



UNIVERSITÀ DIPARTIMENTO
degli STUDI di FISICA
di CATANIA e ASTRONOMIA

PHD PROGRAM IN PHYSICS

ANTONIO ALESSIO LEONARDI

SILICON NANOWIRES: AN OUTSTANDING BUILDING BLOCK FOR
INNOVATIVE APPLICATIONS

PHD THESIS

SUPERVISORS:

PROF. F. PRIOLO
DR. A. IRRERA

ACADEMIC YEAR 2018/2019

Contents

Nanotechnology Age	5
Thesis Outline	13
1 Role of silicon nanowires	15
1.1 State of art of silicon nanowire synthesis	20
1.1.1 Bottom-up and Top-Down approach	21
1.1.2 Metal-Assisted Chemical Etching	38
1.1.3 Conclusion	45
2 Label-free luminescent silicon nanowires sensors	47
2.1 State of art of optical sensing	49
2.2 Silicon sensing platforms	55
2.3 Sensing based on silicon nanowires luminescence	58
2.4 Label- and PCR-free DNA sensing based on luminescent silicon nanowires	60
2.4.1 Functionalization procedure	61
2.4.2 Sensing performances	66
2.5 Gas sensing	70
2.5.1 Si nanowires luminescence sensing	72
2.6 Conclusion	74
3 Artificial 2D random fractal based on silicon nanowires	77
3.1 Fractal charm	78
3.2 Synthesis of silicon nanowires fractal arrays	80

3.2.1	Fractal Si nanowires characteristics	83
3.3	Coherent backscattering of Raman light	90
3.4	Fractal arrays of erbium doped yttrium oxide decorated silicon nanowires	99
3.4.1	Glancing angle sputtering decoration	100
3.4.2	Structural and optical characterization	102
3.5	Conclusion	115
4	Different applications of silicon nanowires	117
4.1	Silicon nanowires based catalysis platform	118
4.1.1	Decorated Si nanowires platform performances	119
4.2	Optical trapping of silicon nanowires	131
4.2.1	4.2.1. Silicon nanowires dynamics in dual beam traps .	133
4.3	Conclusion	144
	Bibliography	145
	Curriculum Vitae	169
	Publication and conference contribute List	171
	Acknowledgements	177

Nanotechnology Age

FROM the beginning, the humankind evolution has been strictly correlated to its technology as a follows of his knowledge. Therefore, this evolution has never had a linear behavior but some events and discoveries changed completely our world. All the great phases of history have in common the discovery of new materials, of new technologies and their applications. Microelectronics and telecommunications represent our last revolution that maybe in the future will be known as the Silicon Age. Silicon is the undisputed leading material of the microelectronics industry as well as the silicon oxide is the main material used to realize the optical fiber that connects our world. While the microelectronics was moving his first steps, from the words of one of the most important scientist of our time, another revolution was just starting. At the beginning of 1960, after all the discoveries of the relativity, the quantum physics, the nuclear physics there was a common question, what remains to discover? Feynman in his famous lecture “There’s Plenty of Room at the Bottom” opens the route and the mind of the academic community to the opportunity and challenge of the nanotechnology [1]. In this lecture, the possibility to arrange information on a small scale, like an entire encyclopedia, by manipulating the atomic surface of just a pinhead was discussed. However, Feynman went beyond the concept of a simply nanoscopic scale (nanoscale) memory by talking of the biology, where sub-micrometric objects are not just memories but can be programmed for a huge amount of tasks. In order to address all the points shown in this fantastic vision, new instruments were required at the time. In 1960 the only equipment that in principle was able to surpass the microscopic scale was the Scanning Electron Microscope. In fact, the Scanning Electron Microscope (SEM) was invented

in 1937 by Manfred Von Ardenne but the first commercial equipment arrived only in 1965 [2]. In the Feynman's talk, the SEM was already present and the scientist claims the necessity of better SEM or similar equipments able to read the position of single atoms. SEM remains today the most used, fast and flexible equipment for the analysis of nanomaterials. Nonetheless, a strong push to the nanotechnology was given by the Scanning Tunneling Microscope (STM) invention. In this scenario, the STM invention by Gerd Binnig and Heinrich Rohrer in 1981 leads to the born of the matter nanomanipulation, the born of the nanotechnology [3]. Some years later, Binnig also developed the first Atomic Force Microscope (AFM), permitting to address the nanofabrication and the nanoscale microscopy also for non-conductive materials [4].

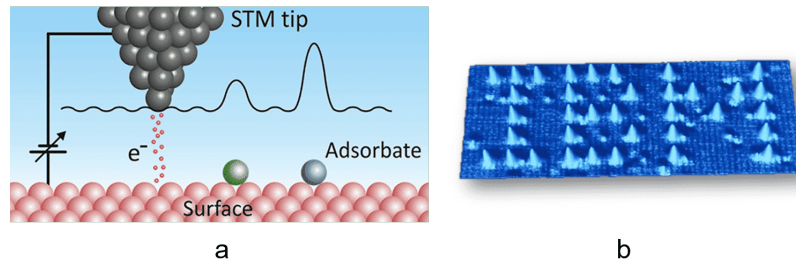


Figure i: a) Scanning Tunneling Microscope (STM) working scheme. b) IBM logo wrote with STM as first example of single atom manipulation with a STM. [5]

In Figure ia, the working principle of a STM is schematized. A voltage is applied to the microscope tip, and when it is close to an object, a tunneling current flow into the tip permitting to reproduce the height of the object. Commonly, the sample is moved through different piezoelectric tubes and this permits to produce a 3D image of the surface by the current signal variation. The realization of the IBM logo, reported in Figure ib, was a strong first example of nanofabrication. The logo realization was demonstrated in 1989 by moving individual atoms of xenon on a Ni substrate, by using the interaction of the tip with a single Xe atom per time [5]. The realization of a nanomaterial as the IBM logo was a pioneering case of a nanotechnology application. A nanomaterial is an object characterized by one or more characteristic lengths below 100 nm [6].

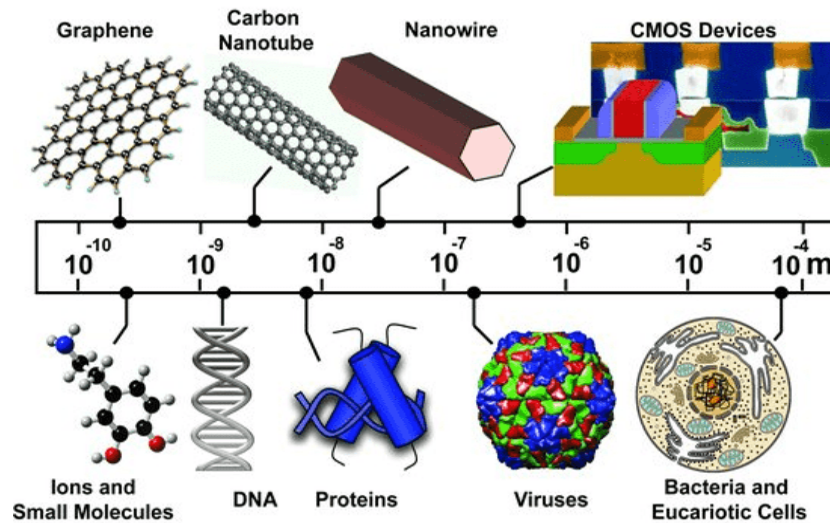


Figure ii: Comparison of different nanomaterials with biological elements of the same dimension. [7]

In Figure ii a comparison of different nanomaterials with biological structure of the same scale are reported [7]. The dimension of these structures opens the route towards the possibility to codify information and to build a device at the same nanoscale of the nature "devices" of which we are made. However, the breakthrough advantage of the nanomaterials is not the low dimension but the new properties that arise at the nanoscale. At this dimension, the quantum mechanics became prominent and different properties became scale, shape and surface dependent.

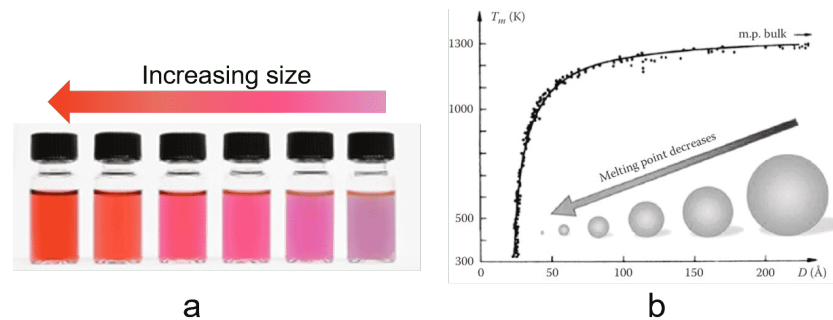


Figure iii: a) Optical properties of gold nanoparticles (NPs) as a function of the size. [8] b) Size-dependent melting point observed for Au NPs. [9]

In Fig. iii some of these changes are shown. As reported in a) for a gold nanoparticles (NPs) suspension, the absorption, transmission, and reflection cross section change dramatically with the size, inducing a naked eye visible color change. In fact, gold is commonly yellow independently to the shape or dimension in the bulk case. On the contrary, when the dimension approaches the nanoscale, due to a plasmonic effect the color change becomes function of the size. It is worth to note that not only the optical properties of the material change. Indeed, in Figure iiib is showed how the melting temperature of Au NPs become a function of the size too [9]. These examples permit to understand how the matter at the nanoscale represents a very interesting and open field for new challenging applications. In the material panorama, silicon is currently the undisputed main actor of the microelectronics industry. The huge earth abundance of this element with the related low cost and its good electrical properties made the Si extremely advantaged with respect to the other semiconductors. Moreover, the silicon oxide with its stability, easy and fine controlled realization has determined the arising of Si as the leading material of our technology. After surpassing the Germanium, since 1970 we saw the doubling of Si transistors inside the same integrated circuit area approximately every 2 years. This technological development trend was discovered by Moore and is known as Moore's law [10].

In Figure iva, Moore's law is reported starting from 1971 to 2018. In the last decades, this trend is starting to change and to show a saturation regime due to the complexity of further down-scaling. Indeed, there are several problems related to the further miniaturizing of the transistors. One of this is related to the physics domain where we can collocate the device and

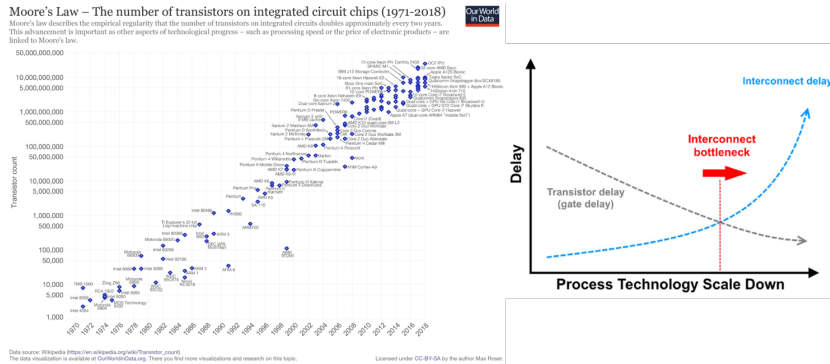


Figure iv: a) Moore's Law on transistor density on integrated circuits. [11]
 b) Interconnection bottleneck for transistor.

in particular to the arising of quantum effects that are no more negligible. In the Complementary Metal Oxide Semiconductors (CMOS) technology, an oxide is placed between a metal and a semiconductor and at the beginning, this material was the SiO_2 . In a CMOS transistor, the insulator is used to let the current flow only in the silicon between the source and the drain region. Due to the down-scaling of the transistor, the thickness of SiO_2 became so small that non-negligible quantum tunneling may occur through the oxide. High-k (high permittivity) materials were introduced to replace the SiO_2 to overcome this issue. This is only a typical example of the challenges faced by Moore's law. One of the hardest limits afflicting nowadays this law is represented by the interconnection bottleneck (showed in Figure ivb). The principal advantage of the miniaturizing of the transistor can be summarized in the reduction of the gate delay and so, in the increasing of calculus speed. However, in an integrated circuit there are billions of transistors all interconnected that work in parallel at the same time. A decreasing in the dimension implies not only more complexity in the circuit realization but also longer and so, more power- and time-consuming interconnections. Today, chips contains several tens of kilometers of copper interconnections [12]. The interconnection bottleneck leads to a disadvantage of further downscaling basically due to interconnection RC delays. These issues are not a future challenge but are present right now. We can just think to the recent several delays on the processor roadmap of the Intel, the most important microelectronics factory. The last down-scaling to the 14 nm technology was done in 2014 with the Broadwell CPU architecture and, even if after different opti-

mization, is still at 14 nm at the beginning of 2019. After different years of delay, the first 10 nm Intel CPU (Cannon Lake) is currently postponed to the second quarter (Q2) of 2019. In the technology revolution seen by our century, another special place belongs to the light. More generally, the use of the light in plenty of fields, from intercommunications to energy production and medicine changed completely our human life. Fiber optics, as well as satellite communication, with the born of internet and now of an all class of cloud services opens the route to an always interconnected society with a massive production of data. In the 2013 Brandtzæg Petter Bae of the Sintef research institute, found that more than the 90% of all humankind data was produced only in the 2 years before the 2013 [13]. In these last years, one of the most interesting challenge is the use of light to transport information inside an integrated circuit by coupling microelectronics with light. Indeed, light is not just the fastest signal that we can think, but with respect to electron transport, is not affected by heating (and so power consumption) due to Joule effect. The use of light might change another time our world. Unfortunately, despite all the silicon advantages, it is an indirect bandgap semiconductor making the integration of light signals in a silicon platform a hard and still open challenge.

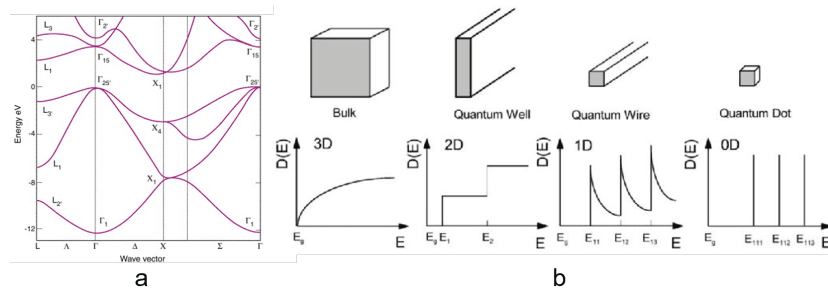


Figure v: a) Indirect bandgap of silicon in the dispersion relation picture. b) Variation of the Density of States (DOS) for low dimensional structures.

In Figure va is reported the dispersion relation picture showing the conduction band edge in the Δ line at 0.85 eV to the X-point while the valence band minimum is at the Γ -point ($k = 0$). At this energy, the photons have not enough momentum to guarantee the momentum conservation and the light emission can occur only as a multiple particle process. The most probable process is simply a three particles one involving the generation or

annihilation of a phonon. This makes the silicon a very poor light emitter at room temperature comprising its applicability in photonics device. However, the new properties arising in the nanomaterials could change the game. In the nanomaterials, when one or more dimensions become comparable to the exciton Bohr radius, the electron Density of State (DoS) changes significantly. This phenomenon is known as quantum confinement. In Figure v b are reported the DoS for the bulk materials (3D) and for 2D, 1D, and 0D structures. The D number represent the dimensions where the electrons are not confined, while the missing ones are related to the quantum confinement spatial degree of freedom. In a bulk crystal, the translational symmetry and so the periodicity of the potential induces the formation of the bands and the electron functions become Bloch waves. In a real finite crystal, the translational symmetry is not infinite, but remain a valid approximation. When the material approaches the nanoscale, the surface effect became prominent and the approximation of infinite translational symmetry is not anymore valid. Quantum confinement corresponds to an increasing of the uncertainty related to the crystalline momentum due to the Heisenberg principle. In a naïve way, we can imagine that the uncertainty is enough to cover the crystalline momentum difference between the valence band maximum and the conduction band minimum. In this picture, the silicon cannot be considered anymore an indirect bandgap material due to the quantum confinement effect and room temperature luminescence become possible. Reality is more complex, and crystalline momentum is not anymore a good number to represent the structure. Different theoretical model considers the problem of the semiconductor applying different correction factors, as electrostatic energy interaction of electron-hole exciton and exchange interaction between them. The probability of an optical de-excitation of the Si increase by reducing the size. The radiative de-excitation probability is a product of the DoS with the oscillator strength that describes the interaction between the involved levels. In confined structures, not only the DoS assume the functions showed in Figure vb but decreasing the size follows an exponentially increasing of the oscillator strength [14]. The emission of light at room temperature in silicon become possible. In this scenario, nanomaterials arise as a strategical resource to overcome the issue of the recent technology making in principle possible the integration of light in silicon. Silicon photonics may be a real strategic resource to go beyond the microelectronics limits. As a clear evidence of that, Intel, the most advanced industry in Moore's law, has an entire division focused on silicon photonics. Nonetheless, history is not written yet.



Figure vi: Photonics transceiver for Data Center of the Intel silicon photonics group. [15]

In fact, the today commercial Si photonics is limited to the only electrical to optical signal conversion in data center facilities, as shown by the device in Figure vi. This is the fascinating contest of this work and the interests of this field. The route to silicon photonics remains today paved with hard challenges and opportunities for the research, as well as for the industry. The next revolution must still be written.

Thesis Outline

Chapter 1

An overview on the role of silicon nanowires in the recent research is presented. In particular, the mostly used approach to synthesize Si nanowires are investigated in details, highlighting their advantages and drawbacks. Nanofabrication methods for the surface structuration at the nanoscale are introduced. Finally, the metal-assisted chemical etching approach, from its born to the nowadays modified approach, is shown.

Chapter 2

In this chapter, a state of art of the current nanomaterial-based sensor is presented with particular attention for the silicon literature. In this scenario, a new class of sensor based for the first time on Si nanowires (NWs) luminescence at room temperature is demonstrated. The Si NWs used are obtained through a modified metal-assisted chemical etching approach by using thin metal layers. This method permits to obtain a cost-effective and Si industrially compatible Si NWs platforms. In particular, the Si NWs sensors obtained have been applied for DNA, and gas sensing demonstrating limit of detection beyond the standard values reported in literature, and that can be applied without the need of a specialized facility, even at home.

Chapter 3

Starting by the recent results of our group in the realization of novel fractal Si NWs, the realization of artificial fractals and their property will be

shown. Thanks to the multiple scattering arising in these materials the first observation of the Stokes second order Raman coherent backscattering at a macroscale level was possible. This phenomenon and the reciprocity breaking related to the Si NWs properties will be analyzed. Finally, the realization of a Er-doped Yttrium Oxide decorated Si NWs fractal substrate will be presented. By controlling the decoration through a glancing angle deposition is possible to control the fractal properties of the material permitting an enhance of the Er emission.

Chapter 4

In this chapter two different applications of silver salt metal-assisted chemical etching Si NWs will be presented. In the first part, the realization of Cu and Au nanoparticles decorated Si NWs as novel and efficient catalysis substrate is presented. The demonstrated results are unprecedented for the Cu pushing forward the literature of the field. In the second part, an interesting study of the dynamic motion of Si NWs optical trapped through counter-propagating beam is presented. In this application, an in-depth investigation of the rich dynamics of trapped NWs, under both optical and hydrodynamic interactions, is shown with perspectives for future applications in optical tweezers.

Chapter 1

Role of silicon nanowires

Abstract

I^N the last century, microelectronics and fiber optics telecommunications changed completely our world. In order to improve the transistor performances, since the 70s, microelectronics industry is pushing down every year the dimension of Si transistors. However, the realization of room temperature light emitting silicon nanowires is less than scarcely reported in the literature and this can be ascribed to the common synthesis approaches used. In this chapter, an overview of several cutting edge technologies of silicon nanowires fabrications will be shown underling their advantages as well as their limitations. Starting from the bottom up approach where small elements are put together, a detailed insight of the Vapor Liquid Solid approach will be given. Different top-down approaches, where a bulk material is etched to realize the nanostructure, will be also showed. Finally, lithography approaches complementary to both bottom up and top down nanotechnologies will be presented. The last part of the chapter will go through the metal-assisted chemical etching approach and its use with thin films. This approach is cheap, compatible with Si technology, all at room temperature and suitable for the realization of quantum confined silicon nanowires with room temperature luminescence.

Silicon is the undisputed leader among all the microelectronics industrial materials. Taking into account the arise of new physical properties at the nanoscale, Si nanostructures emerges as natural candidates for the tomorrow technologies. In particular, silicon nanowires (Si NWs) are emerging as a promising resource in different fields such as electronics [16–18], photovoltaics [19,20], and recently photonics [21,22] and sensing [23,24]. The Metal Oxide Semiconductors Field Effect Transistor (MOSFET) technology born in 1959 at Bell Labs and still remains the most used transistor architecture. In the microelectronics branch, the miniaturizing of the MOSFET technology bring the scientists to think on new improvement possibilities related to the use of nanomaterials, such as nanowires and nanotubes. Si NWs emerge as a natural candidate and the group of Lieber [16] showed substantial advantages with respect to state-of-the-art planar silicon devices.

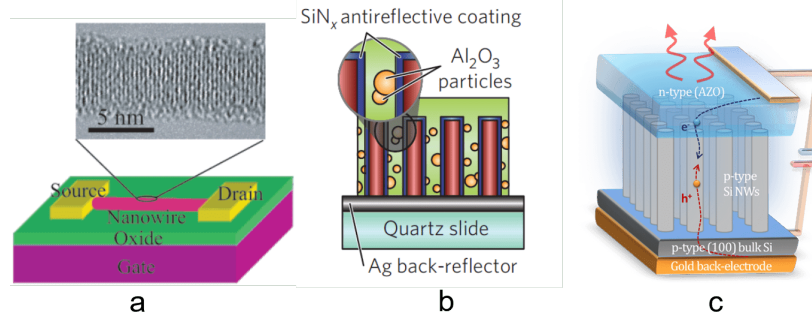


Figure 1.1: Silicon nanowires applications. a) Si NWs Field Effect Transistor. [16] b) Solar cell based on a vertically-aligned Si NWs array. [20] c) Si NWs LED with electroluminescence at room temperature. [25]

In these transistors, the Si NWs FET is realized by using the same planar geometry but with a silicon nanowire as bridge between the source and the drain as showed in Figure 1.1a. The FET is realized by using p-type Si NWs with diameters of 10-20 nm dispersed on a 600 nm silicon oxide layer on top of a silicon wafer. The electrical contact was realized by using an electron beam evaporator (EBE) after the realization of the electrode mask with an electron beam lithography (EBL) process. Thermal annealing process and surface passivation were investigated in order to improve the Si NWs performances. Finally, they observed higher electron conductance from the source to drain. Moreover, in the paper of Feng et al. [18] is reported a low-frequency

noise behavior of the Si NW FET with respect to the planar standard one due to the 1D quantum confinement of the electrons.

In the list of the most important challenges and problems of our time, the energy demand and climate changes are becoming each day even more important. Climate changes are strictly related to the energy and electricity production methods [26]. The World Energy Outlook by the international energy agency reports the use of oil, coal, nuclear and gas around 86% of the total energy production in the 2017 [27]. In order to prevent a disastrous scenario a 75% of the CO₂ emission is demanded by 2050 and adopting a substantial percentage of green energy production is now mandatory and cannot be just a matter of business. Photovoltaics energy is a strategic resource to address this challenge, and in these years the solar cell energy production has become cost-competitive with respect to the energy market. Silicon is the principal material for the realization of solar cells, with above of 90% of silicon panel in the field, due to the cheap manufacturing crucial to compete in the energy market [28,29]. The light managing and its trapping inside a material is of crucial interest in the photovoltaics research. Solar cells efficiency is related to the amount of light that is converted to electric current. The first step is the absorption of light and different strategies can be adopted. The simplest one is to use thick monocrystalline silicon solar cell. Silicon has a bandgap of 1.1 eV at room temperature corresponding to a wavelength of about 1100 nm with negligible absorption for longer wavelengths. This limits the light absorption by Si cells in the IR region. Another point is that, to absorb about the 90% of 700-900 nm incident radiation, a millimeters thickness is required. Despite silicon is a cheap material, the solar cell price is very sensitive to the thickness of silicon used. In fact, all the industrial processes need to realize large surface of high-quality monocrystalline silicon solar cells makes the Si thickness a crucial parameter to the final device cost. Si NWs emerge as a promising tool to increase the light trapping inside the cell with a thickness of at least 2 order of magnitude less than the standard cells. Another Si NWs advantage is the possibility to realize a radial contact around them, in order to drastically reduce the length traveled by the electrons from one side of the junction to the other. Garnett et al. [19] demonstrated substantial advantages in the use of Si NWs. Silicon NWs are realized by using Deep Reaction Ion Etching (DRIE) with a monolayer silica beads as mask. Silicon is etched in the area where the silica beads are not present and 5 μm long Si NWs are obtained. Finally, the silica beads are removed by a hydrofluoric acid etching. In order to obtain the radial p-n

junction, a boron doping of the starting n-type Si NWs was realized. By this strategy, the light path length inside the solar cell is increased by a factor of 73 with 10 times higher efficiencies than by using thin silicon layer with the same thickness of the Si NWs. However, a final efficiency of only 5% was obtained, probably due to the surface and junction recombination affecting the device. Another impressive example of this research field comes from Atwater's group [20], that demonstrated the realization of a solar cell where the p-n junction is formed by embedding the Si NWs into polydimethylsiloxane (PDMS), a conductive polymer. In particular p-type 2-10 μm long Si NWs were synthesized by VLS with a small packing fraction, studied from 1.6% to 16%. Si NWs were covered by 80 nm SiN_x anti-reflective coating and finally embedded into the PDMS. To further improve the performances of the cell, Al_2O_3 particles (0.9 μm of diameter) were added to the polymer to improve the scattering efficiencies inside the cell. The final structure is shown in Figure 1.1b. The obtained device was photo-electrochemically measured and showed a normalized peak external efficiencies of 0.89. This result is very promising but is also noteworthy that a real cell inside an electrolyte solution presents several problems.

The realization of silicon light-emitting devices but also the simpler silicon light emission remain scarcely reported. Porous Si was for a long time studied by several groups to obtain a Si-based light emitter [30, 31]. However, porous Si is generally non-mechanically robust and its photoluminescence (PL) is commonly not very bright and unstable [31, 32]. Silicon quantum dots (or nanoclusters) were used recently as in vivo light source to produce tissue bio-imaging [33]. However, a robust integration of Si nanocrystals (NCs) in a flat substrate without compromising their optical properties is still complex. In this field, Priolo et al. demonstrated the realization of light emission from Si NCs embedded inside a silicon dioxide layer [22, 34, 35]. A silicon oxide sub-stoichiometric layer is deposited by Plasma Enhanced Chemical Vapor Deposition (PECVD) and after a subsequent annealing process, Si NCs are realized embedded in a SiO_x substrate. Moreover, due to the silicon dioxide, the electrical addressing of the device is still very complex and non-radiative recombination at the oxide defect sites may occur. In the photonics field, the application of silicon nanowires is extremely limited due to the drawback of the common synthesis methods. Vapor-Liquid-Solid is the most used approach to synthesize Si NWs. However with this approach is very complicated to obtain vertically aligned NWs with diameters under 50 nm, and commonly, disordered bunches of nanowires are formed [36]. The

occurrence of metal contamination due to the high process temperature is another strong drawback to obtain light emission. Quantum confinement effect requires diameters under 10 nm that are extremely complicated to obtain, even by using very expensive and complex Electron Beam Lithography (EBL) processes coupled with Deep Reactive Ion Etching [37]. All these disadvantages will be analysed during the next paragraph. By taking advantage of the Ge direct bandgap Karem et al. [38] demonstrated near-IR emission of strained Si/Ge NWs synthesized by Vapor-Liquid-Solid approach. However, the structure is affected by different drawbacks as an IR shift due to a hardly controllable stress-induction process. Another strategy used in literature is the doping of Si NWs with emitting impurities as Fe atoms. However, these impurities act as trap levels commonly preventing the possibility to electrically pump the system and increasing the non-radiative losses. Therefore, metal impurities that can migrate inside the silicon are often avoided in Complementary Metal Oxide Semiconductors (CMOS) process due to the detrimental effect on the electrical behavior of the whole integrated circuit. Recently, our group demonstrated the possibility to obtain Si NWs that emit light at room temperature due to the quantum confinement effect. In Figure 1.1c is showed a LED realized by a p-n junction of p-doped Si NWs and Aluminum Zinc Oxide (AZO) as n-type layer [25, 39]. This Si NWs LED shows room temperature emission at few volts of bias. This result is achieved realizing the Si NWs through an innovative modified Metal-Assisted Chemical Etching approach that involves the use of few nanometers thick gold film. The original approach and the thin film modification will be investigated in the last part of the chapter.

Recently, nanostructures are also arising as strategic solutions even in sensor applications. Novel high-sensitive sensing methods, with the possibility to enable a label-free analysis even at home, are some of the most interesting challenges faced by the nowadays scientific community. In fact, several pathologies and diseases can be screened by the use of specific biomarkers. Nanostructures naturally emerge as a strategic resource due to their enhanced surface to volume ratio and to their size comparable to the analyte. However, nanostructured sensors remain scarcely diffused in the industry due to the expensive and often CMOS incompatible synthesis and functionalization approaches. In this field, Si is naturally advantaged among other materials and Si Field-Emission-Transistor sensors with single virus sensitivity are already been demonstrated [40, 41]. However, these sensors are realized by using complex EBL lithography and etching system and their sensing range

is limited to few tens of analyte making the sensor unsuitable for a real commercial use for most of the analytes. In the second chapter, the state of art of silicon sensing will be investigated in details and the realization of a new ultrasensitive and selective class of sensor, based on the luminescence at room temperature of silicon nanowires, will be presented.

1.1 State of art of silicon nanowire synthesis

The material manipulation at the nanoscale involving Physics, Chemistry, and Engineering is generally indicated as nanotechnology. In particular, nanotechnology can be divided into two main approaches: Bottom-Up and Top Down. In the second part of 1900, the rush to the nanofabrication saw the formation of 2 different roads: one starting from the chemistry and another one from the microelectronics industry. The first one is called bottom up and is characterized by the assembling of smaller elements such as atoms and molecules. The second one is called top-down and is realized by the reduction of the bulk material to the nanostructured one. For this reason, this approach is also known as “the sculptor’s approach”. These two methods are schematically depicted in Figure 1.2. However, different nowadays approaches are not easily inside this distinction but are characterized by both top-down and bottom-up synthesis steps.

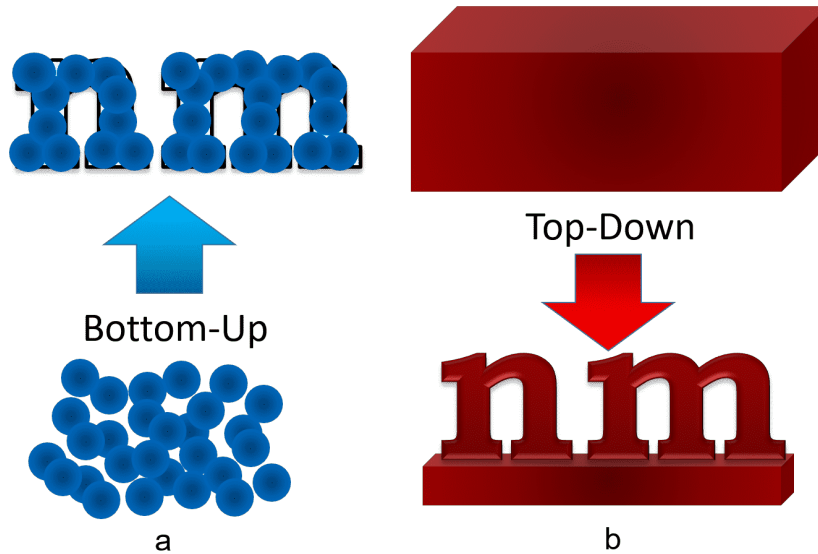


Figure 1.2: Nanotechnology type. a) Bottom up approach scheme with the realization of a nanomaterial starting from smaller units. b) Top Down approach also known as sculptor approach. Nanomaterials are realized removing material from a bulk unit.

1.1.1 Bottom-up and Top-Down approach

Vapor-Liquid-Solid

The most common Si NWs synthesis process is the Vapor-Liquid-Solid approach. This method is a bottom-up approach and is characterized by the use of a silicon-based vapor as a source of silicon atoms to the Si NWs synthesis. The growth of NWs is catalyzed by gold droplets that are realized as a product of the melting of Au nanoparticles (NPs) contaminated with silicon atoms. These droplet of gold-silicon alloy are liquid due to eutectic phase condition obtained through specific chamber thermal condition. When the silicon concentration inside the alloy becomes higher than the thermodynamic equilibrium Si concentration of the eutectic phase, the silicon precipitates. Hence, Si precipitates under the gold, solidifies, and growth as nanowires. The name of this approach is due to the phase changes of silicon from vapor to liquid, and finally into solid.

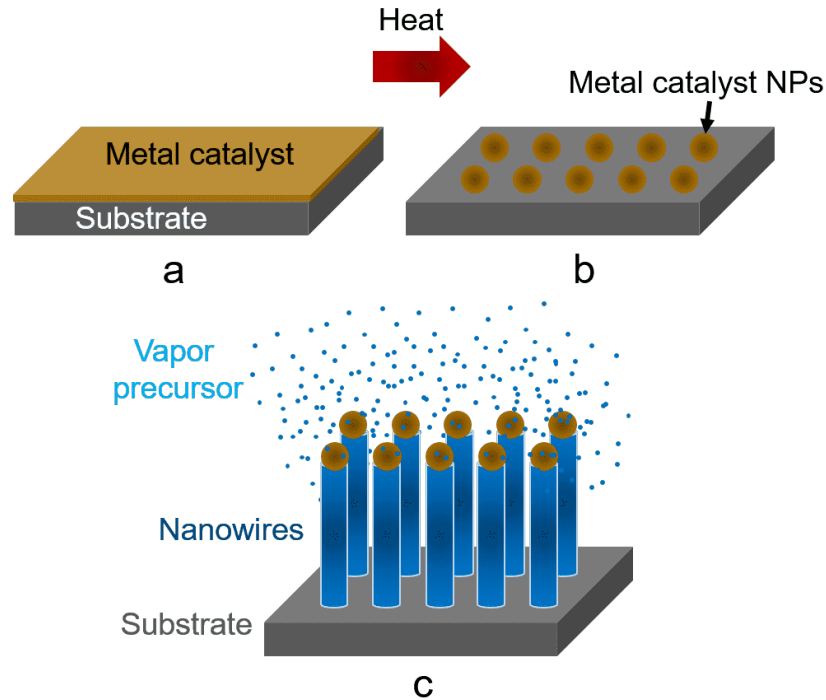


Figure 1.3: Typical VLS scheme for Si NWs. a) Metal layer deposition. b) Clustering of the NPs by annealing. c) Si NWs realization by VLS approach.

In Figure 1.3 a typical VLS process is shown. In this process as the first step, a gold film is deposited on a Si bulk substrate (Figure 1.3a). A simple process to obtain the Au NPs is the annealing of the gold film, that due to the de-wetting effect, follows in a clustering of the gold onto the Si substrate (Figure 1.3b). The substrate covered with the gold nanoparticles is then exposed to a silicon-based vapor precursor at a specific temperature related to the eutectic phase temperature of the gold-silicon alloy (Figure 1.3c). The eutectic phase of a two element alloy is defined as the element mixture characterized by a melting (or in certain cases solidifying) point with a temperature smaller than the temperature needed by the two single elements.

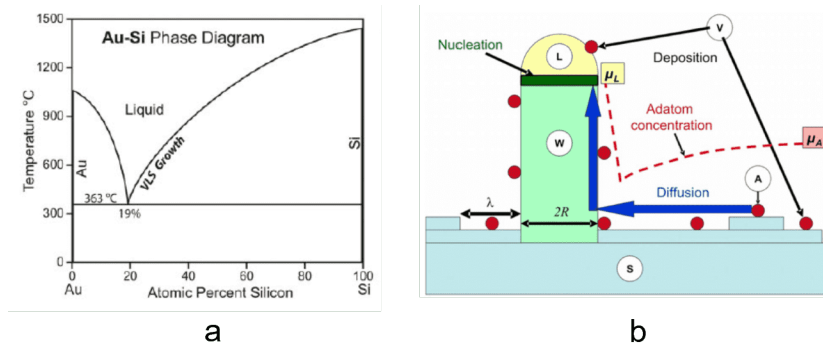


Figure 1.4: a) Au-Si phase diagram showing the Eutectic point after which VLS growth is performed. [42] b) Growth kinetics scheme in VLS approach. [43]

In Figure 1.4a the silicon-gold alloy phase diagram is shown. This graph shows the variation of melting temperature as a function of the silicon percentage in the alloy with the 0% and 100% of Si percentage that corresponds to pure gold and pure silicon, respectively. At the 19% of Si into the alloy correspond the eutectic point with a melting temperature of 363 °C. In the VLS approach, the temperature is set slightly higher than the eutectic melting temperature (supersaturation condition) and inside the chamber a gas precursor is commonly used as a silicon source. Atoms of silicon are adsorbed onto the substrates and due to the chamber temperature diffuse onto the surface. Silicon can be directly adsorbed by the gold droplets or diffuse inside them (Figure 1.4b). The growth of NWs occurs when the Si atom flux, that reaches the droplet by direct absorption and in certain cases by diffusion (i.e. Molecular Beam Epitaxy), is higher than the flux of desorbed ones. When the Si atoms reach the droplet, the Si concentration of the alloy changes surpassing the thermodynamically equilibrium one. The thermodynamical position of the alloy in the phase diagram changes and so the melting temperature of the Si. Hence, silicon atoms precipitate under the droplet solidifying. The droplet is pushed up and a silicon nanowire growth under each droplet.

One of the most important advantages of the VLS is the flexibility of the approach that can be adapted to different equipments [42]. Starting from the Au NPs decorated Si substrate, there are several approaches to provide the silicon in the reactor chamber that go from physical to chemical deposition

techniques. The difference between these two methods is that, in the chemical deposition a chemical reaction occurs (not necessarily on the surface) and one or more reaction products are deposited. In physical approaches, chemical reactions does not occur and what is inserted in chamber is deposited. Chemical Vapor Deposition (CVD), Thermal Annealing, Thermal Evaporation, Molecular Beam Evaporation (MBE), Pulsed Laser ablation, Chemical Bath Deposition (CBD) are just some of the most used methods to realize the VLS synthesis. All these techniques are schematically represented in Figure 1.5 in the same order as previously listed. In particular, CVD and CBD are chemical approaches while the others are physical.

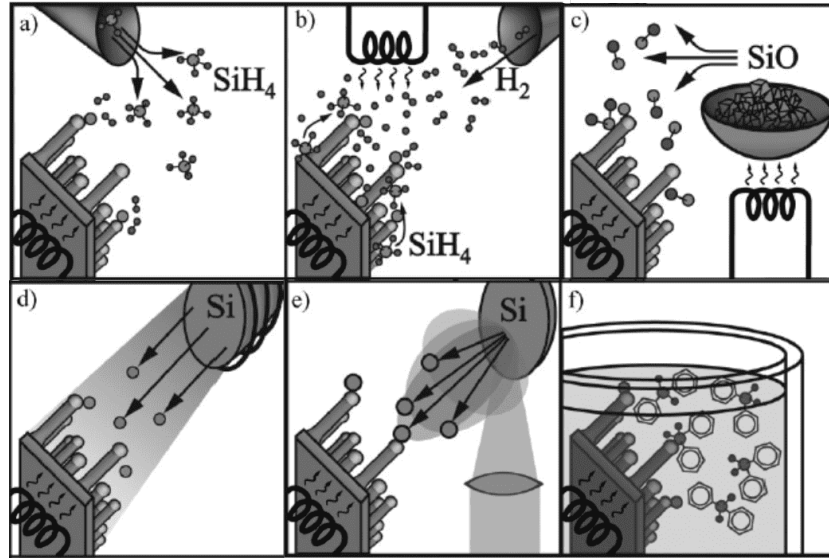


Figure 1.5: Comparison of VLS synthesis performed in different approaches: a) Chemical Vapor Deposition, b) Thermal Annealing, c) Thermal Evaporation, d) Molecular Beam Evaporation, e) Pulsed Laser Ablation, f) Chemical Bath Deposition. [42]

CVD is the most used and explored approach for the VLS Si NWs synthesis. This method offers high flexibility over the Si NWs growth rate from 10^{-2} to 10^3 nm/min [44, 45]. Another advantage is the possibility to obtain Si NWs with a very small diameter up to about 10 nm as shown by the Lieber's group [46]. However, it is very complex and time-expensive and the Si NWs showed in this paper have different orientations and appear as a

hank of wires and not really suitable for real applications. In fact, a strong drawback of CVD process is that the Si NWs exhibit a strong variation on the growth direction for diameters smaller than 50 nm and moreover, a low Si NWs density.

Silicon nanowires, better known as Si whiskers during the period between the 60s and 90s, were discovered by using a thermal annealing into a reactive atmosphere by Wagner and Ellis [47]. Temperatures higher than 900 °C Poly(methyl methacrylate) (PMMA) are used with gas as hydrogen, iodine, bromine that react with metal impurities acting as catalysts. The reaction of these gas in the area of the metal impurities generate gas as SiH_4 that acts as a silicon source for the VLS synthesis. The principal advantage of this method is its simplicity but lack of a strong control on the synthesis process. Synthesis by silicon monoxide evaporation is a low-cost approach that permits to realize NWs with also millimeters length. This approach was demonstrated to work also without a catalyst as for the laser ablation where silicon dioxide can be used to catalyze the growth. However, the size dispersion is high and goes to several hundreds of nanometers. Another disadvantage, for both metal and the metal-free VLS by Si monoxide evaporation, is the synthesis of Si NWs with a small crystalline core surrounded by an amorphous shell.

MBE approach was successfully implemented to obtain epitaxial Si NWs on Si (111)-oriented but is limited to diameters greater than 40 nm and very low density. Moreover, this approach is very expensive, time-consuming and incompatible with the microelectronics industry. In this approach, the precursor gas is silicon and no chemical reaction happens, differently from the CVD and like all the other physical approaches. Differently from the CVD, where the Si atoms are obtained after a chemical reaction catalyzed by the Au alloy, in the physical approaches there is a direct source of Si atoms. In fact, in all the physical approaches the silicon can be adsorbed directly into the Si-Au alloy or can be adsorbed in another point of the substrate and diffuses to the alloy site participating to the growth.

Laser ablation is one of the easiest and cheapest ways to produce Si NWs without, perhaps, the need of a substrate. A mixed target of silicon and catalyst metal is ablated by a laser beam and the silicon material collide with an inert gas. The ablated material already contain both the silicon source and the catalyst. Another aspect of this approach, is the possibility to tune the silicon sub-stoichiometric oxide surrounding the silicon nanowire by adding and tuning a SiO_2 source. The NWs diameters not only depend

on the temperature and substrate used but also on the inert gas type and condition. However, the size dispersion is typically high and is impossible to obtain well oriented and aligned silicon nanowires, thus strongly limiting the appeal of this method.

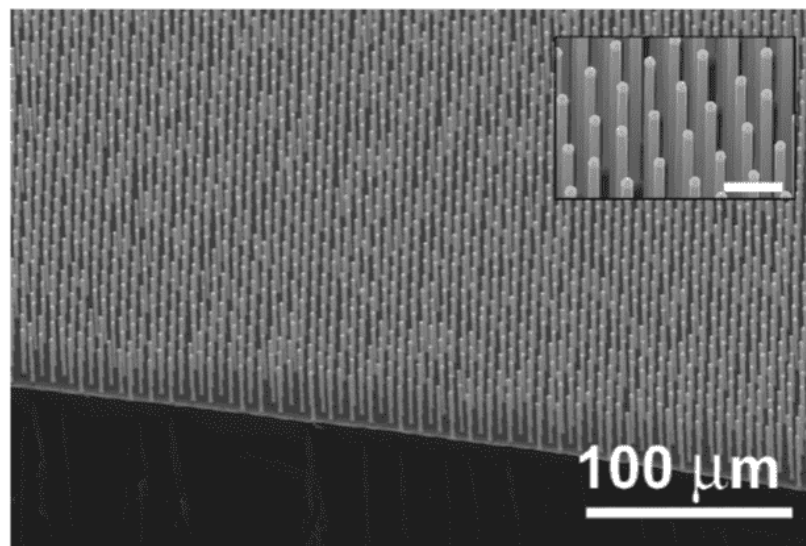


Figure 1.6: Tilted SEM image of VLS synthesized Si NWs. The scale bar in the inset is 10 μm . [48]

In Figure 1.6 a tilted cross-section image of VLS growth Si NWs obtained through a Scanning Electron Microscope (SEM) is reported. In this case, the Si NWs are synthesized by using a CVD process onto a Si (111) substrate. On the top of the silicon nanowires are still visible the gold NPs used as catalysts and a high density of Si NWs is present. The NWs diameters are strictly correlated to the Au NPs diameters.

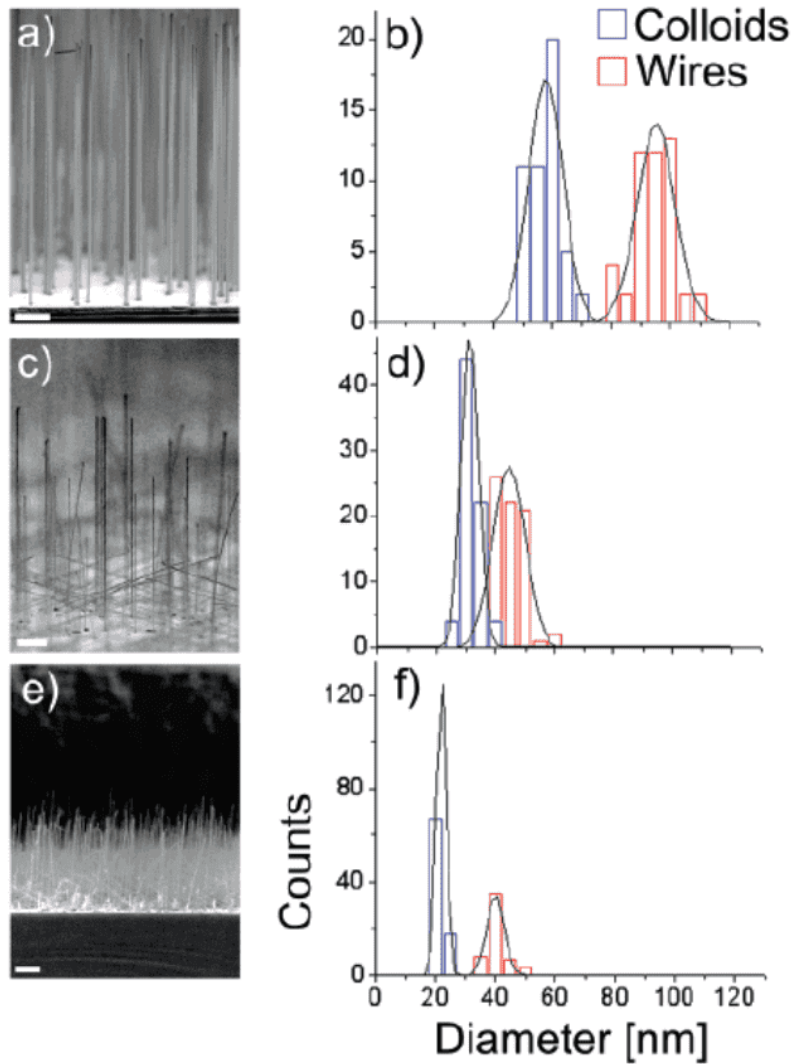


Figure 1.7: Cross section SEM images of VLS synthesized NWs with different average diameter are showed in a), c), e). On the right of the SEM images in b),d), f) the correspondent statistical analysis of the wires and Au NPs diameter dimension are reported. [49]

Figure 1.7 shows the comparative study of Hochbaum et al. on Si NWs and Au NPs diameters in a VLS CVD process using SiC_4 as precursor gas [49]. The NWs diameters obtained were always higher than the Au NPs ones with dimensions not suitable for quantum confinement. This represents a

first limitation to the synthesis of room temperature light emitting Si NWs. In the work of Hochbaum, a maximum density of 1.8×10^8 NWs/cm² is obtained. Commonly, higher densities are difficult to obtain by VLS due to the metal NPs arduous manipulation. Nanoparticles have strong van der Waals attractive forces and tend to cluster into larger particles. Moreover, due to the high temperature of the process, Ostwald ripening occurs and the agglomeration of small particles into bigger ones is thermodynamically favorable. These phenomena make the deposition of metal nanoparticles very laborious in terms of positioning and in general preparation of the substrate. Another strong constraint to the NWs diameter size is due to the Gibbs-Thomson effect [43]:

$$\Delta\mu = 2\gamma/r_{\text{cur}} \quad (1.1)$$

Where γ is the surface tension and $\Delta\mu$ is the difference between the chemical potential of the Si atoms inside the droplet and the gold atoms (or in general the catalyst atoms). The constrain to the critical radius come from r_{cur} . Gibbs-Thomson effect imply that in order to obtain diameters of few nanometers the Si atom incorporation into the silicon-metal alloy require an higher supersaturation condition [50]. From other thermodynamic considerations is possible to define a critical radius under that the Si NWs growth is not thermodynamically favorable. This critical radius is defined as:

$$r_{\text{crt}} = \frac{2V_{\text{liq}}}{RT \times \ln \frac{p}{p_0}} \sigma_{lv} \quad (1.2)$$

where p/p_0 is the partial pressure of the silicon precursor, V_{liq} is liquid droplet molar volume, σ_{lv} is the liquid vapor surface energy [42].

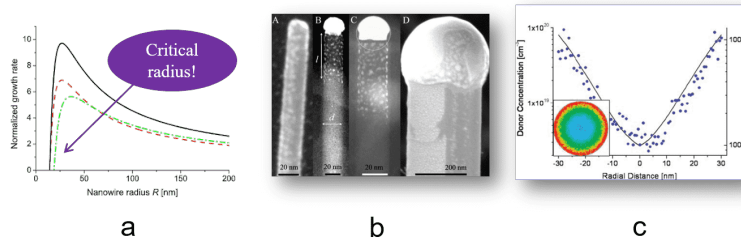


Figure 1.8: a) critical radius limitation by Gibbs Thomson Effect. [43] b) TEM images attesting the presence of gold contamination. [51] c) High disuniformity of the doping realized during the growth due to the high temperature of the process. [52]

This critical radius comes from the Gibbs Thomson effect and it is on the order of 10 nm for the growth of Si NWs catalyzed by gold (as shown in Figure 1.8a). This limit makes very difficult the realization of quantum confined Si NWs. An alternative approach used to obtain very small diameters consists in one or several oxidations by an annealing process each one followed by many vapor or wet HF etching processes. However, this procedure follows in rough Si NWs surface that affects the electrical and optical properties by surface recombination losses. Therefore, Si NWs will be characterized by a small Si core surrounded by a big SiO₂ shell that makes very complex an electrical pumping of the system and the realization of a device. Another crucial limitation is represented by the presence of gold contamination inside the Si NWs, as reported by the Transmission Electron Microscopy (TEM) analysis in Figure 1.8b [51]. Due to the high temperature required by the VLS synthesis process, the gold diffuse inside the Si NWs introducing new trap level in the middle of the band gap. As a consequence non-radiative recombination due to Shockley-Read-Hall effect became more efficient. This effect dramatically affect the performance of the Si NWs in any type of application [53]. Si NWs synthesized by the VLS using Au are intrinsic and the doping is generally obtained during the growth by the use of another gas precursor containing the dopant species. However, due to the high thermal budget required by the VLS, the doping is not uniform. Indeed, as showed by the figure 1.8c, a high dopant segregation onto the surface is attested. Koren et al. demonstrate a disuniform profile of doping [52]. To surpass this drawback, other doping methods are used in literature as low energy ion

implantation. However, in this case, several defects are introduced to the silicon nanowires [54] and in some case can be even present a plastic deformation of the Si NWs due to the amorphization of the silicon [55]. Due to the CMOS incompatibility of the Au and to the trap level effect described, the scientific community focused a lot of effort on the use of different catalyst material. However, a definitive CMOS compatible solution, easily feasible, and without any other drawback, is not available. Due to the high thermal budget required by this approach metal catalyst atoms are always present as final impurities. This makes the impurities level position with respect to the silicon bandgap a crucial starting point to avoid the present of trap levels and their detrimental effect to the electron conduction, as well as an increasing of the non-radiative de-excitation processes.

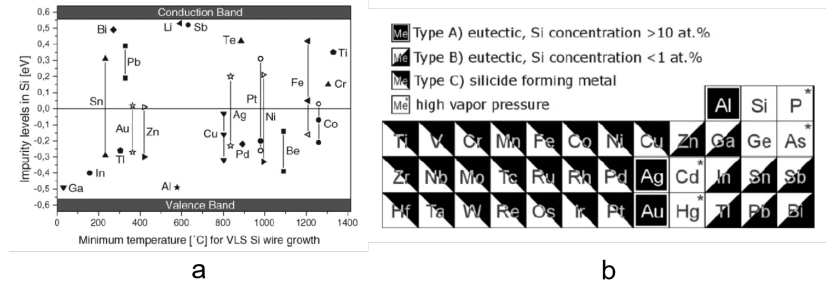


Figure 1.9: a) metal impurities level position inside the Si bandgap. Different level of the same metal are linked with a line. All the metal are reported ordered following the minimum temperature requested for the VLS growth visible in the x-axis. b) Periodic table of the known working VLS metal subdivided by catalysis type. [42]

Figure 1.9 from the work of Schmidt et al. [42] can be used to schematize the behavior of the most used metal catalyst in VLS. In particular in figure 1.9a the bandgap position of some of the most used VLS metal catalyst are showed. For the elements shown in figure, going from left to right, the eutectic temperature required for the VLS process increase. By using the catalyst subdivision of Schmidt et al. [42] (showed in figure 1.9b) we can classify all the potential catalysts in 3 classes called type A, B, and C. Type A catalysts are characterized by a simple eutectic phase diagram with a single eutectic point corresponding to a Si percentage of 10% or higher. This class is the most indicated and Au belong to them. Type B differs from the A

just for the position of the eutectic point at a very small concentration of Si, commonly around 1%. Type C present one or more siliced phase and the eutectic points are all at a higher temperature than 800 °C. Starting from the type A, the new most promising catalyst for Si NWs is the Al with an eutectic temperature of 577 °C. Due to the position of Al impurities as hole donor, the Si NWs synthesized by Al result p-type and commonly heavy doped with 10^{18} - 10^{19} atom/cm³. Moreover, due to the high temperature, the doping realized during the growth is not uniform respect to the NWs radius and is greater onto the external surface, as also discussed for the doping of the Si NWs realized during the growth. Another type A catalyst is the Ag with a high eutectic temperature of 835 °C. Ag impurities, as visible in Figure 1.9, introduce 2 deep levels into the bandgap that can affect the electrical and optical properties. Type B catalysts are characterized by very low Si concentration at the eutectic point. Belonging to this class, Zn and Cd were demonstrated as possible Si NWs VLS catalyst. However, the growth by these metals require very high vapor pressure reaching more than 1 mbar and eutectic temperatures of 420 and 321 °C, respectively. Relevant in this class are also In and Ga with an eutectic temperature of 30 and 156 °C, respectively. However, these low temperatures are not a real advantage. Indeed, in a standard CVD process temperature higher than the eutectic point ones are required, and these low temperatures commonly make the growth more complex and less controllable. In fact, in literature different case of conical shape due to high incorporation or evaporation of the metal can be found [56]. Other type B element as Sn, Pb, Sb, Bi are reported to not allow stable Si NWs growth [57]. Type C metals are characterized by a complex phase diagram with the presence of several silicide phases. Commonly high temperature is required for these elements and most of them as Fe, Dy Pd, leads to poor crystalline quality. Cu and Ni have the same problem of the Au introducing trap level inside the band gap. The most interesting element of this class is the Ti due to its CMOS compatibility and to the quality of Si NWs realized. However the synthesis starts at a temperature higher than 1000 °C and, in the range between 1000 and 1330 °C, and this is troublesome for any device fabrication. Moreover, different sub-stoichiometric transitions of the silicide particle through the different Ti-Si ratio occur before the Si NWs synthesis. All the type C, but also several type B and A, can be used in a Vapor-Solid-Solid (VSS) approach where the temperature is set under the eutectic point. Despite this reduces the required thermal budget, the same drawbacks of the VLS approach apply to the VSS. Therefore considering the

literature, type C in VSS mode are found to synthesize Si NWs with a higher number of defects with respect to the VLS counterpart.

Reactive Ion Etching

Reactive Ion Etching (RIE) is a CMOS compatible top-down approach. In particular, this method is a dry etching approach based on a directional etching by a reactive ion plasma. A strong radio-frequency (RF) electromagnetic field generate the plasma of the reactive gas in a low-pressure chamber and the ions are accelerated to the sample. By using a RF electromagnetic field, the electrons are in each cycle accelerated much more than the ions due to the huge difference of the mass. When the electrons reach the chamber wall are eliminated by the ground of the chamber. However, the electrons than reach the sample, electrically isolated from the rest of the chamber, negative charge it attracting the plasma ions to the sample. The etching is caused by a chemical reaction between the ions and the substrate. The etching is anisotropic through the ion direction with respect to a standard wet etching. An evolution of this process is the Deep Reactive Ion Etching (DRIE) were the etching is even more anisotropic and great aspect ratio nanostructure can be realized. In particular, the Bosch process is the most used DRIE and it is often indicated just as DRIE. This approach has become one of the most interesting fabrication technique in order to obtain high aspect ratio nanostructures up to 50:1 aspect ratio. Other different approaches, as the Cryogenic RIE [58], were proposed as DRIE alternatives but the Bosch is currently the only one truly industrially reliable. With respect to the standard RIE, in this process a cycle of RIE etching is followed by a passivation of the sample, and these two steps are repeated several times. In this way, the effect of the ion direction plays a greater role than in the standard etching, permitting to obtain a higher anisotropic etching. RIE and DRIE etching rate are determined to the chemical affinity of the reactive ion gas with respect to the material. Different materials require the use of different gases to be etched. This can be used in order to etch a specific material on a substrate without etching the entire substrate. Indeed, to realize a specific pattern the substrate has to be masked with a material chemically inert with respect to the reactive gas used. Several approaches can be used to mask the substrate, from cost-effective assembly methods to more complex and expensive UV and Electron Beam Lithography (EBL). Due to the high aspect ratio, this approach is suitable for the realization of Si NWs surpassing several draw-

backs of the VLS approach such as impurity levels and doping. The etching of the Si is generally obtained by using SF_6 or chlorine (Cl_2) gas to selectively etch the silicon and a C_4F_8 passivation gas to enhance the anisotropic effect. Suitable materials, used as a specific mask for the etching of Si, are Ti, Cr or even polystyrene particles [19, 59] that are not or only slightly etched during this method.

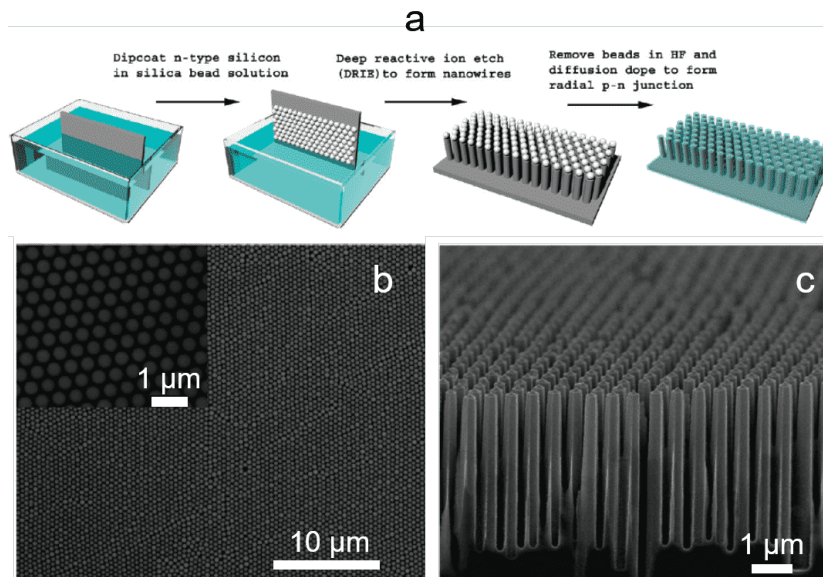


Figure 1.10: a) Scheme of a Reactive ion etching process used for the Si NWs realization. SEM images of the Si NWs showed in plan view b) and in cross section c). [19]

In Figure 1.10a the scheme of a typical DRIE process is reported by Garnet et al. for the realization of vertically oriented and highly ordered Si NWs [19]. In this paper, the mask is realized through the self-assembly of a polystyrene bead monolayer on the Si surface by a dip coating process. A DRIE process is then carried out and the unmasked Si is etched. The Si under the polystyrene particle remains not etched and form the Si NWs. The achieved length was $5 \mu\text{m}$ and the dimension of the sample goes up to 16 cm^2 . However, the sample dimension is not limited by the Langmuir-Blodgett method used to realize the bead monolayer self-assembly mask [60]. Indeed, this method permits to easy cover a 4" wafer. The diameter of the Si

NWs, determined by the beads, was 390 nm in the first case and 530 nm in the second case. The obtained Si NWs are shown in plan view and in cross section SEM images in Fig. 1.10b and c), respectively. With this approach, diameters on the order of tens of nanometers can be obtained. However, this limit the length of the synthesized Si NWs. In fact, a common limit in the aspect ratio of about 50:1 (in some case up to 100:1) [61,62] strictly correlates the diameters to the final achievable lengths of the Si NWs. However, the realization of diameters on the orders of tens of nanometers is extremely complex. In addition, Si NWs realized with these approaches have a rough surface and in several case surface damage that induces surface recombination losses. This is a crucial drawback for the realization of any type of device.

UV and Electron Beam Lithography

In order to obtain nanoscale features or in general nanomaterial, most of the bottom-up or top-down approaches are driven or limited by a specific material. For example, VLS is driven by the use of metal nanoparticles and RIE by the chemical reactivity of the ion gas with a specific material. The use of self-assembly methods is a powerful and cheap resource to mask a material in order to obtain an anisotropic fabrication. Approach as de-wetting through thermal annealing process or Langmuir-Blodgett self-assembly were successfully addressed in several applications. However, there are cases were a stronger control over the device features is required and in these cases, other techniques need to be carried out. The most used approach to obtain strongly controlled micrometers features is UV lithography. Perhaps, this method is used every day in the current CMOS industry to realize complex integrated circuits on top of a Si substrate [63]. UV Lithography permits to have a strong control up to the limit of UV light diffraction corresponding to hundreds of nanometers [64, 65]. Recent improvement of this approach through the use of a UV laser is known as extreme UV lithography and promise in the next few years to push this limit under tens of nm with an industrial compatible approach [66, 67]. In all the cases, an UV source is used to change the local property of a polymer layer in order to produce a mask for further material deposition (i.e. Au NPs for VLS) or for selective etching (i.e. RIE for Si etching). Resist polymer can be divided into positive and negative resist. The UV light is used to change the solubility of the resist with respect to a specific solvent called resist developer. Positive resist become soluble when exposed through the UV light and unexposed portion

of them remain insoluble. On the contrary, negative resist becomes insoluble when exposed to the UV source and are soluble when unexposed. The first step of the process consists in the resist spin-coating onto the substrate. Then the polymeric film is exposed through a specific pattern. The pattern exposure can be obtained by the use of a prefabricated mask that determines the shape of an UV light source. Another better approach is to use a focused laser beam that scans the sample forming the required specific pattern.

In order to surpass the diffraction limit of the UV light, several approaches were proposed as electron beam induced lithography [68], X-ray lithography [69], nanoimprinting lithography (NIL) [70] and Electron Beam Lithography (EBL) [71,72]. In fact, the minimum feature achievable by UV lithography is proportional to λ/NA , where λ is the wavelength used and NA the numerical aperture of the lens. So in principle, by decreasing λ and decreasing the beam spot (increasing NA) is possible to push down this limit. However, other limitations related to the focus of the beam are present. Nanoimprinting Lithography is based on the mechanical deformation of the resist that subsequently is processed through UV light exposure (photo NIL) or by heating (Thermoplastic NIL). A nanoscale patterned mold is used to mechanically deformate a spun polymer by using a thermal or cold welding process. The polymer is then cured through the use of light (photo NIL) or by either a thermal or cold welding process (Thermoplastic NIL). This approach is in general cheap and CMOS compatible with the possibility of large scale applications. Indeed, recently Toshiba validate the process for 22 nm for industrial use [73]. However, NIL results still limited for the feature dimension achievable on tens of nanometers and further improvements are required to reach the resolution limit of EBL.

EBL is the most used approach with respect to the others due to its flexibility of use. In a EBL process electrons are used instead of photons with the advantage of shorter wavelength with respect to UV light. In fact, even in Scanning Electron Microscope (SEM) typical energy value for the electron beams span from 100 eV to 30 KeV with associated λ that goes from about 12 nm to 0.04 nm, respectively. In particular, the possibility to be carried out by using a standard SEM with a beam controller, and an opportune software, make EBL extremely diffuse in research facilities. Another advantage is the fact that the electron beam is directly focused and driven to span the polymer with a chosen pattern without the need of a mask, required in other approaches such as conventional UV Lithography or NIL. However, the use of a SEM as EBL equipment permits to achieve a maximum resolution

of several tens of nanometers (commonly on the order of 50 nm). To push down this limit to sub-10nm, more expensive and dedicated equipments are required [74] achieving a limit of about 5 nm [75]. The definition of positive and negative resist is the same for the EBL resist by considering, in this case, the exposure through a focused electron beam.

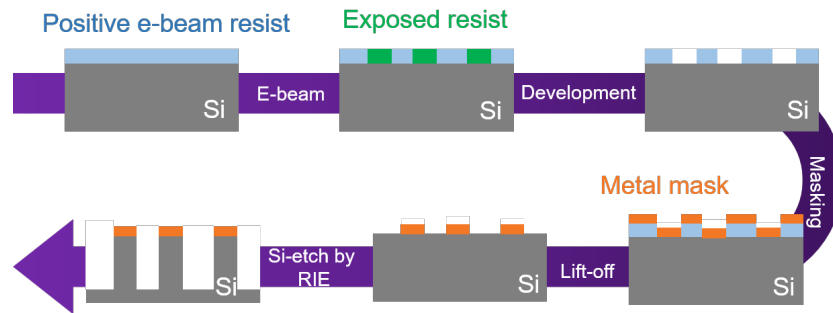


Figure 1.11: Flow chart of the Si NWs synthesis by a EBL based approach.

In Figure 1.11 a typical EBL flow chart for a positive resist is reported showing the principal step during the process. After a cleaning procedure, the sample is spun with Poly(methyl methacrylate) (PMMA) and then baked for 20 min at a temperature between 120°C and 180°C (for Si commonly around 160 °C). The sample is then inserted into the SEM chamber and is ready to be processed. After the EBL exposure is then developed through a Methyl isobutyl ketone (MIBK) 1:2 Isopropanol (IPA) solution for 70 seconds and then for other 20s in IPA. The sample is finally rinsed in water and dried by a nitrogen flux. A nanoscale features mask is now ready to be used for further top-down (i.e. RIE, chemical etching..) or bottom-up (sputtering, EBE, ...) processes.

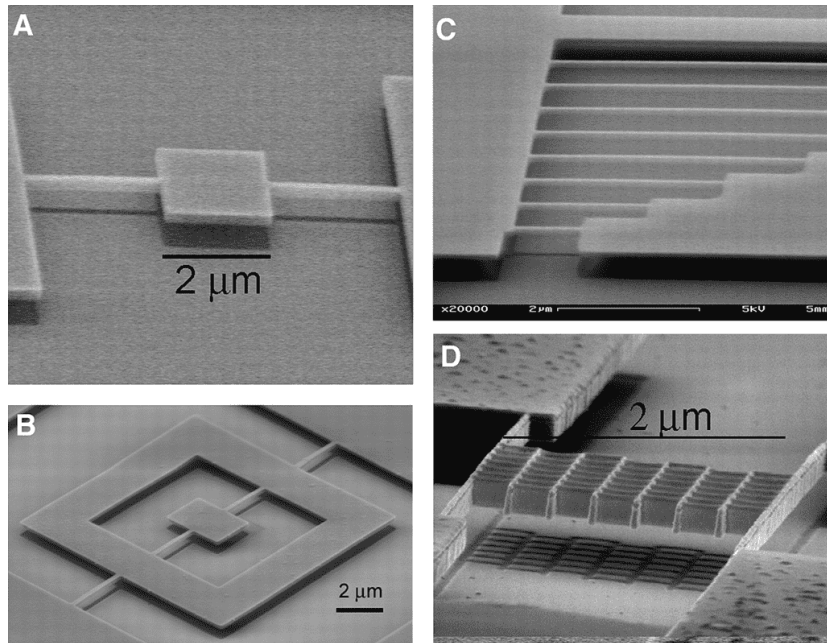


Figure 1.12: Tilted plan view SEM Images of different silicon nanoelectromechanical systems realized by Electron Beam Lithography (EBL) and surface micromachining. In particular: A) a torsional oscillator, B) a compound torsional oscillator, C) a series of silicon nanowires, and D) an oscillating silicon mesh mirror. [76]

In Figure 1.12 different SEM images of several nanoelectromechanical systems from the review of H. G. Craighead [76] are reported. These devices were realized through an EBL process followed by metal deposition and different dry and wet etching processes. EBL arise as a very flexible method used in research to rapidly obtain nanoscale features without the need of very complex and dedicated equipments. Indeed, often the realization of a material design that results of interest for specific optical and/or electrical properties is initially studied by the use of EBL and later adapted to industrially suitable equipments. In fact, this method is strongly limited with respect to the total writing area achievable, that commonly is on the order of few centimeters, making it unsuitable for large scale production and industrial processing.

1.1.2 Metal-Assisted Chemical Etching

Metal-Assisted Chemical Etching (MACE) is a wet etching anisotropic approach catalyzed by the use of a high electronegative metal. MACE was first proposed and demonstrated in 2000 by Li and Bohn as a high anisotropic etching approach to obtain porous silicon [77]. In the first method, an Al covered Si wafer is etched by a solution of $\text{HNO}_3\text{:HF}$ as oxidant and etchant, respectively. Two years later Peng et al. demonstrated the possibility to realize a high density of vertically aligned Si NWs with this approach by using a $\text{AgNO}_3\text{:HF}$ aqueous mixture. This method is known as silver salts approach and take advantage of the silver nanoparticle precipitation onto the Si surface to catalyze the etching. Indeed, AgNO_3 act as an oxidant and a metal source. A selective oxidation process is driven by the metal and the SiO_2 formed underneath the metal NPs is etched by the presence of the HF. All the MACE processes are based onto these simple steps: i) discontinuous metal deposition onto the Si substrate, ii) selective oxidation underneath the metal as catalyst, iii) SiO_2 etching.

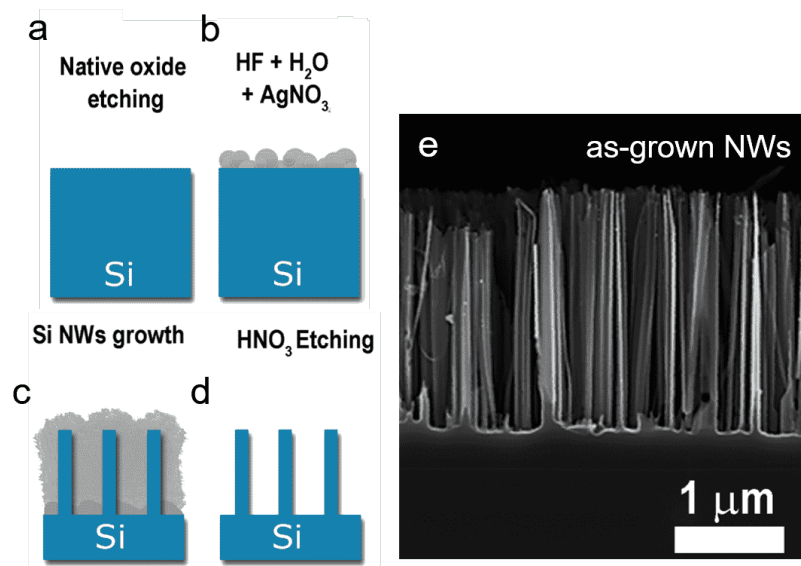


Figure 1.13: Scheme of Si NWs synthesis by silver salt MACE: a) native oxide etching, b) room temperature metal-assisted chemical etching, c) final sample before Ag dendrites removal, d) silver nitrate etching to remove the Ag dendrites. e) Cross section SEM of Si NWs realized by silver salts MACE.

In Figure 1.13a-d the scheme of the silver salts process is shown. In particular, after the etching of the native silicon dioxide a), the sample is immersed in an aqueous $\text{AgNO}_3\text{:HF}$ solution b). Ag NPs, with dimensions and density related to the starting silver nitrate solution, precipitate onto the Si substrate and catalyze the etching. The Ag nanoparticles (NPs) formed in solution are more electronegative than the Si and inject holes into the substrate that is oxidized due to the presence of radical NO_3^- . This MACE kinetics can be depicted as a galvanic cell. In particular, the Si plays the role of the anode and the metal of the cathode with a cell current production in the metal/Si interface during the etching process. Si NWs are formed in the Si uncovered regions and are covered by Ag dendrites as showed in Figure 1.13c. Finally, the sample is immersed in nitric acid solution and the silver dendrites are totally etched d). All the process is at room temperature and commonly no presence of silver contamination is attested in the Si NWs. In Figure 1.13e a typical cross-section SEM image of the realized Si NWs is showed. These Si NWs are realized by using a solution of 40% AgNO_3 (0.05 M), 20% of HF, and 40% H_2O . The average diameter of the realized NWs is about $70 \text{ nm} \pm 20 \text{ nm}$ [78] as usual by using the silver salt approach. This method is fast, doesn't need complicated sample preparation and is very cheap compared to lithography approaches. With respect to VLS is simpler to obtain a high density of Si NWs and doesn't require complicated equipments and high temperature. However, by using silver salts the Si NWs diameter is not suitable for quantum confinement effect and is limited to several tens ($>50 \text{ nm}$ commonly) of nanometers. Furthermore, during the process, the presence of Ag dendrites is attested onto the samples. These dendrites etch may affect and damage the Si NWs. A last critical point is the lack of control on the Si NWs pattern geometry.

In order to surpass the control lacking in the Si NWs array geometry, the MACE can be integrated in a lithography process by using ordered metal film as catalysts. In this way, a very high aspect ratio can be obtained surpassing the limit of 50:1 typical of DRIE. Indeed, different groups [79, 80] report the use of MACE by using high control patterned metal film obtained through EBL.

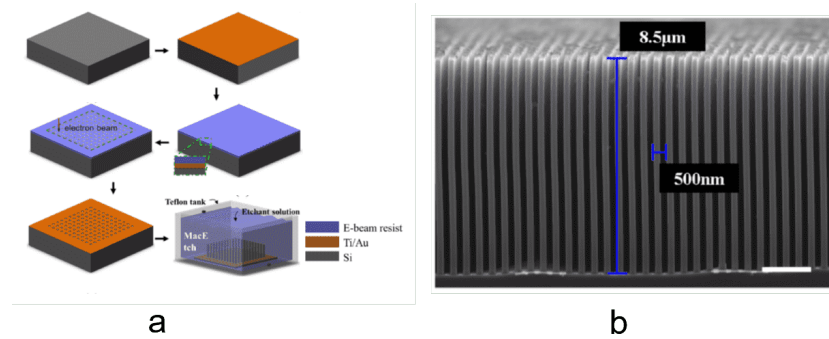


Figure 1.14: a) MACE process with EBL/RIE patterning of the metal catalyst scheme. b) Cross section SEM image of a Si grating realized by MACE with EBL/RIE patterning. [79]

A typical approach is obtained by depositing the metal in a previously patterned PMMA (exposed and developed). After the lift-off, the metal results structured as the negative of the PMMA mask. Another approach used by Li et al. [79] is by patterning the metal (Ti-Au) through a RIE process as shown in Fig. 1.14a. Initially, a 3 nm of Ti as an adhesion layer and 20 nm of Au is deposited by EBE in a Si substrate. The sample is then spun with PMMA and patterned through EBL. The pattern, realized through EBL, correspond to the final structure. In fact, the exposed metal is then etched by RIE and then the PMMA is removed. Finally, the sample is immersed in a H₂O₂:HF solution with the hydrogen peroxide used as oxidation agent. In Figure 1.14b a Si grating is showed by a cross section SEM. As it is possible to observe, a high aspect ratio is obtained with Si structures characterized by a length of 250 nm and a height of 21 μm. Despite this approach permits to achieve a high control on the Si structure geometry, quantum confined Si NWs remains very complicated to be obtained due to the resolution of few nanometers required by the EBL.

Metal thin film approach

In order to surpass the diameter limit of the Si NWs obtained by silver salt MACE, our group engineered an innovative metal thin film approach. In particular, few nanometers Au or Ag layer were successfully employed to obtain room temperature light emitting Si NWs.

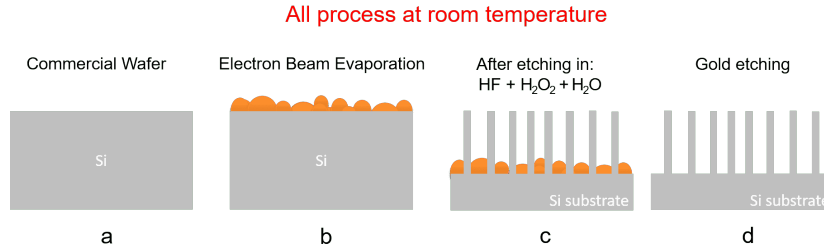
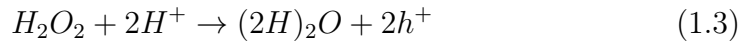
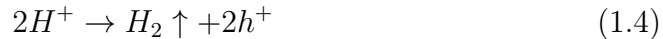


Figure 1.15: Scheme of Si NWs synthesis by thin film MACE: a) native oxide etching, b) thin metal film deposition by EBE, c) metal assisted chemical etching, d) gold etching. All the processes are at room temperature.

As shown in Figure 1.15, a discontinuous thin metal film is deposited by EBE on an oxide-free Si substrate b). The sample is then immersed into a solution of $H_2O_2:HF$ and the metal drive the oxidation just underneath the Si that is subsequently etched by the HF c). Silicon nanowires are realized on the uncovered region and the gold is finally removed by a gold etchant solution d). All the processes are at room temperature and the gold does not diffuse inside the silicon. In this method, the hydrogen peroxide is used as oxidation agent. As previously, we can consider the Si as a local anode with respect to the metal acting as cathode for the current produced in the Si/metal interface. The kinetic of the process is the following:

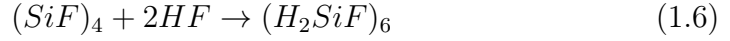
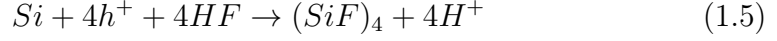


As suggested by the same fathers of this approach, Li and Bohn [77], and by other different studies [81], the cathode reaction happens as the usual reduction of protons into hydrogen:



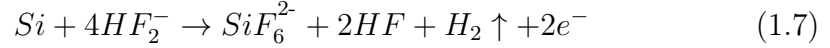
The reduction of the oxidant species generate holes that are injected inside the silicon underneath the metal. Hence, at the Si anode region, the silicon is oxidized and subsequently etched by the hydrofluoric acid. Three Si dissolution processes were proposed by the scientific community. However, up to now, none of them were in-situ experimentally demonstrated to work or to be favorite among the others. The dissolution models follow as reaction I,II, and III, respectively.

Reaction I (RI):



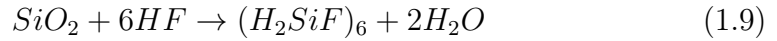
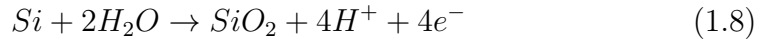
In the RI case, the Si is directly dissolved in a tetravalent state without forming the silicon dioxide.

Reaction II (RII):



In the RII the direct dissolution of Si is still present but in the divalent state.

Reaction III (RIII):



In this third model, the Si atoms in contact with the metal are oxidized and then dissolved in two different processes. RI differs from the other two involving a direct dissolution of Si (in a tetravalent state) with a gaseous formation without the generation of H₂. In the other two models the H₂ generation is followed by the dissolution of the oxidized species Si and SiO₂ in RII and RIII, respectively. The experimental evidence of bubbles formation during the etching process seems to suggest RII as the favorable model. However, all these three models result valid and probably a combination of all of them happens. The structural properties of the Si NWs obtained by this approach are well controllable.

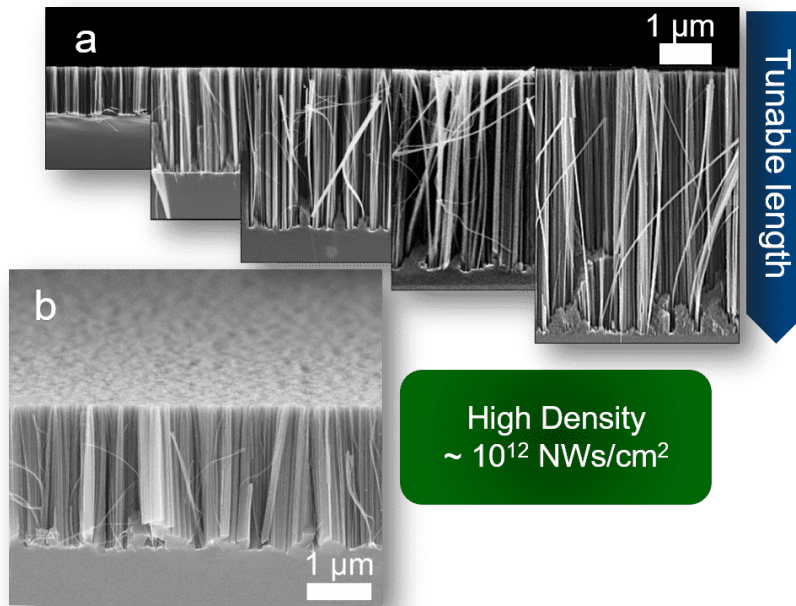


Figure 1.16: a) Cross section SEM images showing the possibility to tune the NWs length from hundreds of nanometers to several micrometers. b) Tilted Cross section SEM showing the high NWs density of about 10^{12} NWs/cm².

By changing the etching time is possible to vary the Si NWs length from few hundreds of nanometers to several micrometers as shown in Figure 1.16a. Therefore, as visible in b) the density of the Si NWs is huge, of about 10^{12} NWs/cm² and this is a crucial point for all the applications. The average diameters of the synthesized Si NWs is determined by the thickness and the type of the metal used as a catalyst. In fact, the thin metal layer is discontinuous and nanometric areas of uncovered silicon are present. The average dimension of these areas is determined by the material wettability and thickness. In particular, by using 10 nm of Ag, 2 nm of Au, and 3 nm of Au we demonstrated an average uncovered Si diameter of 12 nm, 9 nm, and 7 nm, respectively. These data were obtained by a statistical analysis performed by a SEM characterization of the different films. The dimension of the diameters of these uncovered Si holes is strictly related to the final Si NWs average diameters. In particular, the Si NWs average diameters for the different metal thin films were obtained through a Raman analysis of the

obtained samples.

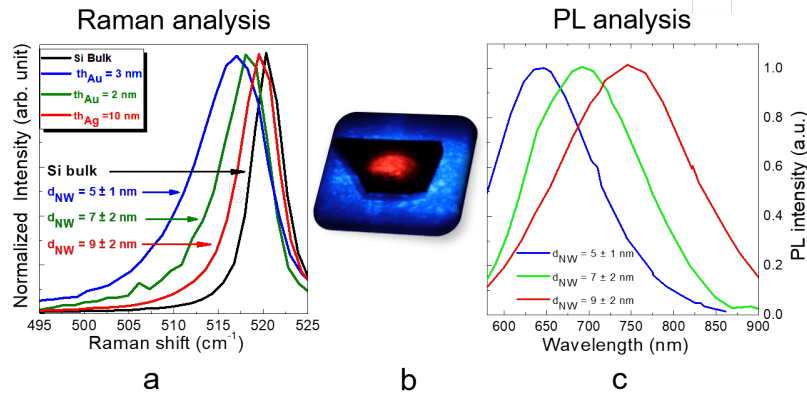


Figure 1.17: a) Raman analysis of the first order stokes silicon peak. The average Si NWs diameter is obtained for each different metal used by fitting this Raman peak with the Campbell-Fauchet model. b) Photo of the PL emission of the NWs sample excited by a defocused 10 mW 364 nm laser. c) PL spectra of the different NWs samples normalized to their peak.

In Figure 1.17a the Raman peaks of Si NWs array realized with different metals are reported. In fact, the Raman signal of the Si results asymmetrical due to the quantum confinement effect and fitting it by using the Campbell-Fauchet method [82] is possible to obtain the average Si NWs diameter for each metal used. Average diameters of 10 nm, 7 nm and 5 nm were obtained by using 10 nm of Ag (red line), 2 nm of Au (blue line) and 3 nm of Au (green line), respectively. These diameter dimensions were further confirmed by an accurate statistical TEM analysis. All these NWs sizes are enough to present quantum confinement effect. Indeed, the room temperature PL emission is attested by the photo in Figure 1.17b and result so bright that can be observed by naked eye. In this case, the PL is obtained by strongly defocalize a 364 nm laser light onto the Si NWs sample. In Figure 1.17c the emission of all the samples is reported demonstrating the quantum confinement nature of that. In fact, by increasing the average diameter of the Si NWs the PL is redshifted in perfect agreement with quantum confinement theory [25]. This thin metal film approach is cheap, fast, compatible with the Si industry, and permits to obtain vertically aligned and room temperature luminescent Si NWs. Another advantage is that the Si NWs crystallinity and the doping

are the same of the starting substrate and hence, perfectly controlled and known.

1.1.3 Conclusion

Si NWs are emerging in different field as an innovate building block to overcome different challenges from microelectronics to energetics, photonics, and sensing. Starting from microelectronics, a lot of effort was spent in the last years to find novel solutions that permits to overcome the limitations of the nowadays Moore's law. In particular, approaching the nanoscale dimension a natural field of research is the application of Si NWs as a channel for a Field-Effect-Transistor. Photonics with the integration of light and silicon, the two technology that more changed our century, is still considered an opportunity-rich and still not totally explored field. In particular, in order to surpass the limit of the bulk silicon as an indirect bandgap material strategies of quantum confinement have been investigated in these last 20 years. Different approaches were used to address this crucial point with the realization of defect emitting nanostructures as well as light-emitting porous silicon and nanocrystals. Despite the extraordinary amount of effort spent in this field, for most of the strategy proposed an industrial realization remain still lacking or very complex. Si NWs emerges as a very promising material able to successfully couple the light to an industrially compatible silicon nanomaterials. However, with the standard synthesis method, the realization of quantum confined Si NWs is very complex and require expensive equipments. Thin film Metal-Assisted Chemical Etching (MACE) has permitted us to successfully realize an array of luminescent Si NWs at room temperature due to quantum confinement effect. In order to present the advantages of this synthesis approach with respect to the literature, an accurate state of art on the most important top down and bottom up approaches for Si NWs growth has been shown. A special insight to the Vapor-Liquid-Solid (VLS) method was given due to the particular importance of this bottom-up approach as the first, and still the most important, Si NWs synthesis strategy. Despite the strong diffusion, this approach suffers of several drawbacks that strongly limit the application of the synthesized Si NWs. The most used catalyst remains the gold due to the high crystalline quality of the realized Si NWs and the simple thermodynamics physics of the Si/Au alloy. However, the high thermal budget required by this method determines several problems as a gold diffusion inside the Si NWs. The gold impurities act as trap levels

strongly increasing the Shockley-Read-Hall recombinations and affecting the performance of Si NWs in electrical, as well as optical applications. The doping is commonly realized during the growth, but due to the high temperature, a disuniform radial doping profile is obtained. The diameter dimensions are commonly limited to few tens of nanometers and, even if reaching the quantum confined dimension is possible, it leads to a lacking of the orientation control on the Si NWs growth. Several other catalysts were studied in literature but without solving the main issues of this approach and, in most of the cases, with a final lower quality with respect to the one achieved by using the gold. Several top-down processes for nanoscale features realization were analyzed in this chapter as well as their use for Si NWs realization. Reactive Ion Etching (RIE) and in particular, Deep RIE (DRIE) are commonly the most used etching approaches in order to obtain high aspect ratio structures. However, the high cost, the need of expensive dedicated equipments and the limit on 50:1 of aspect ratio determines the difficult to achieve quantum confined and high-density Si NWs array. Due to the strong interest in scientific research, as well as in the industrial community, different lithography processes were analyzed. Indeed, a lot of effort was spent in literature on the realization of ordered structure of Si NWs and these techniques can be integrated in a bottom-up, as well as in a top-down process. Finally, the MACE synthesis strategy was presented. This approach is based on a wet etching process driven by a metal catalyst deposited onto the surface of the silicon. Typically the process is at room temperature and no metal contamination is attested in the final nanostructures. Our group demonstrates the possibility to modify this approach with few nanometers metal film in order to obtain quantum confined and room temperature luminescent Si NWs with interesting perspectives for all the application fields.

Label-free luminescent silicon nanowires sensors

Abstract

SENSORS are revolutionizing our interaction with the world by enabling the access to informations beyond our senses. After the discovery of nanomaterials and their novel properties, the scientific community has focused a lot of effort on the realization of new nanomaterial based sensing platforms. In this scenario, the use of silicon, largely diffused in the microelectronics industry, may have a disruptive impact on the real commercial transfer of these technologies. Among all the possibilities, Si NWs emerges as a promising building block thanks to their huge surface to volume ratio, bright and stable luminescence, robustness, and Si-compatible cost-effective synthesis. Novel label-free sensing platform based on Si NWs luminescence for genome detection that doesn't require any DNA amplification by Polymerase Chain Reaction (PCR) will be presented. HBV affects today more than 300 hundred million people and is considered the main cause of liver disease with a widely diffusion especially in poor countries. For these reasons, HBV emerged as the perfect candidate to demonstrate the Si NWs sensing performances. This Si NWs platform demonstrates few copies of sensitivity for the detection of HBV with a strong selectivity tested with a different DNA and even in serum. The sensor was even tested with a real HBV genome extracted from infected human blood, demonstrating the same sensitivity of quantitative PCR but without the need of a chemical laboratory. Another extremely challenging

field that is attracting the interest of the scientific and industrial community is gas sensing. Different applications are emerging nowadays that span from the monitoring of air quality in industrial plants and at home to novel automotive and smart cities applications. One of the most dangerous and diffused compounds that affects air quality is the NO_2 . Indeed, nitrogen dioxide (and in general NO_x) is commonly produced in high-temperature combustion from industrial processes to car engines and can have a dangerous effect even at a concentration of 3 ppm. Our preliminary studies on bare Si NWs demonstrate the possibility to detect this toxic pollutant at a NO_2 concentration of 2 ppm even without heating the platform. These results are obtained by analyzing the luminescent signal variation of the sensor and appear promising for the realization of novel sensing platforms that are not affected by typical electrical sensor drawbacks as electric source noise.

2.1 State of art of optical sensing

Sensors are nowadays everywhere around us and they are becoming smaller, more efficient, and interconnected. In the next future, their number will exponentially increase with new health applications [41], novel environmental monitoring [83] and security solutions [84]. Over the past years, protein and genome analyses have played a crucial role with tremendous advances in different fields from genetics and biology research to health care and forensic applications. Moreover, different biomarkers have been discovered as a novel tool to fast and easy monitor the health state of a patient related to different diseases [85–89], revolutionizing the worldwide health care system. Commonly, these biomarkers are proteins or particular genome expressed as a consequence of a specific biochemical process related to a certain disease. The advantage of protein and genome sensing is that specific probes to detect these targets are already present in nature or can be designed. Immunoturbidimetric and nephelometric assay [90] are some of the simplest and extremely diffused approaches for protein analysis. These analyses are based on transmitted light intensity variation due to the scattering caused by the agglomeration of the antigen target with the specific antibody used as a probe. These methods are characterized by a limit of detection (LOD) of the order of few $\mu\text{g}/\text{mL}$ permitting a useful biomarker screening only in blood [91,92]. Another drawback of this clinical protocol is the occurrence of nonspecific binding of the antibody that follows in the agglomeration of several antibody/antigen molecules making very complex a correct light scattering data interpretation [93]. Moreover, the presence of non-specific binding can also affect the measure with false positive [94]. Among all the protein detection methods, the Enzyme-Linked Immunosorbent Assay (ELISA) emerged as one of the most reliable and sensitive approaches with a crucial impact, not only to the general biomedical research, but also to the biosensors field [95,96]. The ELISA method includes different strategies and variants known as direct, indirect, competitive, sandwich, and so on. All of these approaches are based on the selective binding of an antigen to its specific antibody. Among them, one of the most reliable and diffused methods is the sandwich one.

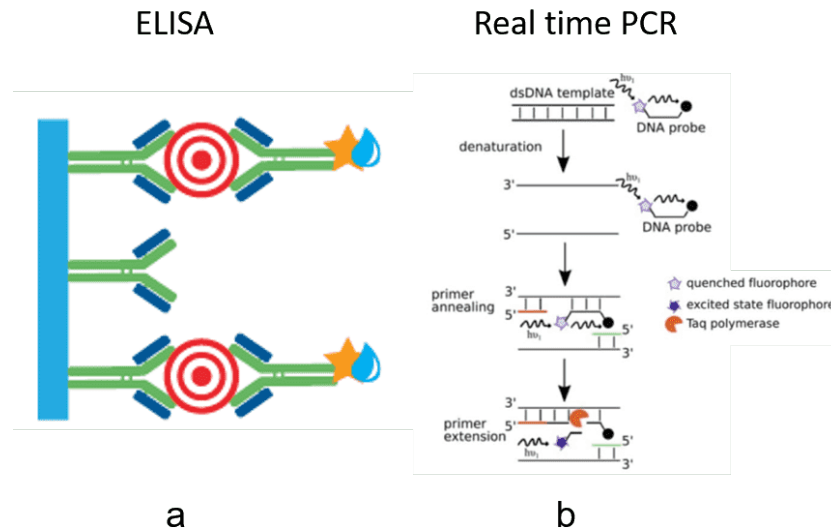


Figure 2.1: Scheme of direct sandwich ELISA working principle and real time PCR are shown in a and b, respectively.

In this method, the antigen target is labeled with the specific antibody to whom is attached an enzyme. The surface sensor is functionalized with the specific antibody and the labeled target, when captured, is sandwiched between the label and the sensor surface antibody (as schematized in Fig. 2.1a). The unbound molecules are washed off with several rinses in the buffer solution or deionized molecular grade water. The enzyme substrate is added in solution and interacts with the enzyme linked to the labeled antibody. As a consequence of the enzyme-substrate interaction, a fluorescent signal is emitted and its intensity represents the sensing mechanism. By using a sandwich Elisa assay, Canady et al. demonstrated a correlation between an enhanced level of keratinocyte growth factor in the sera of keloid and scleroderma affected patients. The detection limit of ELISA is commonly limited to the 10^{-4} $\mu\text{g}/\text{mL}$ [97] that commonly correspond to a pM limit (depend to the molecular mass) [23]. This LOD is a limit to enable novel sensing applications, as for example non-invasive analyses that require pM or lower sensitivities [98–102]. Moreover, the enzymes or the fluorophores used as tagging are unstable with time and extremely sensitive to the solution environment, causing information loss by photobleaching. This quenching effect by molecule agglomeration dramatically affects the detection efficiency and

reliability of this approach [96].

Another approach that revolutionized the medicine, as well as the genome diagnostics, is the Polymerase Chain Reaction (PCR) and the following invention of real-time PCR method for quantitative genome analysis [103, 104]. This approach permits high-sensitive and quantitative detection of DNA targets in a totally closed system, minimizing cross-contamination issues by using fluorescence transduction as sensing method [105, 106]. Indeed, real-time PCR is still considered the gold standard for genome analysis as proven by its large use in a plethora of applications including determination of viral or bacterial loads in clinical samples, identification and titers of germs in food, diagnosis of tumors, gene expression analysis, and forensic analyses. This approach is based on the PCR reaction and is also known as quantitative approach (qPCR). In the qPCR, the sensing mechanism is represented by the fluorescent signal emitted by a sequence-specific oligonucleotides probe (primer) labeled with a fluorescent dye when it captures a PCR product of the analyte. More in details for each qPCR cycle (Fig. 2.1b): i) the double stand DNA (dsDNA) is denatured into the 2 complementary single stands (ssDNA); ii) the PCR amplification of the DNA occurs and follows the annealing of the primer that polymerase with a segment of the ssDNA in a new DNA double stand; iii) the primer is separated by the fluorescent dye causing its light emission. The limit of detection is commonly around 10 DNA copies per reaction (cps) in a volume of hundreds of microliters [107, 108]. However, complex instrumentation, qualified personnel, and specialized laboratories are required. These aspects, combined with the high cost of the analysis, limit the PCR pervasion and its use for a large-scale screening and early diagnosis applications. In general, the realization of fast and simple sensors that can be used outside of a hospital, even at home, represents one the major priorities in the “Grand Challenges for Global Health” [109]. Moreover, severe limitations are present in the third world and developing countries where the biochemical infrastructures are scarcely diffused and suffers from several limitations as power supply, cost constraints, and characterized by poor hygienic conditions. In this scenario, the availability of easy-to-use and low-cost methods for biomarkers analysis as well as genome diagnostic still represents a priority task.

To overcome these drawbacks, a new class of label-free optical biosensors is currently under investigation. Such biosensors rely on the direct detection of an optical, electrical, or acoustic signal, generated by the binding of the untreated target to the functionalized sensing interface. Indeed, label-free

measurements are faster, easier to perform and, the response is more reliable. To face this demand of label-free reliable, cost-effective, simple, high-selective, and sensitive sensors, novel nanomaterial-based solutions emerged in these years. Indeed, there was an exponential growth of the research on innovative sensors based on semiconductor and metal nanostructures. The innovative nanomaterial properties, as well as their increased high surface to volume ratio, make nanotechnology a strategic tool to surpass the standard sensor limits [110–113]. However, despite these remarkable properties, nanostructured biosensors are scarcely commercially diffused due to the high production cost and the often incompatibility of their synthesis approaches with the current industrial technology. In this picture, quantum confined nanostructures [114] are emerging as novel biosensing platforms due to their high surface-to-volume ratio along with their bright, stable, and tunable luminescence [115, 116]. In particular, light emitting quantum dots (QDs) have been proposed by several groups as promising label-free optical biosensors with sensing mechanism as photoluminescence (PL) quenching, shift, or enhancement [117].

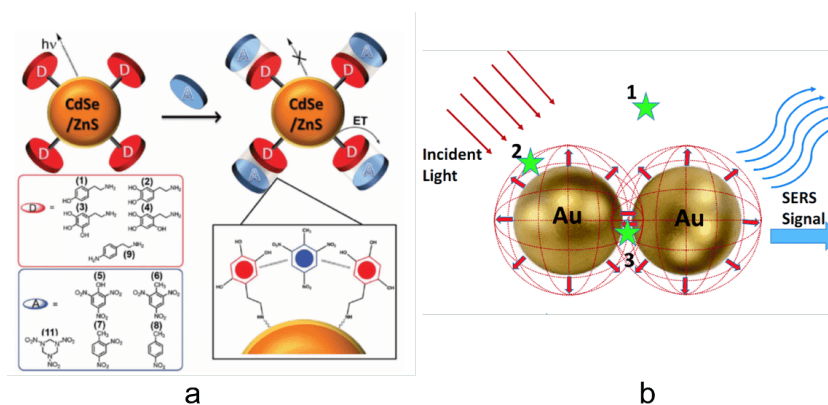


Figure 2.2: Fluorescent quenching sensor based on CdSe nanoparticles. [118]
 b) Raman enhancement scheme by Au nanoparticles SERS sensor. [119]

In figure 2.2a the scheme of a luminescent CdSe/ZnS Qds sensor is reported. In this case, Freeman and coworkers demonstrate a detection limit of 100 pM of nitroaromatic or $C_3H_6N_6O_6$ (RDX) explosive sensing [118]. The sensing platform is realized by covalently links CdSe/ZnS to a series of electron donors as tyramine (1), dopamine (2), 5-hydroxydopamine (3), and

6-hydroxydopamine (4) (as reported in Fig. 2.2a). The sensing mechanism is the PL quenching of the QDs luminescence that the authors demonstrated as caused by an energy transfer occurring through the particles and the target gas. As another example, by using CdSe QDs functionalized with tert-butyl-n-(2-mercaptoethyl)-carbamate a $1.1 \mu\text{M}$ cyanide detection has been demonstrated [117]. Apparently, the detection limit of label-free QD optical sensors is generally limited to the nM range [114, 117]. Such low sensitivity limits their use for more advanced applications in non-invasive assays requiring ultralow sensitivity down to the pico and femtomolar (fM) range [98–102]. One of them is the CRP detection in saliva, which necessitates a LOD below 850 fM [98, 120, 121]. Another critical point is that, Se and Te are toxic and the use of heavy metal species (Pb, Cd, Zn) is generally avoided in the microelectronics industry. In fact, the diffusion of these elements inside a device drastically affect its performances. Furthermore, it is extremely complex and inefficient to electrically excite QDs and, aside from optical pumping, their implementation in optoelectronics devices is strongly limited. Another interest label-free optical sensing approach is the Surface Enhanced Raman Scattering (SERS) sensing. In this method, metal nanostructures as Au or Ag nanoparticles (NPs), are used to enhance the Raman scattering of the target. In fact, the Raman scattering provides a unique fingerprint of the investigated material permitting to identify and quantify the target with a label-free approach. However, this approach is strongly limited to the low cross section (10^{-30} cm^{-2}) which often in presence of target fluorescence (i.e. dye cross section 10^{-15} cm^{-2}) implies a too low signal to be correctly distinguished and analyzed. This issue can be surpassed by the SERS approach where the Raman scattering is enhanced thanks to the formation of collective modes of the conductive electrons called Localized Surface Plasmon modes (LSP). Hence, the sensing mechanism relies on the Raman scattering enhanced by the resonant optical coupling of the incident electromagnetic field to the LSP. As showed in Fig. 2.2b, metal nanoparticles locally enhance the near field permitting to reveal the Raman signal of the molecules close enough to them (molecule 2 and 3 and not molecule 1 in the Figure 2.2b). Another advantage is that this analysis can be performed even in liquid permitting to analyze the biomolecules in their physiological conformation state [112]. In SERS analysis, a crucial parameter is the Raman enhancement that determines the increase of the Raman signal in the SERS substrate with respect to the standard Raman scattering of the target. The use of SERS sensing is widely diffused in literature for several application

fields, from biosensing to pollution analysis, and even in cultural heritage. In the review of Wei et al. many SERS applications on pollutants, dyes, explosives, and biomolecules sensing are reported [119]. Commonly, the detection limit reported for all these applications is in the μM -nM range [113] with few applications down to 100 pM [119]. As elicited, the Raman signal is specific for each molecule and commonly no functionalization of the sensor is needed. However, in most of the case of different big molecules, like protein or DNA, several functional groups are present and distinguish between two similar biomolecules is extremely complex. Another problem for big molecules is that the hotspot region is too small compared to the molecule dimension. In these case, functionalization procedures are also used in order to catch the target species at a specific distance from the surface, permitting to enhance the Raman signal of the interested functional group. Another advantage of the functionalization is the possibility to wash out other biomolecules by simple buffer or water rinse procedures. As elicited, for the case of big molecules the SERS Raman enhancement result limited due to the difficulties to couple the near field effect with the big dimension of the target. In fact, the Raman scattering enhancement obtained by LSP is commonly limited to few nanometers. As an example, in literature is reported how by using an Ag SERS substrate the Raman signal of the CH_3 group of an alkanethiol molecule decreased by a factor of 2 when the distance between target and substrate increased from 0.8 nm to 2.5 nm [122]. For real applications, solid SERS substrates are often considered more reliable with respect to the liquid ones [119]. However, commonly the preparation of these substrates relies on complex, expensive, and not large scale compatible approach as electron beam lithography, focused ion beam lithography, and nanosphere lithography [119]. Moreover, the analysis of the Raman spectra generally requires expert personnel and the data elaboration is not trivial. Despite the remarkable properties of all these nanostructured biosensors, in general they remain scarcely commercially diffused. Without taking into consideration each single detection strategy, a common drawback is the high cost of the materials and the often incompatibility of their synthesis approaches with the current microelectronics technology. In this scenario, the use of silicon, largely diffused in the microelectronics industry, may have a tremendous impact on the real commercial transfer of these technologies.

2.2 Silicon sensing platforms

Several groups demonstrated very high sensing performances by using silicon nanowires (NWs) in a Field-Effect Transistor (FET) configuration. In these type of sensing platforms, a single Si NWs is used in a FET architecture permitting to obtain a detection limit that surpass the picomolar concentration limit [123, 124]. In particular in these structures, Si NWs are used as FET channels and are functionalized to catch the desired target.

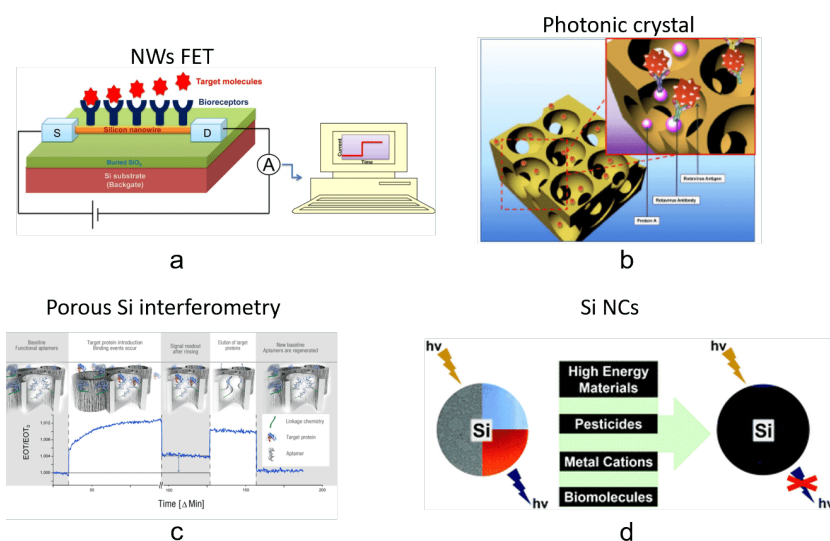


Figure 2.3: Schematic working principle of several Si-based sensors. Si NWs FET, 3D photonic crystal, porous Si, and Si nanocrystals are reported in a) [125], b) [126], c) [127], and d) [128], respectively.

As shown in Fig. 2.3a, when the analyte is captured by the probe it affects the conductivity and so the resistance of the device. The resistivity change is the sensing mechanism and common LODs in the pM–fM range [125] are reported with the possibility, as demonstrated by the Lieber’s group, to detect even single virus [40, 41]. As an example, McAlpine et al. have demonstrated a 220 attomolar LOD for DNA sensing (about 6600 DNA copies per 50 μL) by using a Si NWs FET sensor with Si NWs having diameters under 20 nm [129, 130]. More interestingly, this group showed the possibility to implement up to 24 NWs FET onto a single sensing interface by Superlattice Nanowire Pattern Transfer (SNAP) for high throughput and multiplexed

biomolecule detection in a microfluidic circuit [131]. Despite the incredible sensitivity of this class of sensor, for what concerns the genomic analysis they require amplification of the DNA target through a PCR process limiting their application in specialized facilities. Another strong drawback of these sensors is the poor working range that strongly limits their application in real context hindering the realization of a real medical platform. These sensors result complex to integrate into ICs (integrated circuits) due to the challenges of electrically address individual wires and integrate with conventional manufacturing processes. Moreover, the high background noise of such devices may limit their sensitivity in more complex environments. Their fabrication result very expensive and commonly they integrate a microfluidic system whose manufacturing make the device even more very complex and expensive. All these aspects make these platforms not suitable for a large industrial production. Another interesting strategy present in literature is the use of Si Photonic Crystals (PC) as sensor platforms. In these systems, as shown in Fig. 2.3b, a photonic crystal structure is employed as transducer taking as sensing mechanism the shift of the reflected peak wavelength value [126]. A PC is designed as a dielectric periodic arrangement that causes the formation of a wavelength bandgap for the light inside the material. By using a broadband light source, this corresponds to a typical wavelength peak reflected by the photonic crystal. This peak depends on the characteristics of the ordered crystal structure as the typical dimension of the periodic elements, the space between these elements, and their refractive index. In the 3D case shown in Fig. 2.3b the ordered elements are air sphere inside a dielectric matrix. After the functionalization of the Si PC, a first shift of the peak wavelength value appears. The sensing mechanism relies on the refractive index variation when the target is captured by the probe. Fauchet's group [132] demonstrate a nM sensitivity by using CMOS compatible microring PC resonator. The typical microring structure is implemented with a PC by realizing a periodic air circles chain. The advantage of this structure is the extreme simplicity and the possibility to realize it with CMOS standard UV lithography. After the functionalization of the sensor, the capture of the target corresponds to a red shift of resonator transmitted wavelength. In this case, the light is coupled to the sensor by a waveguide making the realization of this sensor expensive and complex. In general, the realization of a PC is commonly expensive and the detection limit is comparable to the ELISA Kit already present on the market [132, 133]. Despite the silicon is an indirect band gap material, the quantum confinement effect permits to engineer the

optical properties according to the structural characteristics [134–136]. This effect permits to obtain light emission at room temperature (RT) from silicon nanostructures as Si quantum dots (QDs) [137], porous Si [138, 139], and as recently demonstrated from Si NWs [140]. Nonetheless, the use of porous silicon or Si QDs luminescence as the detection mechanism is scarcely reported due to the poor and unstable luminescence [137, 141]. Indeed, porous silicon (pSi) is commonly present in literature as an optical sensor platform based on the refractive index variation occurring when the analyte is captured by the pSi functionalized surface. Urmann et al. [127] obtained a μM LOD by using a pSi interferometric sensor (Fig. 2.3c). A porous silicon Fabry Perot thin layer is functionalized to be selective to polyhistidine tagged proteins. The sensing mechanism relies on the change of the Effective Optical Thickness (EOT). When the target is captured by the probe introduce a refractive index change and so, a variation of the EOT. The common LOD for these sensors is in the μM range [127, 142]. As reported by Wu et al. [143], Si nanocrystals (NCs) with different surface modification are mostly used as nano light source for in vivo cell imaging and drug delivery system. However, Si NCs are becoming an interesting alternative to Cd-based system due to the possible release of toxic Cd^{2+} ions [128]. Amine-terminated Si NCs were used for mercuric ions sensing with a detection limit of 50 nM. The sensing mechanism is a fluorescence quenching caused by the introduction of new non-radiative de-excitation levels. Other group reported the use of Si NCs in a Fluorescence Resonance Energy Transfer (FRET) configuration with a 1 nM LOD for trinitrotoluene (TNT) detection. In this type of sensor when the target is captured the fluorescence of the NCs decrease and as a consequence due to an energy transfer process the fluorescence signal of the target (or the dye-labeled target) increase. In general, the LOD of these Si NCs appears to fall in the nM range, limiting the applications of these platforms for higher sensitivity applications. In this scenario, 1D materials as Si NWs emerge as a more easily integrable solution with the standard technology and offer a more robust platform with very high aspect ratio and exposed surface [113, 144, 145]. We have demonstrated the realization of thin Si NWs synthesized by a cheap, fast and industrially compatible approach with room temperature (RT) luminescence due to quantum confinement effect [21, 25].

2.3 Sensing based on silicon nanowires luminescence

In these last years, we have demonstrated the realization of the first sensor based on the room temperature (RT) Si NWs photoluminescence (PL). In particular, a Si NWs-based platform for the detection of the C-reactive protein (CRP) has been carried out. CRP is an acute-phase protein related to an inflammatory condition of the human body and in a specific range of concentration is the main biomarker of a heart failure pathology [146–149]. In developed countries, cardiovascular diseases are the second major cause of death. This makes the realization of fast, easy to use, high sensitive sensors a priority demand as prevention instruments for primary health care analysis that can be performed even at home [150]. The standard methods for CRP detection are the immunoturbidimetric or nephelometric assays [90]. By these approaches, CRP is with a common LOD of 1 $\mu\text{g}/\text{mL}$ permitting a useful analysis for cardiovascular disease only in blood serum [91,92]. In fact, as well known from the literature, the CRP concentration in blood related to a high-risk occurrence of infarction is above 3 $\mu\text{g}/\text{mL}$ while concentrations under 1 $\mu\text{g}/\text{mL}$ are typical of a healthy patient [147]. In this picture, an analysis method that can be performed at home in a non-invasive matrix as the saliva can have a tremendous impact on the myocardial infarction prevention. However, the CRP concentrations in saliva related to the same risk factors measured in serum are about four orders of magnitude lower, below 10^{-4} $\mu\text{g}/\text{mL}$ (850 fM) [98] and undetectable by the standard techniques. Room temperature luminescent Si NWs appears as a promising solution due to their robustness, bright luminescence, and huge surface to volume ratio. In order to realize a high selective sensor for the CRP, the specific antibody (Anti-CRP) was chosen as the probe. As the first step, the streptavidin (SA) was used to bridge the Si NWs with the biotinylated Anti-CRP (Ab). Indeed, the bound between SA and biotin is the strongest non-covalent one known.

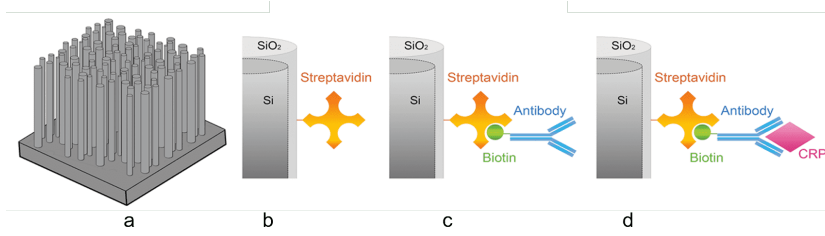


Figure 2.4: Si NWs functionalization process for the C-reactive protein (CRP) detection. a) as-synthesized Si NWs, b) functionalization of Si NWs with streptavidin b), and subsequently functionalization with biotinylated anti-CRP. After this step the sensor is obtained and was tested with different CRP d). [23]

All the functionalization steps are shown in Fig. 2.4. Two different concentration of SA and Ab were used realizing two different operating range sensors. In particular, by using $10 \mu\text{g}/\text{mL}$ of SA and $50 \mu\text{g}/\text{mL}$ of Ab a detection limit suitable for the CRP analysis in saliva was achieved. After the Ab functionalization, the sensor response was studied in a wide concentration range spanning from $10^{-9} \mu\text{g}/\text{ml}$ to $10^2 \mu\text{g}/\text{mL}$.

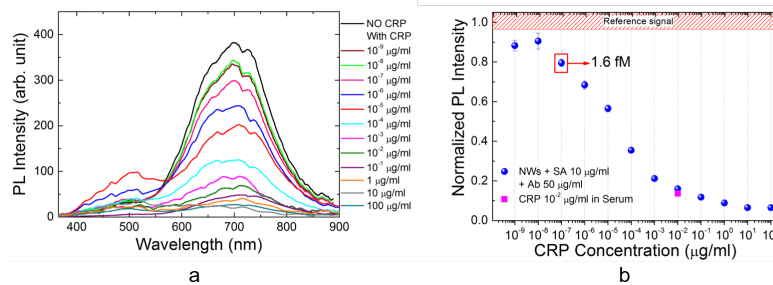


Figure 2.5: a) PL spectra obtained at room temperature for the sensor tested in different CRP concentrations. The black signal is the reference PL of the sensor without CRP b) Calibration curve obtained as the integrated Si NWs PL signal and normalized to the reference as a function of the CRP concentration. The red dashed bar represents the PL reference. In pink the signal of the Si NWs sensor obtained with $10^{-2} \mu\text{g}/\text{mL}$ of CRP in serum is reported. [23]

In Fig. 2.5a the sensor PL spectra obtained in these different CRP solu-

tions are shown. In particular, in black is reported the reference spectrum of the sensor without CRP. It is possible to observe as increasing the CRP concentration follows a decreasing of the PL. This PL quenching represents the sensing mechanism of the sensor and it is due to new non-radiative levels introduced by the captured CRP [23]. The integrated PL of the Si NWs de-convolved contribution is reported as a function of the CRP concentration to obtain the calibration curve shown in Fig. 2.5b. Hence, only the Si NWs contribute is considered to build the calibration curve. As shown by the calibration curve the sensor operating range is huge and go from a femtomolar limit that corresponds to 10^{-7} $\mu\text{g}/\text{mL}$ up to 1 $\mu\text{g}/\text{mL}$. This wide operating range with this LOD permits a saliva analysis to avoid a heart attack occurrence. This type of analysis is less invasive and can enable a lifesaver prevention analysis that can be performed even at home. The sensor selectivity was demonstrated by different negative testes. Moreover, the sensor was even tested with a known CRP concentration dissolved in human serum. Despite a large number of other proteins and biomolecules present in this complex matrix, the PL signal obtained, shown in pink in the calibration curve, was the same observed in buffer demonstrating the high selectivity of the sensor [23]. This has been the first proof of a new class of label-free sensors based on Si NWs luminescence. The same protocol adopted for the CRP can be used for other biomarkers. Once obtained these such good performances, we decided to test this platform for other strategic sensing applications.

2.4 Label- and PCR-free DNA sensing based on luminescent silicon nanowires

Since the DNA clearly evidence in 1953 and thanks to the human genome project, the genomic research played a crucial role in biology, as well as in novel disruptive health care applications. Nowadays, the genomic research still represents one of the most important fields in medicine where, just as an example, incredible efforts are being focused on cancer understanding and treatment. Furthermore, different rare mutations and diseases are related to the genomic heritage of the patient and genome analysis plays a strategic role in the research, prevention, and early treatment procedures. However, nowadays DNA analysis is not just related to medicine and biology but took place in wide of different fields as forensic analyses and sanitary control in the food

industry. As introduced at the beginning of this chapter, Real-time PCR has been and continues to be the genome analysis gold standard. However, this approach requires complex equipments, is expensive, time-consuming and cannot be performed outside specialized biochemical laboratories. All these points limit the pervasion of the genome screening and early diagnosis on a large scale. A simple and cost-effective approach that can be used outside a hospital is an imperative demand for third world country and home-analysis applications.

Nanostructured silicon sensors are the ideal platform to push the genome analysis on a large scale. After the success with the CRP, a such important application field appear of tremendous interest for the realization of a novel Si NWs sensor. Until now, the luminescence quenching of Si NWs for genomic recognition has been still unexplored and detailed studies on the sensing mechanism based on the light emission by NWs upon DNA capture are lacking. Hepatitis B virus (HBV) was chosen in order to test the Si NWs performances in the genome recognition applications. HBV infects today over 3 hundred million people worldwide and it is one of the major causes of liver diseases and liver cancer [151, 152]. This motivates the choice of HBV as the target for the first test of this Si NWs sensor.

2.4.1 Functionalization procedure

In order to guarantee the sensor selectivity, HBV complementary genome sequence probes were used. These two probes are able to cooperatively hybridize the HBV genome. The binding of the probes to the Si NWs is obtained by using the (3-glycidyloxypropyl) trimethoxysilane (GOPS) as a bridge. Si NWs were obtained by using the metal-assisted chemical etching approach with 2 nm of discontinuous Au layer. As presented in details in the 1.3.1 paragraph, with this approach is possible to obtain quantum confined Si NWs that present photoluminescence (PL) emission at room temperature (RT). A n-type ($\rho \approx 1\text{-}5 \Omega \times \text{cm}$) Si bulk substrate was UV Ozone-treated for 2 min and then immersed in a HF 2.5M aqueous solution in order to obtain an oxide-free Si surface. The 2 nm gold substrate was deposited by an electron beam evaporation at room temperature. The sample was then etched in a 5M HF and 0.44M H₂O₂ aqueous solution. Au acts as a catalyst driving the Si etching only under the gold and, at the end of the process, the uncovered Si regions will form the Si NWs. Finally, the Si NWs sample was immersed in a gold etching solution to remove the Au layer.

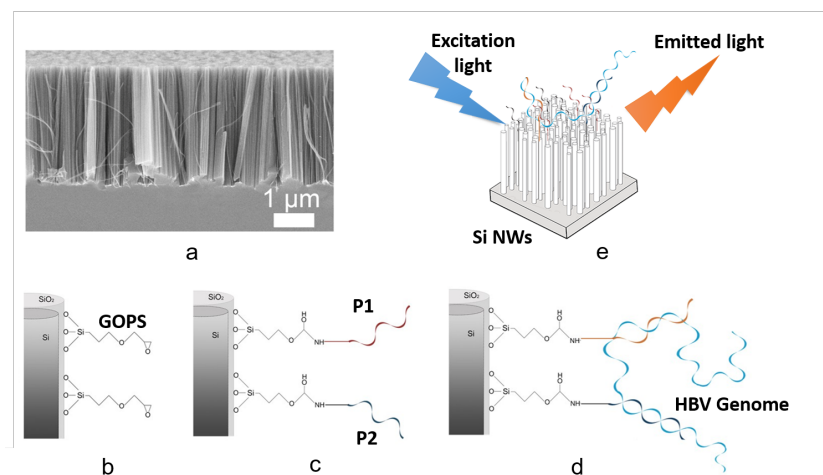


Figure 2.6: a) Cross section SEM image of the starting Si NWs with a length of about $3 \mu\text{m}$. Schematic illustration of the NWs surface functionalization: b) silanization of the Si NWs surface with GOPS after the cleaning procedure, c) NWs sensor reference obtained after the anchoring of two specific complementary probes for HBV probes P1 and P2, and d) capture of HBV by the probe P1 and P2 due to cooperative hybridization. e) Sketch of the NWs optical sensor operating principle. [24]

All the approach is at RT and a cross section Scanning Electron Microscopy (SEM) image of the as-grown Si NWs is shown in Fig. 2.6a. The as-synthesized Si NWs were functionalized with a three process step: (i) cleaning step, (ii) vapor phase silanization, and (iii) probe anchoring process. All this protocol is schematized in Fig. 2.6b-d. i. The Si NWs samples were first cleaned for 2 min in an isopropanol bath, rinsed in water for other 2 min, treated with UV ozone for 5 min, washed another time in water (2 min), and finally dried by nitrogen flux at room temperature. This cleaning procedure guarantees the removal of any biological contamination from the Si NWs promoting the uniform formation of the external silicon oxide thin surface. Indeed, the SiO₂ layer improves the hydrophilicity of the NWs which is an advantage for the functionalization [23]. ii. The cleaned samples were exposed to 10 mL of GOPS at 120 °C for 4h in a low vacuum chamber (200 mbar). After this process, Si NWs results chemically modified by a GOPS layer (Fig 2.6b). This silane is used to produce an epoxy-terminated Si NWs surface able to covalently react with amino-terminated P1 and P2 probes.

iii. After cooling at room temperature, the silanized samples were immersed for 4 h in 20 μM of both P1 and P2 probe (Fig. 2.6c) dissolved in a 150 mM phosphate buffer solution with pH 9.2 and at a temperature of 30 ± 1 $^{\circ}\text{C}$ [153]. After that, the samples were washed three times with molecular biology reagent-grade water to remove all the unbound probes and dried by nitrogen flux. The samples were stored at room temperature until use. After these three steps, the samples represent the sensors and were tested with different HBV solutions. In general, around 100 μL of HBV solution was applied onto the reaction area of 3×3 mm^2 of the Si NWs sensor obtained after the 2nd step consisting in the P1/P2-modified-NWs sensor. First of all, the HBV genome denaturation was carried out by heating the solution with immersed the Si NWs sensor for 4 min at a temperature of 90 $^{\circ}\text{C}$ with the different HBV genome solutions. In order to perform the hybridization reaction, the samples were heated for 2 h at 50 ± 0.1 $^{\circ}\text{C}$. After that, the samples were washed three times in molecular biology reagent-grade water and dried with a nitrogen flux (Fig. 2.6d). The cross-reactivity of our system assay was investigated by testing the sensors in a human serum matrix. Moreover, to further address this point, the sensors were tested with an unspecific target consisting of a *Mycobacterium tuberculosis* clone genome with the same protocol. The working principle of the Si NWs PL quenching is sketched in Fig. 2.6e. In order to demonstrate the success of the cooperative hybridization process and the HBV presence on the Si NWs sensor Raman scattering and Attenuated Total Reflectance IR (ATR-IR) measurements were carried out. The genome capture by the sensor, as well as the correct probes functionalization, were attested.

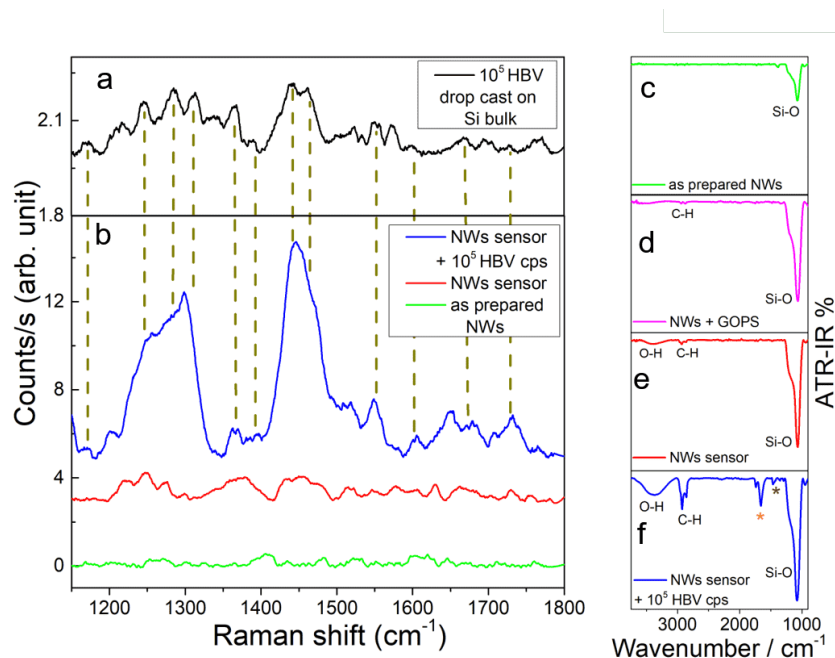


Figure 2.7: a) Raman spectrum of 10^5 HBV copies (cps) drop-cast (5 times on the same point) onto Si bulk wafer without any functionalization is shown in black as a reference for the Raman peak identification of the HBV presence. b) Raman spectra of as-prepared Si NWs (green line), NW sensor after the functionalization procedure (red line), and after the adsorption protocol with 10^5 HBV clone cps in buffer (blue line) are shown in the spectral range of interest for HBV recognition. ATR-IR spectra of c) as-prepared Si NWs (green curve) and d) functionalized NWs after GOPS silanization (magenta line), e) Si NWs sensor (red line), and f) Si NWs sensor with 10^5 HBV (blue line). [24]

Fig. 2.7a-b shows the Raman spectra of as-prepared Si nanowires (green line), of the same NWs sample after the functionalization procedure with P1 and P2 probes (Si NWs sensor, red line) and after HBV adsorption protocol (Si NWs sensor with HBV, blue line). All these spectra are reported in the range of interest for genomic recognition from 1150 to 1800 cm⁻¹. In particular, the characteristic features associated with amide-I band (1560–1600 cm⁻¹), amide III band (1200–1300 cm⁻¹) of HBV genome [154], and the strong double peak at 1440 and 1460 cm⁻¹ due to the C–H deformation typical of

biomolecules are distinguishable from the spectrum of Si NWs sensor with HBV. We also compared this vibrational pattern of the NWs sensor with HBV (blue line) to the Raman spectrum of the same DNA drop casted on a Si substrate and then dried (procedure repeated 5 times on the same point) shown as a black line in Figure 2.7a. It is noteworthy that we can recognize the same spectroscopic contributions, although the better-defined Raman signal coming from HBV in NWs sensor (blue line in Figure 2.7b) is affected by small shifts and different relative intensity ratios of the Raman bands which lead to a more evident convolution of the spectroscopic features compared to those revealed in Figure 2.7a. This is due to the different conformations of the HBV copies in the two samples: a less chaotic one assumed when HBV is captured by the Si NWs sensor with respect to those assumed by the same genome when it is drop-casted several times on Si substrate, on which it forms a sandwich layer. The Raman measurements were carried out using the 633 nm line of a He laser beam through a 50X LWD objective (NA 0.5) and a 100X objective (NA 0.9) with a power of 1.5 mW onto the samples. The signals were acquired in a backscattering configuration through a Jobin-Yvonne HR800 spectrometer by using a Peltier cooled (-70°C) CCD. To further support this Raman analysis an Attenuated Total Reflectance IR (ATR-IR) spectroscopy was carried out for all the protocol steps and for the HBV immersed sample. IR spectra related to as-prepared Si NWs (green curve), functionalized NWs after GOPS silanization (magenta line), Si NWs sensor (red line), and Si NWs sensor with HBV (blue line) are shown in Figure 2.7c-f, respectively. As demonstrated by the bands identified at $\approx 1070\text{ cm}^{-1}$ with a small shoulder at $\approx 1200\text{ cm}^{-1}$ as-grown Si NWs present a surface oxide layer. These two peaks represent the Si-O asymmetric stretch (AS) modes. As expected, the silanization process led to a remarkable decrease in ATR-IR% of asymmetric Si-O stretching modes (magenta line). Moreover, weak bands relevant to asymmetric and symmetric C-H stretching at ≈ 2945 and 2875 cm^{-1} can be identified and attributed to alkyl chain of GOPS. In the NWs sensor (Figure 2.7e), the anchoring of p1 and p2 probes occurs and can be visualized in the IR spectrum (red curve) in terms of the decrease in ATR-IR% of C-H stretching modes and their slight shift to lower wavenumbers as for the formation of a more packed layer. Additionally, the presence of O-H stretching at $\approx 3390\text{ cm}^{-1}$ is indicative of a certain hydration of single-stranded DNA. ATR-IR analysis confirmed the successful hybridization of DNA probes in Figure 2.7f for NWs sensor tested with HBV. In fact, the intense bands between 1740 and 1650 cm^{-1} can be

undoubtedly ascribed to C=O, C=N stretching, and exocyclic-NH₂ bending vibrations of the DNA bases (orange asterisk). Moreover, purine ring mode was identified at 1460 cm⁻¹ (brown asterisk). Unfortunately, the characteristic signals such as the stretching modes of PO₂ group related to the DNA phosphodiester backbone (1080, 1230 cm⁻¹) could not be discriminated due to the Si-O stretching bands. However, the slight shift to lower wavenumber and the significant decrease in ATR-IR% of O-H stretching band indicates the capture of HBV DNA in Figure 2.7f. IR spectra were acquired by a Spectrum Two PerkinElmer FT-IR spectrometer equipped with a diamond crystal (wavelength range 4000–500 cm⁻¹, resolution 2 cm⁻¹, 16 scans). Raman and ATR-IR fully demonstrated the successfully HBV capture by the designed probes. After the functionalization testes, the PL signal of the sensor in different HBV clone solutions was acquired.

2.4.2 Sensing performances

In order to demonstrate the sensing performances, this Si NWs platform was tested with 2, 20, 200, 2000 and 10⁵ cps in 100 μL of HBV clone solution, consisting in the typical PCR calibration range. The signals were acquired in a backscattering configuration through a Jobin-Yvonne HR800 spectrometer by using a Peltier cooled (-70°C) CCD and exciting with a 364 nm of an Ar⁺ laser. All the PL measurements of the sensors were performed 10 times in different points of the same sample and repeated for several sensors for each HBV concentration both in serum and in buffer. In Fig. 2.8a the PL spectra measured at room temperature are reported. The black spectrum is obtained from the sensor immersed in buffer without any HBV copies and represent the sensor reference. Increasing the HBV cps the PL signal decreases. It is noteworthy that the signal obtained at 2 cps result distinguishable with respect to the sensor reference. After 2000 cps the signal shows a saturation trend. In order to demonstrate the selectivity of the sensor, this platform was tested with 20, 200, 2000 cps in human serum and the obtained PL spectra are shown in Fig. 2.8b. Indeed, the human serum is a complex matrix rich of other proteins, DNA and in general biomolecules. The reference spectrum obtained as the sensor signal in human serum without HBV is shown in black. In Figure 2.8a and b) is possible to observe the decrease of the PL signal increasing the HBV concentration in both matrix. Another series of peak around 400-600 nm appear in human serum and can be ascribed to this complex matrix. To demonstrate that, a Si bulk substrate was functionalized

and immersed in the same human serum solution without HBV. The PL signal obtained from the Si substrate after each functionalization step was analyzed permitting to assign the 400-600 nm peaks to the serum matrix.

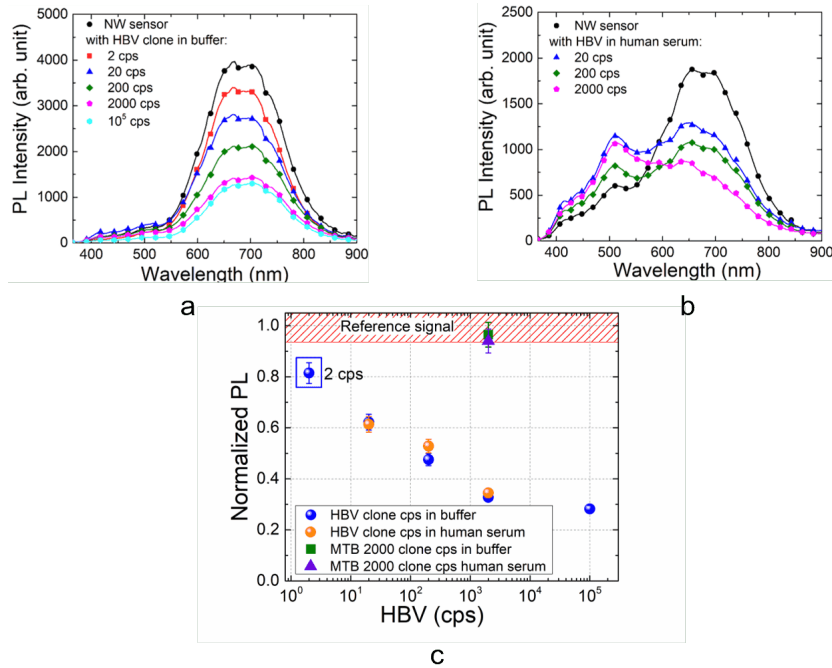


Figure 2.8: PL spectra of the NWs sensors obtained for different HBV clone concentrations tested in buffer solution a) and human serum b). PL reference spectra of the NWs sensors without any HBV copies are shown in black for both of them. The calibration curve showing the PL integrated peaks of the NWs sensors as a function of HBV clone concentration in buffer (blue dots) and in serum (orange dots) is shown in c). For each HBV concentration, the PL integrated peaks are normalized for each reference signal (red dashed region) of the sensor. The green square shown in c) is the PL integrated peak (normalized to the buffer reference signal) of the NWs sensor tested for 2000 Mycobacterium Tuberculosis (MTB) clone cps in buffer, while the violet triangle is the PL integrated peak (normalized to the human serum reference signal) of the NWs sensor tested for 2000 MTB clone cps in human serum. [24]

In Fig. 2.8c the calibration curve of the sensor is reported. In particular,

the PL signal of the HBV cps in buffer and in serum are shown as blue and orange dots, respectively. The reference signal is reported as a red dashed bar and for the blue and orange points represent the PL reference of the sensor without any HBV cps immersed in buffer (PBS) or in serum, respectively. The sensor signal obtained in the buffer (blue dots) is the integrated PL signal of the Si NWs sensor normalized to the reference. As is possible to observe the sensor shows a detection limit of 2 copies with a PL decrease of 19% with respect to the reference. For each order of magnitude of HBV cps increases, corresponds a further PL quenching of the 20%. Between 2000 and 10^5 cps the PL variation is just the 4% showing a saturation trend. It is noteworthy the LOD reached of 2 cps is even better than the common detection limit declared for qPCR analysis corresponding to 10 cps [107, 108]. After the identification of the 400-600 nm peaks to the more complex matrix, the integrated PL signal of the sensor was obtained by considering the only contribution of the Si NWs. This PL signal normalized to the reference in serum as a function of the HBV cps (orange dots) represents the calibration curve of the sensor in serum. As is possible to observe, this signal perfectly matches the PL quenching obtained in buffer, demonstrating that the selectivity of the sensor results not affected by the solution matrix. This point is crucial for a real medical sensor. To further confirm the selectivity of the sensor, we tested the Si NWs platform in 2000 cps of *Mycobacterium tuberculosis* (MTB) in both buffer and serum. The obtained PL quenching is undistinguishable with respect to the reference signal demonstrating how the sensor responds only to the HBV. To undoubtedly prove the performance of this platform in real medical use, this sensor was tested with real HBV cps extracted from infected human blood and dissolved in buffer. The DNA length of the clone and the real sample is different due to the HBV clone synthesis procedure. Indeed, the clone DNA samples consist in 7.144 Kbps while the real sample is just 3.3 Kbps.

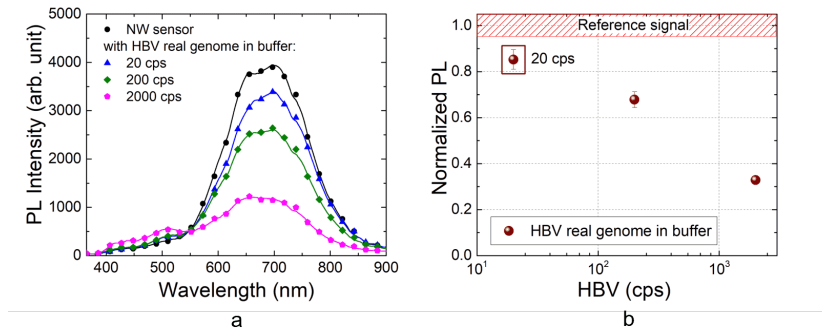


Figure 2.9: a) PL spectra of the NWs sensor tested in HBV real genome extracted from infected human blood and spiked in buffer. The PL reference of the sensor without any copies of HBV is shown in black. b) Trend of the PL integrated peak of the NWs PL emission as a function of real HBV genome concentration and normalized to its PL reference signal (red bar). [24]

In Fig. 2.9a the PL spectra analysis obtained with 20, 200, and 2000 real HBV cps is shown. In black, as usual, is visible the reference signal of the sensor acquired after a buffer immersion without any HBV cps. Increasing the HBV cps a further PL quenching is observed. In particular, in Fig. 2.9b the integrated PL signal as a function of the real HBV cps is reported. The red dashed bar is the signal of the sensor without HBV. A 15% PL quenching correspond between 20 cps and the reference. The same PL quenching ratio is attested for 200 cps and a 35% further decrease is visible between 200 cps and 2000 cps. It is worth to note that this Si NWs platform is able to detect the real HBV genome with a LOD of 20 cps comparable to the real-time PCR, even when the genome length is about half of the analytical sample [24]. In conclusion, the proposed Si NWs platform has proven to reach a remarkable LoD of 2 cps for synthetic genome in a buffer solution and 20 cps with the real genome. It is noteworthy that the Si NWs sensor is able to detect without any label and amplification step the HBV in a biological matrix at high complexity, like serum, where there is the presence of a huge amount of possible interfering molecules, such as proteins or nucleic acids. Moreover, the designed functionalization protocol based on cooperative hybridization for the DNA capture is very versatile and can be used for the specific detection of other different genomes. The realization of the Si NWs, as well as the functionalization protocol, is fully compatible with the stan-

standard microelectronics industry. These aspects combined with the sensitivity, easy detection method, and low manufacturing cost permits the development of a competitive miniaturized device for genome analysis outside a biochemical laboratory. All these points are key factors for the future development of a new class of genetic point-of-care devices that are reliable, fast, low-cost, and easy to use for self-testing including in developing country context.

2.5 Gas sensing

The interest of the scientific community and industry in gas detection has continuously become more important since the industrial revolution. In fact, the born of the industry follows with an exponential production of different toxic gas as CO, CO₂, NO_x, NH₃, and several hydrocarbon compounds. As a consequence, due to the effects of these toxic gases on human health gas detection start to become a priority demand. It is worth to note that the use of air quality detectors born in the 19th century. Indeed, during this century one of the first detection method employed by the coal miners relied on the sing of canaries down to the tunnels. The stop of canary singing or eventually its dead was used as an alarm for a toxic high presence of carbon dioxide, carbon monoxide, and methane. Nowadays, gas sensors play an important role in many applications from industrial air quality monitoring to novel automotive and smart cities applications. Indeed, air quality control is crucial for several industrial fields such as refineries, pharmaceutical manufacturing, fumigation facilities, paper pulp mills, aircraft, and shipbuilding facilities, hazmat operations, and waste-water treatment facilities [155]. This list is not limited to only industrial activities and workers can be exposed to toxic gases in operations such as painting, fumigation, fuel filling, construction, excavation of contaminated soils, landfill operations, and in general confined spaces works. Finally, the air quality at home or inside vehicles as well as in big cities has attracted a lot of effort for the realization of novel cost-effective, fast and sensitive device. Since the 1960s, many research activities have been addressed to resistive semiconductors oxide gas sensors. Since the development by Taguchi of a sensor based on SnO₂ [156, 157], this class of sensors gained more and more attention and many semiconducting materials have been investigated and analyzed. As in biosensing innovative nanomaterial solution are emerging with the promise of high sensitivity, low cost, and low power consumption [158, 159]. Among all the toxic compound a special

role is occupied by CO and NO₂. The risk related to CO is commonly well known, it is a molecule able to poison the red globule occupying the oxygen position and hence, causing even in small quantity as tens of ppm, a serious risk for health. Nitrogen dioxide is another environmental pollutant produced during high temperature combustion process in industrial factories as well as in automotive engines especially in the diesel ones. This gas can lead to deterioration and olfactory paralysis [160] even with an exposure of about 3 ppm for more than 8 hours daily. In confined environments such as automotive cabin, garage parking or tunnels, high concentrations (> 3 ppm) are a serious health hazard. In this scenario, the realization of cost-effective, selective, sensitive and reliable gas sensing platform for the detection of NO₂ (and in general NO_x) is an open challenge.

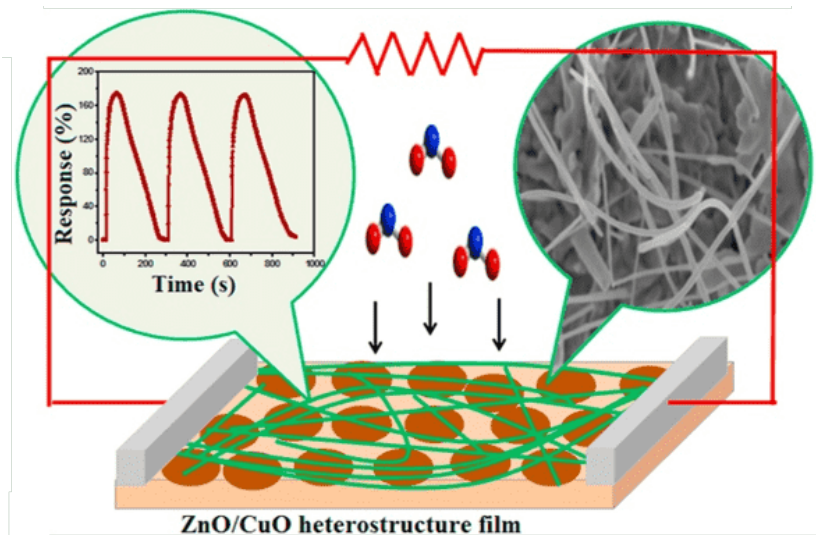


Figure 2.10: Schematic illustration of the ZnO NWs/CuO nanoparticles sensor working principle. [160]

In Fig. 2.10 the typical working principle of a semiconductors oxide sensor is schematized. In particular, the image shows the nanomaterials-based device used by Navale et al. characterized by 1 ppm of NO₂ detection limit with an optimal temperature of 150°C [160]. The sensing mechanism relies on the resistivity change of ZnO nanowire/CuO nanoparticle heterostructures. In this device, CuO nanoparticles are covered by a disordered hank of ZnO nanowires, as showed in the SEM image inset. In this type of sensors, the

operating temperature is a key factor influencing the gas molecules adsorption/desorption onto the sensor surface. Despite this sensor had an optimal response at 150°C, most of the semiconductors oxide resistive sensors shown the operating temperature in the 300-400°C range with as consequence typical high power consumption. Moreover, harsh environments are a challenge for resistive gas sensors, since poisoning or deterioration of the gas sensitive materials may happen by aggressive compounds like SO₂ or NO_x [157]. Optical sensors are commonly considered the best solutions in literature due to their excellent sensitivity, selectivity, and durability [158] but also very expensive. Another advantage of optical sensing is to be immune to electromagnetic and electrostatic interference. Indeed, electric sensors are affected by noise source such as high power source, electric engine, and in general AC sources, making necessary expensive signal filtering solutions. Silicon nanowires have demonstrated remarkable performances in biosensing emerging as a natural candidate for a novel optical Si-based gas detector. Indeed, Si NWs sensors are realized with Si-compatible and cost-effective approach permitting to surpass the drawback of the standard optical sensors.

2.5.1 Si nanowires luminescence sensing

A n-type ($\rho \approx 1\text{-}5 \Omega \times \text{cm}$) Si NWs sample was realized following the method described in the 1.3.1 section and shortly discussed for the DNA sensor in the previous paragraph. In order to test the Si NWs bare sensing performance based on their PL quenching a spectroscopic analysis in a gas controlled chamber was carried out. The sample was inserted in a closed environment linked to a gas controller and the excitation and emission signal acquiring were obtained through a quartz window. The PL experiment was performed using a Jobin-Yvonne HR800 spectrometer by exciting the Si NWs with a 476 nm Ar⁺ laser at a power of about 100 μW in a backscattering configuration with a long working distance 50X LWD objective.

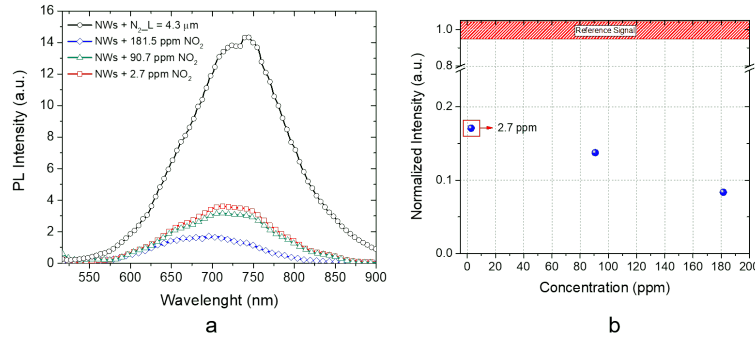


Figure 2.11: a) PL spectra of the Si NWs gas sensor tested with NO_2 obtained at room temperature. In black is reported the reference signal of the sensor after its stabilization under N_2 300 sccm flux. b) Sensor calibration curve obtained as the integrated PL signal normalized to its reference as a function of the NO_2 concentration.

In Fig. 2.11a the PL spectra obtained at room temperature for the Si NWs tested with different NO_2 concentrations are reported. The Si NWs sample was inserted into a volume gas chamber with a controlled N_2 flux of 300 sccm for several hours obtained by using a certified bottle and a mass flow controller. After an initial PL variation due to the different environment condition (humidity, other gas desorption) the sensor shows a stable PL signal reported as a black line in Fig. 2.11a. Gas coming from a certified permeation tube was diluted with the N_2 flux in order to obtain the desired ppm NO_2 . The gas flow and so the concentration was chosen by using a mass flow controller. The sensor was tested after 15 min of target gas exposure for each NO_2 concentration. After that, in order to purge the sensor a 300 sccm N_2 flux was applied to the chamber and the PL signal returned to the reference one in about 40 min. In order to avoid false signals response due to sensor poisoning, the Si NWs sample was tested starting from the smaller concentration to the higher ones. Moreover, all the PL spectra are the average of more than 5 measures in different points of the sample and the results were replicated by using another different sample. As usual, the integrated PL signal normalized to the reference as a function of the NO_2 concentrations is the calibration curve shown in Fig. 2.11b. The platform demonstrated to be sensitive up to 2.7 ppm of NO_2 with a PL quenching of about 72% with respect to the reference. A further decrease of 5% is attested for each 90 ppm

of NO₂ increase up to 180 ppm. Despite the small PL variation between the different NO₂ concentration, the sensor shows a signal to noise ratio higher than 5 with less than 1% of PL variation during the measurements. This Si NWs sensor shows interesting performances and is able to detect the strategic level of nitrogen dioxide to avoid high health risk. Furthermore, these are to be considered only preliminary measurements. It is noteworthy that this Si NWs platform was tested at RT were commonly these type of sensor require a temperature of several hundred of °C. As a natural follow of this project, these sensors will be tested at different temperature up to 100°C in order to strongly decrease the response and the purging time of the sensor. Furthermore, the temperature commonly plays a key role in the type of gas response permitting to make the sensor active for only a certain class of gas. About this point, as well reported in literature, another interesting strategy to increase the sensitivity and selectivity of a gas sensor and to a specific class of gas is related to the surface chemical modification. In this case, the Si NWs were tested without any functionalization and in future, the use of different chemical surface modification will be studied. Furthermore, the realization of an array of Si NWs sensor with each of them functionalized to respond to different classes of gas may be a promising strategy to realize a low-cost sensing platform for air quality monitoring.

2.6 Conclusion

Sensing applications are continuing to attract more and more interest in these years. The discovery of different proteins and genome strictly related to the health state of a patient with respect to a specific disease made the realization of novel sensing strategies a crucial demand. In particular, despite several reliable solutions already exist and are applied in hospitals, the realization of high sensitive devices that can be used outside a biochemical laboratory and even at home may change the health care industry with great advantages for the patient. A state of art for the standard strategies was presented showing the limits that are making the realization of new sensing platforms a global interest challenge. In this scenario, nanostructures with their novel properties and huge surface to volume ratio emerged in research as the natural candidate to surpass the today technology limits. However, as presented in this chapter, despite the remarkable properties of all these nanostructured biosensors, they still remain scarcely commercially diffused. Biomarkers and

genome recognition applications require higher sensitivity that surpass the picomolar limit and in certain case up to few DNA copies. Moreover, a common drawback is the high cost of the materials and the often incompatibility of their synthesis approaches with the current microelectronics technology. In this scenario, the use of silicon, largely diffused in the microelectronics industry, may have a tremendous impact on the real commercial transfer of these technologies. Silicon nanowires sensors were deeply investigated by the scientific community demonstrating a detection limit that surpasses the picomolar limit. However, these sensors are characterized by a small operating range that strongly limits their real application. 1D materials as Si nanowires (NWs) emerge as a more easily integrable solution with the standard technology and offer a more robust platform with very high aspect ratio and exposed surface. After have shown the realization of quantum confined luminescent Si NWs synthesized by a cheap, fast and industrially compatible approach we demonstrated their remarkable performance as optical sensors. In particular, we designed a novel sensing platform based on Si NWs luminescence for the detection of genome. Nowadays, genomic analysis and quantification play a crucial role in plenty of fields from medicine where, incredible efforts are being focused on cancer, different rare mutations diseases, forensic applications and food sanitary control analyses. Real-time PCR is the genome analysis gold standard but requires complex, expensive, and time-consuming equipment. Moreover, it cannot be performed outside specialized biochemical laboratories. All these points limit the pervasion of the genome screening and early diagnosis on a large scale. A simple and cost-effective Si NWs sensor that can be used outside a hospital was presented. This platform was tested for the Hepatitis-B Virus (HBV) detection. Indeed, HBV affects 300 million people worldwide, most of them in the third world countries making the realization of a DNA sensor that can be used without a expensive laboratory a critical demand. After have shown the success of the functionalization by Raman and ATR-IR analyses, the sensor was tested with the synthetic genome in buffer and in serum and with real HBV extracted from infected human blood. In all the cases, this Si NWs platform shown a detection limit of a few genome copies without amplification even in a complex matrix like the human serum. Another extremely challenging field that is attracting the interest of the scientific and industrial community is gas sensing. Different applications are emerging nowadays that span from the monitoring of air quality in industrial plants and at home to novel automotive and smart cities applications. All these different sectors have in common the demand of inno-

vative, cost-effective, fast, and high sensitive gas sensor devices. One of the most dangerous and diffused compounds that affects air quality is the NO_2 . Indeed, nitrogen dioxide (and in general NO_x) is commonly produced in high-temperature combustion from industrial process to car engines and can have a dangerous effect even at a concentration of 3 ppm. Recently, nanomaterials semiconductors oxide sensors are emerging due to their low-cost production, small dimension, and high sensitivity. Despite this activity is at its beginning, preliminary studies have already demonstrated the possibility to detect this toxic pollutant at a concentration of 2 ppm even without heating the Si NWs platform. The Si NWs were tested without making advantage of further chemical modification of the surface and this strategy remain to be explored for the future. The sensor performances are obtained by analyzing the luminescent signal variation of the sensor and appear promising for the realization of novel sensing platforms that are not affected by typical electrical sensor drawbacks as electric source noise. In conclusion, these sensors have shown remarkable high sensitive and selective performance for the detection DNA with the possibility to be employed out of specialized biochemical laboratories and even at home. Furthermore, the functionalization protocol adopted permit high flexibility for the realization of Si NWs sensor selective to different biomarkers and genome targets. First testes with gas demonstrated promising performances even without any applied temperature and chemical functionalization of the surface for the nitrogen dioxide detection. All these points are key factors for the future development of a new class of sensor based on Si NWs luminescence that are reliable, fast, low-cost, and easy to use for biomarkers and genome analysis, as well as gas sensing applications.

Artificial 2D random fractal based on silicon nanowires

Abstract

IN this chapter the realization of 2D Si NWs fractal arrays and their peculiar optical and structural properties are reported. 2D random fractal arrays of Si NWs were able to foster a widely angular spread CBS cone demonstrating the strong light trapping inside the material. Furthermore, Si NWs fractal arrays permitted the first observation of coherent backscattering of Raman light (RCBS) that emerged as a new all-optical process able to partially break reciprocity in reverse light paths across a disordered medium. Moreover, we present the realization of a new system obtained by coupling a fractal Si NWs array and Er:Y₂O₃. Both the two systems are extremely appealing in the Si photonics field. By a cost-effective and Si industry compatible process the fractal Si NWs were realized and decorated with Er:Y₂O₃. We demonstrated that the strong light trapping inside the fractal array determines a high enhancement of the Er emission. Moreover, this Er:Y₂O₃ Si NWs platform demonstrated different Er light-emission intensity as a function of the wavelength by simply changing the fractal morphology that drive the system scattering.

3.1 Fractal charm

In 1733 Jonathan Swift wrote: “So, Nat’ralists observe, a Flea /Hath smaller Fleas that on him prey,/ And these have smaller yet to bite ‘em/ And so proceed ad infinitum”. Probably even Swift wouldn’t image that this superb analogy was also a perfect example of a fractal. Fractals are everywhere around us.

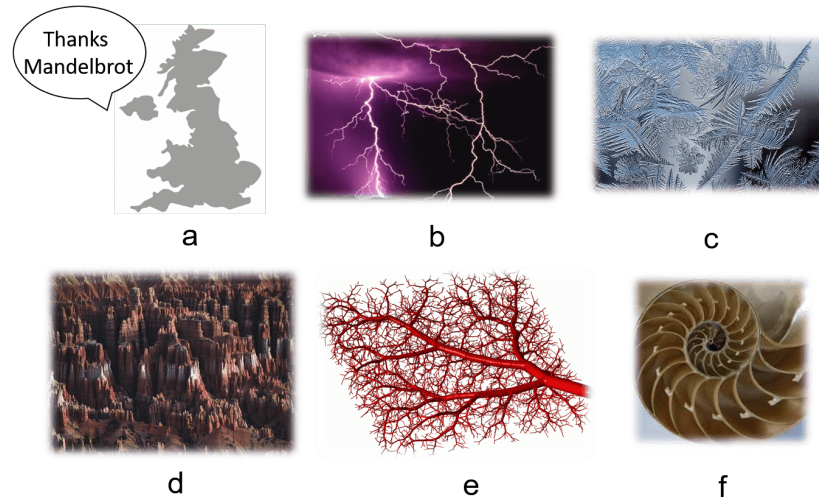


Figure 3.1: Several example of natural fractals. In order: a) UK coastline, b) lightning trajectories, c) ice crystals geometries, d) mountains ranges, e) circulatory system, and f) nautilus shell.

As shown in Figure 3.1, just by taking a close look to nature, the coastline of UK (and not only the UK one), the trajectory of the lightnings, the geometry of the ice crystals, the mountains ranges, our circulatory system, and the nautilus shell are only few examples of fractals. A mathematical fractal is an object characterized by a self-similarity behavior and that present the repetition of the same geometry at all the lengthscales (scale invariance) [161,162]. For a real object, these characteristics are present on a limited set of observation scales and this is the reason why sometimes they are also called protofractal. The introduction of the concept of fractal by Mandelbrot in the 70s has a huge impact on a plethora of fields [163,164]. Nowadays, the study of fractals is of large interest not only for physics, chemistry, and engineering but even for financial and sociology applications [21,165–168]. A

simple way to measure a length, a surface, or a volume is to cover it with a certain number of a segments, a squares, or cubes, respectively. Let's suppose that we want to measure a surface. In this case, we can count the number of square box N with fixed length needed to cover all the object. In general, to measure an Euclidean d -dimensional object, a d -dimensional box characterized by a length ϵ is used.

$$M = N\mu = N\epsilon^d \quad (3.1)$$

Where M indicate the measure of this d -dimensional object. In the literature, M is also known as the measure of the mass of an object. However, this measure fails for fractals. As the most famous example used by Mandelbrot we can just think to the UK coastline. In this case, we could think to measure its length by using a certain number of segments with a fixed length. However, if we try to measure this very jagged coastline with the method introduced we will find that its measure depends on the segment length chosen. By changing the segment dimension from several hundreds of km to a few meters the length of this coastline will result every time different. In the last century, the mathematician community face this type of problems, as for example with non-rectifiable curves, and defined a new generalized concept of measure or dimension. Among them, one of the most famous one is the Hausdorff-Besicovitch dimension. In particular, if we want to measure the mass on an object $\mu = \epsilon^d$ with unknown d we can take ϵ^α as unit of measure. As example, for the simple case of a square ($d=2$) with side L we know that $M = L^d = N\epsilon^d$, that implies $N = L^d/\epsilon^d$. Hence follows that:

$$M = N\mu = N\epsilon^\alpha = L^d\epsilon^{\alpha-d} = L^2\epsilon^{\alpha-2} \quad (3.2)$$

If we try to measure the length of a square ($\alpha=1$) we will find $M \rightarrow \infty$ and for the volume ($\alpha=3$) $M \rightarrow 0$. The square area is obtained only for $\alpha=2$ that is the same dimension of a surface. This method can be applied for any real α and in general the measure M is defined as:

$$M = \inf\{\alpha : M(\alpha) = 0\} = \sup\{\alpha : M(\alpha) = \infty\} \quad (3.3)$$

The Hausdorff-Besicovitch dimension is the α^* that make jump the measure from 0 to ∞ [161]. A simple method to obtain this dimension for a real object is the box-counting method. Starting from the Hausdorff notion of dimension $= N(\epsilon)\epsilon^\alpha$:

$$\alpha = \frac{\ln M - \ln N(\epsilon)}{\ln \epsilon} \quad (3.4)$$

That follows by taking the logarithm of the equation 3.2. The fractal dimension $D_f = \alpha^*$ by the definition in 3.3 is:

$$D_f = \lim_{\epsilon \rightarrow 0} \alpha = \lim_{\epsilon \rightarrow 0} \frac{\ln N(\epsilon)}{-\ln \epsilon} \quad (3.5)$$

Indeed, M is a finite number and $\lim_{\epsilon \rightarrow 0} (\ln M / \ln \epsilon) \rightarrow 0$. In more practical terms, for example a surface is covered with boxes of fixed dimension ϵ and by decreasing this length the slope of the regression $\ln N(\epsilon) / -\ln \epsilon$ for $\epsilon \rightarrow 0$ is taken as fractal dimension. Mandelbrot was the first to understand that the concept of the Hausdorff-Besicovich dimension can be applied to several objects present in nature. Thanks to its work this measure become widely spread to characterize a fractal.

Fractals are emerging in physics due to a variety of remarkable phenomena such as superconductivity, superdiffusivity, and non-linear optics effects present in these structures. Moreover, among other types of material fabrication, random fractal spontaneously arise in nature permitting to avoid expensive and time-consuming nanofabrication approaches. During the past years, different approaches of surface nano and microscale design arise in order to manage the light inside a material. Indeed, an area of key interest is the control of light propagation inside a material. In this picture, disordered materials are emerging as easy-to-fabricate designs, often leading to optical performances superior to those offered by ordered photonic structures. The random media ability to promote multiple scattering in a wide wavelength range is potentially useful to develop next-generation optical devices. The random media ability to promote multiple scattering in a wide wavelength range is potentially useful to develop next-generation optical devices. In fact, in field as photovoltaics, the trapping of light inside the material is of crucial interest to reduce the cost of the produced energy [19]. All these aspects have driven the realization of a 2D random fractal of Si NWs with the extremely advantage to be compatible with the current Si industry [21].

3.2 Synthesis of silicon nanowires fractal arrays

In the thin metal Metal-Assisted Chemical Etching (MACE) the Si NWs array is obtained as the negative mask of the starting discontinuous metal film. In particular, the gold acts as a catalyst and drive the process of silicon etching. The Si underneath the gold results etched while the uncovered silicon will form the Si NWs. Hence, a strategy to obtain a particular texture

of the Si NWs must involve the engineering of the Au film. In literature is well known that a percolative gold layer is a 2D random fractal [169]. A percolative gold layer is characterized by the appearing (or disappearing) of infinite extent connected regions that permit to always identify a path connecting the edges of the considered area [170,171]. The percolation threshold depends on the filling factor, defined as the ratio between the filled area by the material with respect to the total area. In general for the Au, according to the deposition and substrate condition, a filling factor between 50 and 60% is related to the percolation threshold [172,173].

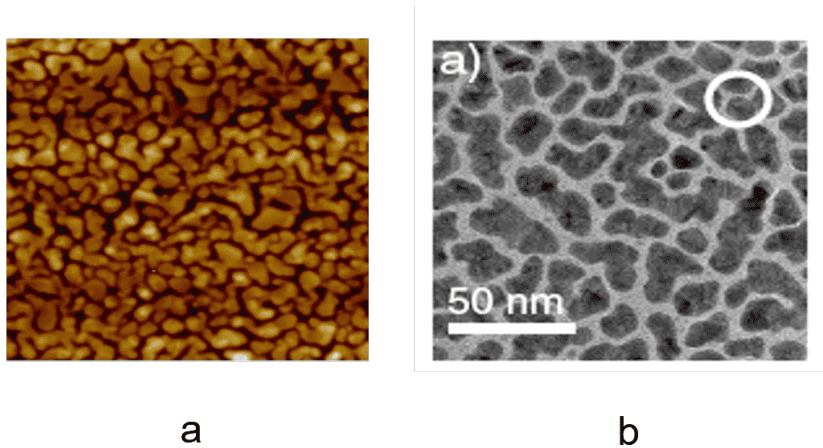


Figure 3.2: a) Atomic force microscopy image of a percolation gold film on quartz. [174] b) Transmission electron microscopy image of an Au film at the percolation threshold. [169]

Figure 3.2a shows a percolative gold layer which image was obtained by the Laverdant et coworkers through an atomic force microscopy [174]. This film has a filling factor of 59% and was obtained by a thermal evaporation in ultrahigh vacuum condition on quartz substrate. In Fig. 3.2b the Transmission Electron Microscopy (TEM) obtained by Carminati et al. for a percolative Au film on glass is reported [169]. These researchers demonstrated the fractal nature of this percolative gold film by analyzing the presence of non-linear optical transitions. Non-linear optics effects, strong electrical conductance, and super-diffusion phenomena generally occur above the percolation threshold. These are some typical phenomena usually observed in fractal systems, where novel and unexpected physical effects are observed [162,173].

The percolation threshold is directly correlated to a fractal geometry of the system. Since in literature is well known that by using a percolative gold layer deposition is possible to obtain a fractal Au film, the idea of our group was to use this fractal gold layer as a metal precursor to obtain a 2D random fractal array of Si NWs. With this approach, the fractal geometry of the gold is transferred to the Si NWs geometry obtaining a fractal Si NWs array. Indeed, as previously discussed, the gold in our approach is the negative mask to obtain Si NWs and so the gold fractal geometry is transferred to the Si NWs array. First of all, the Au deposition through an Electron Beam Evaporation (EBE) approach was optimized to obtain a percolative gold layer.

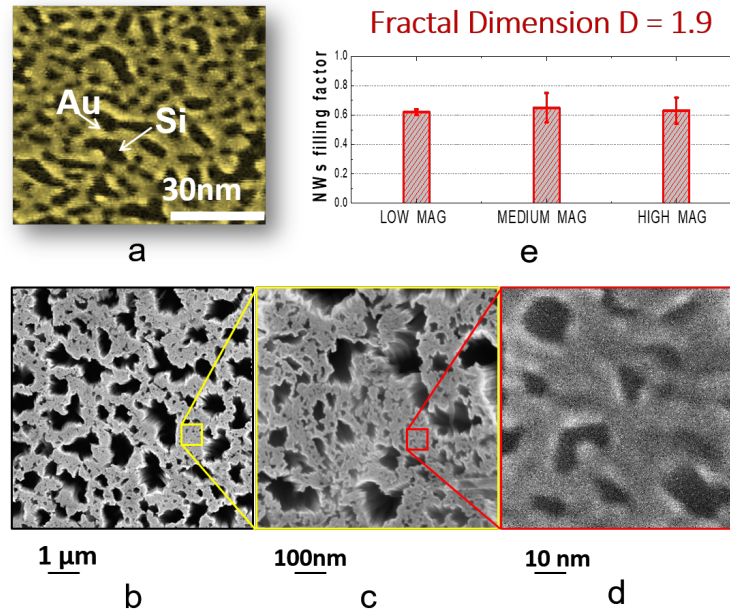


Figure 3.3: a) Au fractal film at percolation threshold obtained through electron beam evaporation on a Si substrate. Scanning electron microscopy (SEM) images of fractal Si NWs self-similarity are reported at 25 kX, 250 kX, and 2500 kX, in b), c), and d) respectively. e) filling factor comparison between the three different SEM magnification and obtained fractal dimensions through box-counting algorithm.

In Fig. 3.3a the plan view Scanning Electron Microscopy (SEM) image

of percolative gold layer obtained on an n-doped (ρ 1-5 ohm \times cm) Si bulk (111) substrate is reported. In this SEM image the Au is highlighted in gold and the black region is the uncovered Si region clearly showing the connected structure typical of the percolation threshold. A 54% filling factor was obtained for this film, above the typical Au percolation threshold on silicon and guaranteeing the realization of a fractal structure. The fractal geometry is sensitive to different factors such as deposition and substrate conditions. In particular, the substrate plays a crucial role in determining the wettability that permits a metal cluster arrangement onto the substrate surface [173]. After the optimization of the Au percolative gold deposition, a Metal-Assisted Chemical Approach (MACE) synthesis was used to obtain the fractal Si NWs array. This approach is explained in details in the first chapter. Our group have already demonstrated that Si NWs synthesized by this approach are a 2D random fractal. Indeed, in Fig. 3.3b-d are reported the SEM plan view obtained at a magnification of 25 kX, 250 kX, and 2500 kX, respectively. By these images is possible to appreciate the self-similarity behavior typical of a fractal object. It is very impressive to observe the repetition of the same random structure by changing the magnification up to 2 order of magnitude. The measured filling fraction was about 60% and remains the same for all the analyzed images (as reported in figure 3.3d). All the fractal properties of these Si NWs array have been already studied and demonstrated [21,140,175]. Moreover, the possibility to tune the fractal properties by changing the gold layer used as precursor are already been investigated with a broadband fractal geometry.

3.2.1 Fractal Si nanowires characteristics

In this section the characteristics of the fractal Si NWs array realized by my group are reported. Starting from these results, during my Ph.D. I have been involved in the experimental demonstration of the coherent Raman backscattering for the second stokes order with a complete study on the reciprocity breaking mechanism related to the sample characteristics. Moreover, an entire new activity on the realization and characterization of artificial 2D fractal array of erbium decorated Si NWs will be shown. The same Mandelbrot after the discoveries of the fractals in nature was the first to understand that the only fractal dimension was not enough to uniquely identify a fractal object. Indeed, for the same fractal dimensions, different objects can be found. An easy example used from this scientist come from the Cantor sets. This type

of mathematical fractal is built recursively starting from a segment, dividing it into n smaller segments, and by removing a certain number of them.

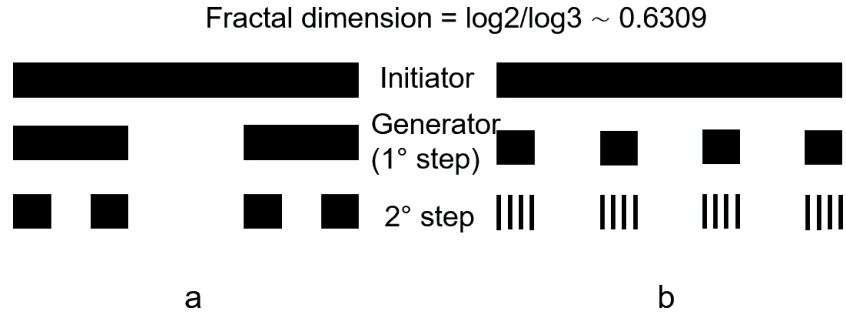


Figure 3.4: Two different Cantor sets with the same fractal dimension but with different lacunarity are reported in a) and b).

As an example, we can divide the segment into 3 part removing the central one (Fig. 3.4a). Iterating this simple rule a fractal Cantor set with fractal dimension ≈ 0.63 will be generated. Another Cantor set can be obtained by dividing the segment into 4 smaller segments of length $1/9$ of the previous one. Then these segments are equidistant disposed as visible in Fig. 3.4b. The generator of this second Cantor set is equivalent to uniformly spacing the elements obtained in the second step for the first Cantor set. Despite the two Cantor sets generated look slightly different, they have the same fractal dimension. The difference between them is the “degree” of rototranslational symmetry. Fractal dimension doesn’t uniquely identify a fractal and another parameter is required. Mandelbrot suggests that this parameter is the lacunarity able to quantify the heterogeneities present at each scale. In 1983 this scientist defined the distribution of gap sizes as a function of the length scale, the lacunarity. Therefore an object is considered more lacunar when the gap sizes are distributed over a wide range of lengths. In particular, the lacunarity is defined (up to an additive constant) as the variance divided the square mean of the mass measured for a certain box size. It is clear how this parameter may depend on the box size. Different calculation method and work [21, 39] report the lacunarity as:

$$\lambda_f = 1 + \frac{\sigma^2}{\mu^2} \quad (3.6)$$

Where σ and μ represent the standard deviation and the average filled pixels measured at a certain box dimension, respectively. This means that $\lambda_f = 1$ corresponds to the absence of lacunarity and hence, to the presence of rototranslational symmetry for the fractal. The presence of a high lacunarity means that at this particular scale a large fluctuation of the mass is present. This is the reason why a large lacunarity is an indication of a very heterogeneous material. A large fluctuation of the mass follows as a large fluctuation of the local refractive index of the material at a determined lengthscale, determining a strong coupling with light and a strong photon trapping at that corresponding wavelength. In particular, a fractal is characterized by a self-similarity at very different lengthscale and this permits to obtain a coupling with different wavelengths. All these points have driven our research through novel Si-based fractal able to foster a strong light trapping in a wide range of wavelengths. Indeed, light-harvesting and management are some of the most studied topics for a plethora of applications from photonics to photovoltaics. As discussed, our group previously demonstrated that the fractal Si NWs geometry is obtained through a percolative gold layer [21, 140, 175]. Hence, by changing the deposition condition or the type of substrate is possible to vary the fractal gold layer and so the Si NWs in-plane geometry. The design of different fractal can be optimized as a function of crystalline orientation of the substrate and of the deposition conditions by changing the filling factor and the geometry of the percolative gold layer. In particular, two different samples were realized by changing the substrate from (111) to (100)-oriented called sample 1 and sample 2, respectively. The different crystalline orientation determines a different electron density distribution and so, a different number of atom exposed onto the surface, thus causing a difference in the wettability of the two Si substrates [176, 177]. In particular, this changes the fractal arrangement of the gold layer and, as a consequence, of the Si NWs fractal array.

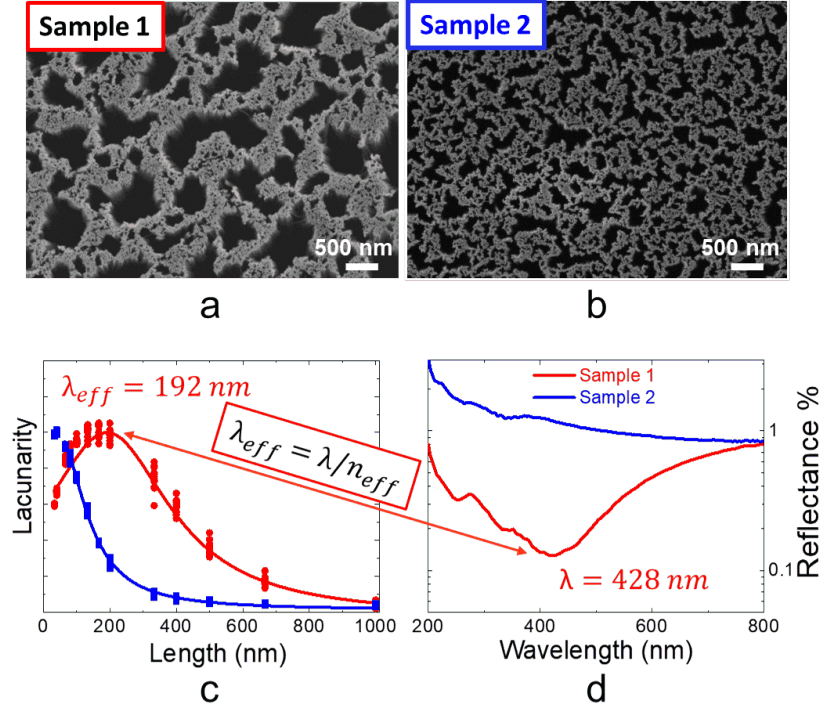


Figure 3.5: In-plane SEM images of sample 1 and sample 2 are reported at the same magnification in a) and b), respectively. The lacunarity of the two samples as function of the lengthscale are reported in c). d) Total reflectance percentage of both the sample in the UV-VIS-NIR range. [21]

In Fig. 3.5a and b) the sample 1 and 2 are shown, respectively. Sample 2 appears as a more compact and highly packed fractal architecture. The measured fractal dimensions were $D_{f1} = 1.87 \pm 0.02$ and $D_{f2} = 1.92 \pm 0.02$ for sample 1 and sample 2, respectively. The fractal dimension was obtained counting the number of the box at each box size ϵ , as discussed in the first part of this chapter. However, the fractal dimension itself is not enough to unequivocally describes the system. Both the fractal dimension and lacunarity are a measure of the structural complexity of the system. However, the lacunarity is the only quantity that describe the system heterogeneity distribution as a function of the length scale The lacunarity is defined as $\lambda_f = 1 + \sigma^2/\mu^2$ with σ and μ that represent the standard deviation and the average filled pixels measured at a certain box dimension, respectively. In Fig. 3.5c λ_f is reported as a function of the box size ϵ (observation scale) per

each sample. The pixel average number and its standard deviation were calculated with the same box counting approach through ImageJ. Both sample 1 and sample 2 show lacunarity values higher than one demonstrating the presence of heterogeneities in range of tens and hundreds of nanometers. The lacunarity of sample 2 increases for smaller length scale without showing any appreciable peak. The minimum length scale studied was 33 nm but it is not possible to exclude the presence of a peak for smaller length scale. In particular, the sample 1 shows a lacunarity peaked at 192 nm that correspond to the maximum fluctuation of air gaps between the Si NWs. This implies a strong fluctuation of the refractive index that correspond to an enhancement of the scattering efficiency of the material. Indeed, by measuring the light scattering properties is possible to observe the perfect correspondence of the total reflectance to the lacunarity of the system. The light scattering of the fractal Si NWs was studied by an integrating sphere for total and diffuse reflectance measurements. In particular, in Fig. 3.5d the total reflectance of the sample 1 and sample 2 in the UV-VIS-NIR range are reported in red and blue, respectively. As is possible to observe the reflectance of both the sample is lower than 1% demonstrating an efficient light trapping in all the visible range. The absorption and scattering properties of a single quantum confined Si NWs with a 7 nm diameter cannot explain such efficient light trapping inside the material [25]. The fractal structure with the presence of air gaps between the Si NWs, that span from few tens of nm to few microns, are responsible for the strong heterogeneity that leads this high in-plane multiple scattering inside the medium. In particular, the reflectance of sample 1 presents a minimum at 428 nm approaching the remarkable value of 0.1% while the sample 2 reflectance has a monotone trend. These results are in perfect agreement with the lacunarity trend of both the sample. Indeed, by considering the effective refractive index calculated through the Bruggemann mixing rule, the wavelength of 428 nm perfectly match the maximum of lacunarity at about 200 nm. Indeed, an effective wavelength propagating inside the material of $\lambda_{eff} = \lambda/n \approx 200$ nm is obtained with a refractive index $n = 2.33$ and a wavelength of 428 nm. The refractive index was obtained by considering a composition of 40% air voids, 40% silicon, and 20% silicon native oxide [178,179]. These value of the composition were obtained through previous SEM, TEM, and EDX analyses. Sample 2 lacunarity doesn't present any maximum and indeed, the reflectance measurements don't show any minimum. These measurements highlight the correspondence between the optical scattering properties and the lacunarity behavior. These results strongly

demonstrate the possibility of engineering the optical trapping of the Si NWs array by tuning the fractal and lacunarity characteristics with very interesting potentialities for photonics and photovoltaics. A strong light trapping in the UV-VIS-NIR range is very appealing for the light-harvesting and photovoltaics fields. Recently, novel black silicon material able to trap the light in the visible range were proposed in order to address this point [180]. Despite our Si NWs samples appear black, they cannot be enumerated inside the standard class of black silicon. Indeed, black silicon is characterized by a z-graded refractive index profile that leads to an antireflection effect. On the contrary, Si NWs obtained by MACE have an almost perfect vertical alignment leading to a constant refractive index along their vertical direction. The lack of a z-graded index profile permit to exclude an antireflection behavior for these Si NWs. However, in order to fully demonstrate the exclusion of an anti-reflection mechanism, transmittance measurements in the near-infrared were carried out. These measurements were performed using a spectrophotometer to detect the direct transmission signal excluding the diffused light components. In order to avoid any interference effect of the signal from rough Si surface, these measurements were performed on Si NWs synthesized on double-polished Si wafer and on its Si bulk reference.

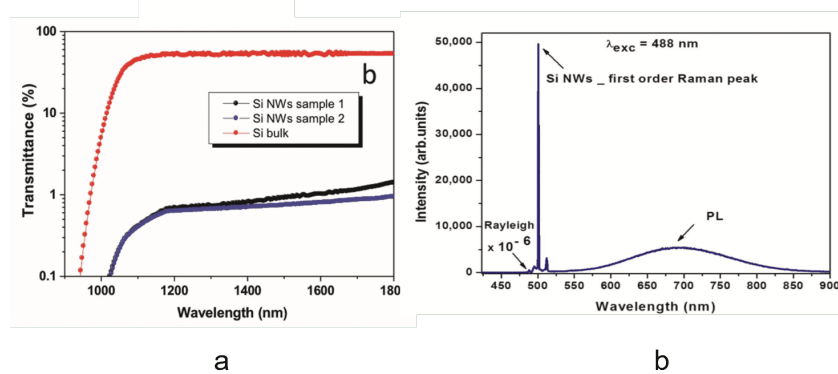


Figure 3.6: a) Transmittance percentage of the two Si NWs fractal realized in a double polished Si substrate compared to the double polished Si bulk reference in the Si transparency region from 900 to 1800 nm. b) Si NWs Raman scattering and PL emission obtained at room temperature exciting the system at 488 nm. [21]

In Fig. 3.6a, the transmittance obtained in the range 900-1800nm from

the Si bulk reference, sample 1, and sample 2 are reported in red, black, and blue, respectively. Comparing the Si NWs signal to the one obtained from the Si bulk reference a strong transmittance suppression below 1% is attested. The observed trend clearly permit to exclude an anti-reflection mechanism. Indeed, for anti-reflection materials, a transmittance increment above the Si bandgap is observed due to the fact that reflection and absorption of silicon are close to zero in the IR range after the Si bandgap. On the contrary, both the Si NWs samples present a transmittance lower than 1% in the Si non-absorbing region. Therefore, light is neither reflected nor scattered out of the Si NWs array but remains mostly trapped inside the NWs layer. This is a strong demonstration that the optical properties of the material and the strong light trapping are related to the fractal geometry of the Si NWs with the coupling of the light with the present air gaps, that span from tens of nm to few μm . The presence of such strong multiple scattering, able to foster light trapping in all the visible and NIR region, is extremely appealing for photonics and for photovoltaics applications. In the fractal Si NWs, the light trapping is not very affected by the radiation incident angle making this material a promising architecture for cost-effective, industrially compatible, and Si-based photovoltaics cells with high light trapping and efficiency all day. The light inside the fractal Si NWs medium results multiple scattered and eventually absorbed by the medium making the samples look black. Hence, the strong light trapping enhances all the process of scattering and absorption. The influence of the fractal on the Si NWs photoluminescence (PL) emission, as well as on the Raman scattering of the medium, was investigated. The Si NWs array (sample 1) was excited with the 488 nm line of an Ar^+ laser with a power of 20 mW onto the sample plane. In Fig. 3.6b the PL emission and the Stokes first and second order Raman of sample 1 are reported. The broadband NWs PL signal centered at about 700 nm and due to the quantum confinement effected is clearly visible in the figure. However, It is impressive to observe such remarkable high Si Raman signal compared to the bright NWs PL emission. The realization of 2D Si NWs fractal arrays has been demonstrated by maskless, cost-effective, and Si-technology compatible approach. By using this approach is possible to engineer the fractal geometry in order to tune the optical properties in term of scattering. Fractal Si NWs arrays with strong light trapping in all the visible and NIR range were shown, underlining their promising low reflectance performances for photovoltaics and remarkable Raman and PL signal for novel photonics applications.

3.3 Coherent backscattering of Raman light

Among the interference effects occurring when light propagates in a random medium, the most robust and always surviving any averaging upon disorder, is known as Coherent Backscattering (CBS) of light. This phenomenon is described as a simple constructive interference process of a couple of electromagnetic waves, which preserve their phases and interact after reciprocal paths. In analogy with the weak localization of electrons in solid-state [181], CBS is also known as weak localization of light and it is considered a precursor of strong localization regime. The interaction between the two light paths always leads to a factor of 2 coherently enhanced intensity at the exact backscattering direction with respect to the diffuse incoherent background; the exponential decay of the intensity as moving away from the backscattering gives rise to an intensity angular feature known as CBS cone. The reciprocal light paths interference is analogous to the case of a Young double-slit interferometer with the last scatterers that play the role of the two slits. Thus, from a quantum point of view, CBS is just a single photon self-interference effect due to the indistinguishability of the two paths and hence to the reciprocity of the process. In this view it appears clear as any perturbation to the two mutual light paths indistinguishability determines a reciprocity breakdown with the consequent lowering and eventually loss of the CBS cone [182]. Different processes can break the indistinguishability of the two paths causing a dephasing between the two reciprocal waves such as scatterers motion, as in the case of Brownian motion [181], or, in the case of ultracold atoms, by applying a dephasing kick on atoms by means of an optical disordered potential [183]. Furthermore, by using an external magnetic field is possible to obtain different final polarization state for the two counter-propagating waves breaking the reciprocity between the two light path [184]. As already shown in the previous section, our Si NWs material is affected by a strong multiple scattering of light resonant with the fractal structure. The strong scattering strength has been determined by means of Rayleigh CBS measurements that highlight a large cone from which we deduced a transport mean free path of 170 nm when the system is excited at 532 nm. Moreover, thanks to an intriguing combination of strong scattering and not negligible absorption of light, Si NW array permitted the first observation of coherent backscattering of Raman light (RCBS) [140,185]. The recent demonstration of RCBS arising in spontaneous Raman scattering of light proposes another all-optical mechanism able to break the indistinguishability of the reverse

light paths. More interesting, in the Raman case, the indistinguishability is obtained without any type of external perturbation since it is related only to the way the light propagates across the medium, which in turn, it depends on the material properties. In solid-state physics Raman scattering can be described as an inelastic process for which a photon loses or gain an amount of energy equal to that of vibration quantum (phonon) of the matter with which it interacts. For a time interval on the order of few picoseconds, the Raman photon preserves coherence with the incident photon, thus in principle allowing for the observation of Raman coherent backscattering. The RCBS phenomenon takes place as the interference of Raman photons generated in reciprocal light paths. Since the position of each Raman scatterer is arbitrary during the random walk of light across the medium, reciprocal paths traveled at different wavelength can develop a dephasing, which affects the shape and the intensity of the cone. In the Raman case, the short scattering mean free path determines the number of scattering events for which the coherence of Raman photon is preserved. On the other hand, the optical absorption cuts the longest paths preventing a dephasing between reciprocal paths. These occurrences make the RCBS cone of Si NWs well visible not only for the first order Stokes and anti-Stokes, but also for the Stokes second order Raman mode of silicon. Hence, Si NWs appears as the perfect candidate to a detailed study of the RCBS phenomenon and to an in-depth analysis of the dephasing mechanism effect. Raman Stokes second order is characterized by a larger frequency shift if compared with the first order mode, and as predicted by the hybrid scattering path theoretical model, leads to a partial reciprocity breaking. In this thesis work we experimentally demonstrated as the Raman mode frequency strongly affects the light dephasing mechanism in the two reciprocal paths, leading to a breaking of reciprocity for certain light paths. In order to represent the physics of the coherent backscattering of Raman light a hybrid path model with Rayleigh and Raman events was designed.

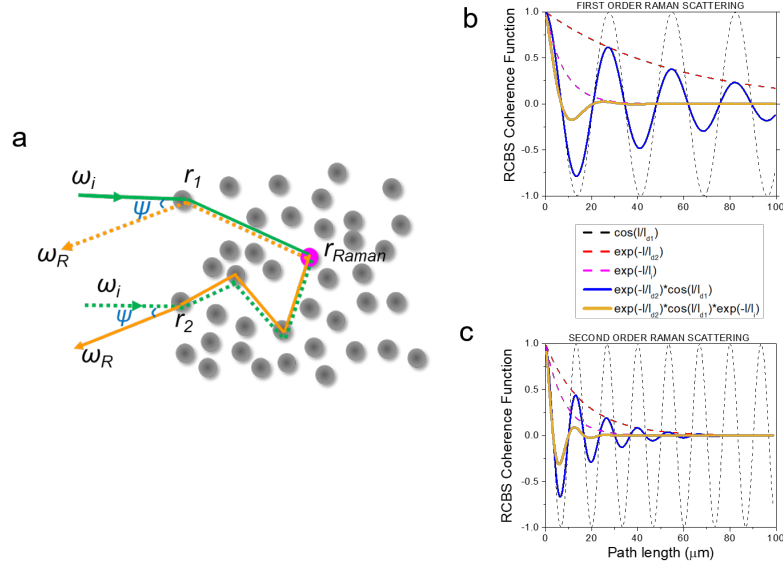


Figure 3.7: a) Schematic illustration of the hybrid path with Rayleigh and Raman events for two counterpropagating beams. In b) and c) the phase factor and cut-off length that determines the global phase factor for coherent Raman scattering are reported for first and second order, respectively.

As shown in Figure 3.7a, a photon propagates inside the scattering medium with a certain number of elastic scattering events. At a certain point a Raman scattering happens and, due to the phonon interaction, the photon propagating after this event is characterized by a slightly different wavelength. On the reciprocal path the inverted case happens. Reasoning in terms of waves, light waves go through reciprocal paths with steps between scatterers at different wavelengths where we have the presence of a Rayleigh scattered wave in one direction this correspond to a Raman one in the reciprocal path and viceversa (see Fig. 3.7a). In the Rayleigh case, the phase difference between the two waves is determined by the difference of the two geometrical path. On the contrary in the RCBS case, due to the wavelength change introduced by the Raman event, the two reciprocal waves accumulate a phase shift by a difference in the optical path at each scattering step. As a consequence, the two out-coming waves can accumulate a global phase difference $\Delta\phi$; a constructive interference allowing to detect a Raman coherent backscattering is possible only if the global dephasing appreciably remains below π . We should notice that the Raman event can happen in any scatterers along the path with

the same probability. As a consequence of that, a statistical distribution of $\Delta\phi$ related to the position of the Raman event along the light path has to be considered. From this distribution it is possible to obtain the global average phase factor, which is found to be a complex function. Let's consider a photon that is traveling from one point \mathbf{r}_1 to another \mathbf{r}_2 by multiple scattering processes, the probability that it preserves phase coherence in this trajectory, and in the time-reversal one, is named Cooperon. Cooperon is mathematically defined as $\langle C(\mathbf{r}_1, \mathbf{r}_2, \mathbf{r}_3, \mathbf{r}_4) \rangle = F(\mathbf{r}_1, \mathbf{r}_2)\delta(\mathbf{r}_1 - \mathbf{r}_4)\delta(\mathbf{r}_2 - \mathbf{r}_3)$. In the general case, the Cooperon describes the coherent backscattering phenomenon through the intensity propagator $F(\mathbf{r}_1, \mathbf{r}_1)$ related to the dressed Green function [186]. In the Raman case C is affected by the global phase factor that assumes the following form [140] $\langle e^{i\Delta\phi(l)} \rangle \cong e^{il/l_{d1}} e^{-l/l_{d2}}$. In the global phase factor the two dephasing lengths, $l_{d1} = 2/|\Delta k|$ and $l_{d2} = 2/(l_t \Delta k^2) = l_{d1}^2/2l_t$, are introduced. In these quantities, Δk is the module of the wavevector exchanged in the Raman process at r_{raman} . In Fig. 3.7 these factors are reported for the first order and the second order in b) and c), respectively. In particular, l_{d1} goes inside the cosine acting as a fast oscillating term (black dashed line) and represents a phase matching length. Depending on the relative phase difference of reciprocal paths it allows for constructive and destructive interference. On the other hand, l_{d2} , much longer than l_{d1} for $l_{d1} \gg l_t$, acts as a cut-off length with an exponential decay factor (red dashed line). The random position of the Raman scatterer determines a fluctuation of the dephasing between the two reciprocal paths. This Raman coherence loss is represented by l_{d2} . Another cut-off length that acts on this process is l_i that represents the inelastic scattering mean free path related to the photon losses by absorption (pink dashed line). The mutual effect of l_{d1} and l_{d2} is reported as a blue line. The final form for the global average phase factor is therefore a damped cosine (orange line) and it is clearly visible the difference of this function between first and second order. Then, if we consider an incoming plane wave perpendicular to the sample surface and damped inside the medium by K_{ext} (extinction rate), the final form for the coherent backscattered intensity in terms of scattered flux per solid angle $\gamma_c(\mathbf{k}_s)$, with \mathbf{k}_s outgoing vector, is the following:

$$\gamma_c(\mathbf{k}_s) \propto \int d\mathbf{r}_1 \dots d\mathbf{r}_4 e^{i\mathbf{k}_s(\mathbf{r}_1 - \mathbf{r}_3)} e^{-1/2K_{ext}\mu_s^{-1}(z_1 + z_3)} \\ \times F(\mathbf{r}_1, \mathbf{r}_2)\delta(\mathbf{r}_1 - \mathbf{r}_4)\delta(\mathbf{r}_2 - \mathbf{r}_3) e^{i\mathbf{k}(z_2 - z_4)} e^{-1/2K_{ext}(z_2 + z_4)} \quad (3.7)$$

$\mathbf{k} = \omega/c_0$ with c_0 the speed of light in the vacuum. The extinction rate K_{ext} is

now modified by the presence of both the dephasing lengths and assumes the form $K_{ext} = l_t^{-1} + l_i^{-1} + i l_{d1}^{-1} + l_{d2}^{-1}$ (see [140] for more details). Here l_i represents the inelastic or absorption mean free path, linked to the absorption length L_{abs} by the relation $L_{abs} = \sqrt{(l_i l_t)/3}$. The absorption plays a fundamental role in RCBS cone preventing the vanishing of Cooperon intensity when the inelastic scattering length l_i is shorter than l_{d2} . It is worthy to note that l_i acts as a cut off for both coherent and incoherent longest paths. After the demonstration of the presence of this phenomenon, in order to show the role of the dephasing length on the RCBS cone, a set of simulations were carried out by using the hybrid path model for the second order Raman mode of Si. The effect of absorption is newly remarked in Figure 3.8a. The RCBS simulated cone, calculated at a fixed transport mean free path, is plotted as a function of the inelastic scattering length. Decreasing the material absorption and therefore increasing l_i , a relative minimum appears in the Raman cone at the backscattering angle ($\psi=0$), for which the longest scattering paths contribution is accounted. In Figure 3.8b the RCBS angular shape trend as a function of the transport mean free path l_t is shown with l_i fixed at $8.1 \mu\text{m}$. The inelastic scattering length used is the one previous calculated for a light propagating at 532 nm of wavelength in the Si NWs medium [140]. Since $l_{d2} = (l_{d1}^2)/2l_t$, a change of l_t affects the l_{d2} value for a fixed l_{d1} . Therefore, also in this case, we deal with the variation of a cut off length in the traveled coherent paths. When l_t increases, the dephasing length l_{d2} decreases and then the Cooperon intensity is damped, involving the longest paths mostly, for which it goes rapidly to zero.

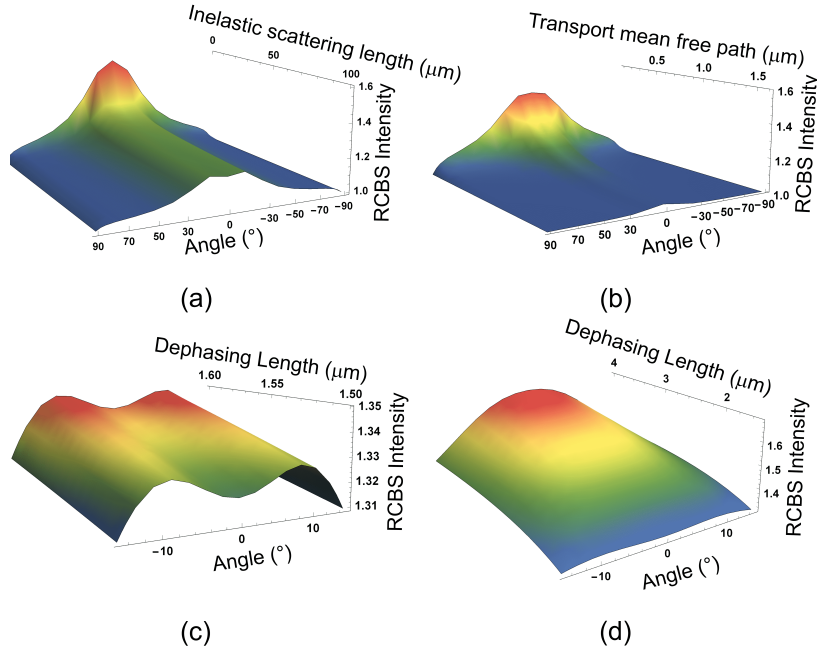


Figure 3.8: a) RCBS cone at fixed transport mean free path is plotted as a function of the inelastic scattering length. b) RCBS cone with fixed inelastic scattering length is reported as a function of the transport mean free path. RCBS angular shape as a function of the dephasing length l_{d1} in the Raman second order c) and in the first order d) value range.

The dephasing length l_{d1} is related to the module of the exchanged wave-vector Δk and so it changes between different Raman modes. Figures 3.8c and d) put in evidence the role played by l_{d1} on the shape of RCBS cone in two different ranges of dephasing length, from the second order value range (Fig. 3.8c) to the first order Raman mode of silicon (Fig. 3.8d). We notice that the longer l_{d1} , the more the Raman frequency approaches the Rayleigh one. We notice that the l_{d1} increasing for the first order case with respect to the second order one, corresponds to a longer period associated to the oscillating term of the global dephasing (as shown in Fig. 3.7c-d). On the other hand, l_{d1} and l_{d2} are linked together. Indeed, $l_{d2} = l_{d1}^2/2l_t$. As a consequence, a change of the phase matching length l_{d1} affects the cut-off term of global phase factor. Destructive interference contributions are taken into account by the fast oscillating cosine that enters into the real part of the global phase factor (black dashed line in Fig. 3.7b). These destructive interference path

can appreciably weight averaging on all reciprocal paths lengths. Indeed, a partial anti-enhancement effect for those particular path lengths accumulating relative phase difference of $(2n + 1)\pi/2$ occurs, making significantly lower the enhancement factor. In order to demonstrate this dephasing mechanism, a Raman scattering experiment on 2D fractal Si NWs was carried out. Raman coherent backscattering measurements were performed in the range -90° , 90° by using a homemade goniometer. A 532 nm solid-state laser was used to excite the sample with a spot size of 1 mm of diameter onto the Si NWs surface. In order to eliminate as much as possible laser speckles and average on all the scattering paths, the sample was put on a rotating mount and all the data were obtained in this configuration. The light signal was acquired with a 0.1° of angular resolution by a nitrogen-cooled CCD (Spec 400 BR, Princeton Instruments). The incoherent contribution was measured acquiring the linear polarization non-conserving channels. The signal was obtained in linear cross-polarized configuration taking into account the vertically polarized incident laser beam. In order to collect the coherent part of the scattering intensity, the measures were performed acquiring the helicity-conserving channel. In this configuration, single scattering events and reflections from the set-up are excluded. The coherent contribution was then normalized to the tails at larger angles than 60° of the incoherent contribution. The normalized backscattering cones were obtained by dividing the intensities of the helicity-conserving channel for the measured diffuse background. In order to verify the particular shapes of RCBS predicted by the dephasing model, we experimentally investigated the angular dependence of the scattered light related to all the Raman modes of silicon.

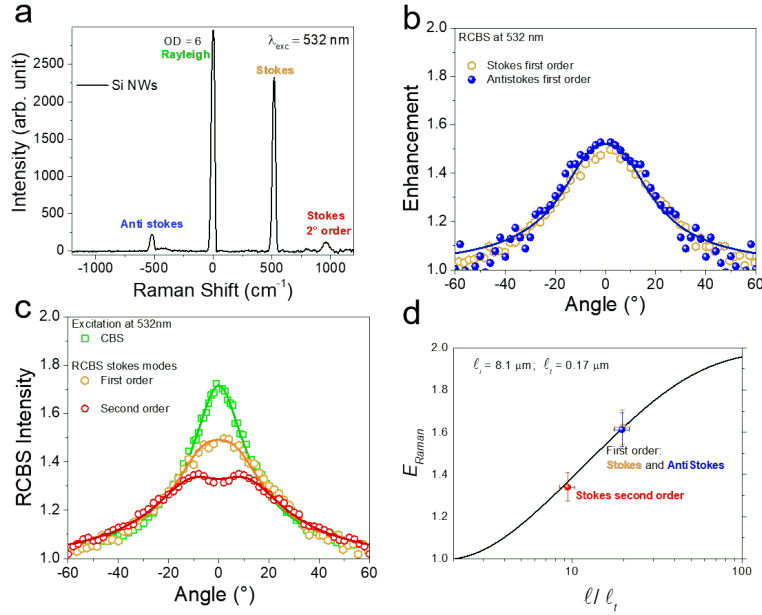


Figure 3.9: a) Typical Raman scattering acquisition obtained for 20° . b) RCBS cone comparison between Stokes and Anti-Stokes first order. c) RCBS cone comparison between Rayleigh (green) and Raman Stokes first (orange) and second order (red). d) Enhancement Raman obtained for the different orders in backscattering condition as a function of the dephasing length l_{d1} normalized to the transport mean free path.

All the spectroscopic signals coming from Rayleigh, anti-Stokes, and Stokes first and second order Raman scattering were acquired in a single spectrum for each angle, as shown in Figure 3.9a for a scattering angle = 20° . This procedure guaranteed to have identical experimental conditions for the entire data set. Raman anti-Stokes modes are characterized by the same absolute frequency shift of the Raman Stokes modes of the same order, even if the two scattering processes are generated by different energy transfer mechanisms, energy acquisition (anti-Stokes) or loss (Stokes). Since they are related to the same exchanged wave-vector module ΔK , the RCBS processes should be affected by the same dephasing length l_{d1} . Indeed, as shown in Fig. 3.9b the RCBS cone obtained for the anti-Stokes mode (blue dots) of the first order Si Raman peak shows exactly the same shape of that one of the RCBS cone related to the Stokes first order Raman (orange dots). Furthermore, by

the RCBS cone fit (orange line) we obtained similar values of both dephasing length l_{d1} and Raman enhancement E_{Raman} (see Table 3.1).

Raman scattering mode	E_{Raman}	$l_{d1}(\mu\text{m})$	$l_{d2}=l_{d1}^2/2l_t(\mu\text{m})$
Anti-Stokes first order	1.61 ± 0.08	3.4 ± 0.3	34 ± 7
Stokes first order	1.62 ± 0.08	3.4 ± 0.3	34 ± 7
Stokes second order	1.38 ± 0.06	1.7 ± 0.4	9 ± 2

Table 3.1: Enhancement Raman and dephasing lengths obtained for the different Raman modes.

On the contrary, comparing different order Raman scattering that are characterized by different wavelength shift is possible to observe a drastic cones shape change. In Figure 3.9c the Rayleigh case (green) is compared to the first (orange) and the second order Raman Stokes (red). In the figure, all the data are reported as dots and the lines of the same color correspond to the RCBS cone fit obtained. The shape change is due to the variation of dephasing length measured by the fitting procedure and the obtained data are in agreement with the theoretical ones. In particular, the RCBS cone of Stokes second order Si peak shows the presence of a sort of plateau at small scattering angle ($\pm 8^\circ$) with a relative minimum at about 0° . A perfect agreement of the experimental data with the fitting curve at small angles was found. This is a strong demonstration that our theoretical model, based on dephasing mechanism between reciprocal paths, takes into account the possibility of this particular cone shape. Indeed, the absolute value of the scattering angles is strictly related to the light path length that can participate in the coherent interference. The smaller the angles absolute value the longer the allowed scattering path. The appearance of a plateau in the angular dependence of coherently scattered light, with a relative minimum at 0° , is due to reciprocity breaking which mainly affects the longer interfering paths and that is part of the Raman coherent backscattering physics. In Figure 3.9d the E_{Raman} obtained for all the measured scattering signals are reported as a function of scattering path total length normalized to the mean free path l/l_t . Decreasing the mean free path, this figure highlights the similarity of Raman Stokes and anti-Stokes first order and the difference with the Stokes second order. In conclusion, thanks to the particular optical prop-

erties based on a fascinating mixture of scattering and absorption exhibited by Si NWs random fractals, we were able to thoroughly investigate the new physics of Raman Coherent backscattering. RCBS appears as an all-optical process able to break reciprocity without the action of any external field and is uniquely linked to the scattering medium properties. Indeed, reciprocity breaking depends on characteristic lengths of the random medium, such as the transport mean free path and the inelastic scattering length. This evidence paves the way for coherent control of waves in disordered materials just tuning their morphological and compositional characteristics, with important implications in future sensing technologies.

3.4 Fractal arrays of erbium doped yttrium oxide decorated silicon nanowires

The strong light-trapping demonstrated in 2D artificial random fractal Si NWs driven our research through new methods to integrate silicon and other interesting material in controllable engineering of the fractal process. In this scenario, the integration of different light-emitting material in Si represents a critical demand for silicon photonics. Among all the possible strategy to obtain light emission in silicon, a very studied approach is the introduction of light-emitting impurities. In this field, rare-earth ions and in particular erbium has a special role as one of the most studied and interesting systems. Another great advantage of this material is that erbium can be introduced as a dopant in Si compatible substrate by standard silicon technology processes. However, Er is characterized by low solubility and low excitation cross-section. In order to overcome these drawbacks, several strategies were employed in these years [22]. Silicon nanoclusters were used as Er^{3+} -sensitizers demonstrating an enhancement of four orders of magnitude for the excitation cross-section [187] and with the possibility to obtain an efficient excitation by non-resonant transfer [188]. The low solubility of erbium in silicon is a critical limit to the light-emitting performance of the device. Indeed, the occurrence of clustering phenomena and non-radiative ion-ion interactions can strongly affect the light emission of the platform. Another limit, arising for high Er concentration, is the ion-ion interactions which determine the occurrence of new non-radiative phenomena with the consequence of a PL quenching. The critical doping concentration depends on the

matrix and indeed, the scientific community has devoted a lot of efforts on the research of Si compatible materials that allow the incorporation of high concentrations of optically active erbium ions [189,190]. Erbium silicates emerged as a very interesting solution due to their crystalline structure. In these materials, erbium is not a dopant but a constituent [191,192]. Among them, yttrium oxide (Y_2O_3) is a Si compatible material [193] that arise as a strategic solution to minimize the ion-ion interactions [194,195] that may suppress the Er light emission. In this material, the crystalline structure of the Er_2O_3 is very similar to the Y_2O_3 one and the Er atoms can be introduced in the Y substitutional position. Due to this reason, concentrations up to 10^{22} at/cm³ without Er clustering were demonstrated [196]. In this scenario, the realization of artificial $\text{Er}:\text{Y}_2\text{O}_3$ decorated Si NWs fractals appear as very promising for the realization of a new light-emitting Si compatible materials. In order to decorate the Si NWs fractal in an engineerable way without losing the self-similarity behavior of the fractal, a novel decoration approach was optimized by using a sputtering glancing angle deposition.

3.4.1 Glancing angle sputtering decoration

The first crucial challenge was to find an innovative industrially compatible and non-destructive approach able to deeply and uniformly decorate the Si NWs with the Er-silicate materials. Vertically aligned Si NWs with 2D fractal geometry were synthesized by metal-assisted chemical etching using a 2 nm percolative gold layer on a (111) n-type (ρ 1-5 ohm \times cm) Si substrate as discussed previously. The deposition of Er-doped Y_2O_3 on the 2.5 μm length Si NWs was obtained by a glancing angle deposition performed at different angles.

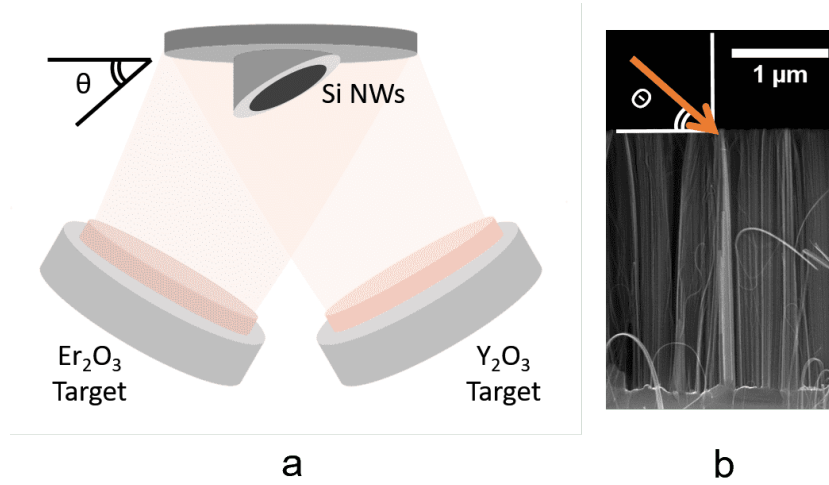


Figure 3.10: a) Scheme of the glancing angle sputtering deposition approach for the case of $\text{Er}:\text{Y}_2\text{O}_3$ decorated Si NWs. b) Cross section of Si NWs showing the angle deposition respect to the sample.

A schematic illustration of this process is shown in Fig. 3.10a. The deposition angle θ is the angle of the sample holder with respect to the standard parallel position to the targets. In Fig. 3.10b the as-synthesised Si NWs cross-section SEM image with the angle of the deposition θ is shown. The use of a glancing angle co-deposition guarantees that the presence of the fractal geometry is not only preserved but can be controlled by changing the deposition angle. A target of Y_2O_3 and another one of Er_2O_3 were co-sputtered at the same time in an ultra-high vacuum chamber of a magnetron sputtering. The Y_2O_3 and Er_2O_3 targets were eroded by radiofrequency co-sputtering in a controlled Ar atmosphere at a pressure of 5×10^{-3} mbar and deposited onto Si NWs and c-Si(111) reference substrates placed onto the uppermost part of a tilted homemade holder at a constant temperature of 300°C . In order to guarantee the uniformity of the decoration in any part of the NWs, the sample holder rotate at ≈ 10 rpm. A constant power of 35W and 500W were applied to Er_2O_3 and Y_2O_3 target, respectively, in all the processes. In this way, the amount of yttrium and erbium oxide were maintained fixed between the different Si NWs samples and Si bulk references. The stoichiometry $\text{Er}:\text{Y}_2\text{O}_3$ is determined by the sputtering of yttrium and Er oxide without using other oxygen sources. These conditions were chosen by the optimization of the deposition process obtained in previous work for

high-quality Er-rich and optically active Y_2O_3 -Si substrate [196]. In order to increase the decoration depth along the Si NWs without ruining the fractal morphology, a glancing angle deposition was used. Indeed, the self-shadowing effect permits to vary the morphology of the deposited material as a function of the deposition angle. The Si NWs and the Si bulk were co-sputtered at three different angles, 5° , 10° , and 15° , in order to demonstrate the realization of a decoration process able to vary the fractal morphology without losing the scale-invariance effect. Increasing the angle, a more uniform coverage with a more in deep deposition is obtained. The same conditions were used for Si NWs and Si bulk substrate reference. The morphological and optical properties are influenced by the oblique angle chosen for the Si NWs samples onto the tilted holder.

3.4.2 Structural and optical characterization

In order to confirm the stoichiometry of the elemental composition of the $\text{Er:Y}_2\text{O}_3$ decorated sample, an RBS analysis was carried out. In this characterization technique, an ion beam (He^+ in our case) at an energy of 2 MeV onto the samples is used as a probe in a Rutherford backscattering experiment. By the energy loss of the probe is possible to obtain the atomic density of the probed element and the thickness of a thin film. In our set-up, the He^+ ions are accelerated by a singletron HVEE and the backscattered electrons were collected and analyzed by a multichannel analyzer at the detection angle of 165° with respect to the beam direction. Fractal Si NWs are characterized by air gaps that span from nm to μm range. For the $\text{Er:Y}_2\text{O}_3$ covered Si NWs the range of the air gap is slightly reduced especially for the small holes but it is still present. In RBS analysis is extremely complicated to fit a signal from such discontinuous material as shown in Fig. 3.11a in green for bare Si NWs. In the Si NWs samples, the signal from the Si is strongly influenced by the discontinuity of the substrate. Indeed, an He^+ ion can be backscattered from the NWs tips as well as from the Si substrate at $2.3 \mu\text{m}$ of difference. This introduces a strong variation on the Si atom position reflected by the RBS spectrum shape. Thus, the analysis was performed on Si bulk to find the stoichiometry of the deposited material. The RBS spectra obtained for 5° , 10° and 15° $\text{Er:Y}_2\text{O}_3$ depositions on Si bulk shown the same stoichiometry, as expected by the deposition conditions.

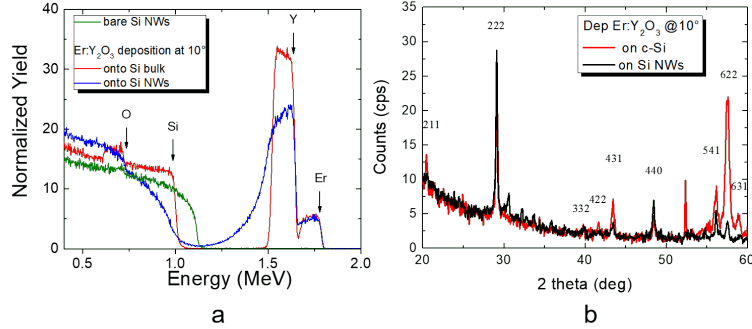


Figure 3.11: a) Rutherford backscattering spectrometry of the bare Si NWs (green) and of the decorated Si bulk (red) and Si NWs (blue) obtained at 10° . b) X-ray diffraction analysis of the $\text{Er:Y}_2\text{O}_3$ deposited on Si bulk and on Si NWs at 10° .

In Fig. 3.11a the typical signal obtained from $\text{Er:Y}_2\text{O}_3$ on Si bulk is shown in red (10° case). The presence of the Er, Y, Si, and O signals are highlighted in the graph. By fitting the position of these peaks and their extension with the simulation software SIMNRA we found an Er concentration of 2 ± 1 at% (areal density of about 0.3×10^{17} at/cm²), while Y and O shown a concentration of about 38 ± 2 at% (areal density of 4.5×10^{17} at/cm²) and 60 ± 5 at% (areal density of 7×10^{17} at/cm²), respectively. For the $\text{Er:Y}_2\text{O}_3$ decorated samples (blue spectrum), the Si signal shows a clear shift towards lower energy loss channels, which is the results of the additional energy loss of the ion probe that is proportional to the $\text{Er:Y}_2\text{O}_3$ concentration onto the surface. It is worth noticing that after the $\text{Er:Y}_2\text{O}_3$ decoration, both the decorated Si bulk and Si NWs attest about the same downshift, further suggesting the same concentration of Er, Y and O deposited on the two substrates. This point is strongly confirmed by the same Er and Y areal density in the two samples. After the RBS analysis, the Si NWs and Si bulk decorated samples were characterized by XRD with a Bruker X-ray diffractometer to demonstrate the absence of Er silicates between $\text{Er:Y}_2\text{O}_3$ and Si NWs. Indeed, Er silicates layers at the interfaces are well known to strongly affect the PL emission, acting as non-radiative de-excitation channels. In Fig. 3.11b the XRD spectra of the Si bulk and Si NWs decorated at 10° are reported as an example, confirming the good crystalline quality of the $\text{Er:Y}_2\text{O}_3$ films. The fingerprint of the cubic Y_2O_3 crystalline structures is visible for the two sam-

ples, confirming the absence of silicates whose characteristic X-ray diffraction peaks are not visible. This result is in agreement with the literature where the formation of Er silicate at the interface between $\text{Er:Y}_2\text{O}_3$ and Si NWs are absent at a deposition substrate temperature of 300°C [196]. After the XRD characterization, the $\text{Er:Y}_2\text{O}_3$ decorated Si NWs were analyzed in plan view and in cross-section by SEM per each tilt angle.

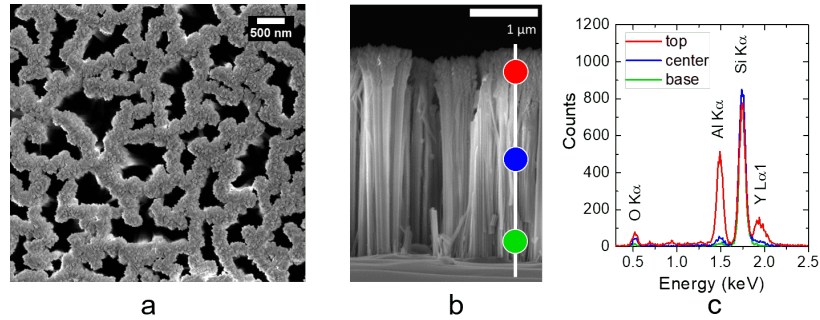


Figure 3.12: SEM images of $\text{Er:Y}_2\text{O}_3$ decorated Si NWs in plan view and in cross section are showed in a) and b), respectively. c) Energy dispersive X-ray analysis of the 10° decorated Si NWs reported for the bottom (green), center (blue), and top (red) region.

In Fig. 3.12a the plan view of the 10° decorated Si NWs sample is reported. As is possible to observe, the decoration process follows the Si NWs geometry in-plane without closing all the present air gap. This point is crucial to preserve and engineer the fractal morphology of the system. In Fig. 3.12b the cross-section of the 10° sample is reported as a representative of the ensemble. In this image is possible to observe a polycrystalline Y_2O_3 structure decorating the uppermost part of the NWs tips with a decoration that goes up to $1.5\ \mu\text{m}$ deep while the yttrium oxide presence is no longer attested in the bottom part of the Si NWs. In all the SEM images the Si NWs do not result damaged by the decoration process. In the $\text{Er:Y}_2\text{O}_3$ decorated Si bulk sample the deposited film is continuous with the same stoichiometry, but to a tilt angle increasing correspond a decreasing film density. These characteristics are typical of an angle sputtering process. The $\text{Er:Y}_2\text{O}_3$ profile along the Si NWs was further analyzed by high magnification SEM and by an EDX profilometry analysis. In Fig. 3.12c the EDX spectra obtained in the top, center, and bottom part of the $\text{Er:Y}_2\text{O}_3$ decorated Si NWs at 10°

are reported in red, blue, and green, respectively. In the three zone marked with the correspondent colored circle the Si, Y, and O X-ray signals were detected. The Er concentration in these samples of 2% is too low to permits the acquisition of the typical X-ray signal of this element by EDX. Going from the Si NWs tips to the bottom part, the Y L_α signal (around 1.9 keV) decrease to the 16% in the center region (blue circle) and to the 4% in the bottom region (green circle) considering as 100% the signal detected onto the tips (red circle). A similar trend is attested for the O concentration. Indeed, the K_α emission line of O at 0.5 keV decrease to 54% in the center and to the 20% on the bottom with respect to the tip value corresponding to the 100%. On the contrary, as attested by K_α emission line at 1.75 keV the Si experiences a 5% decrease in the top region due to the major presence of Y_2O_3 . The difference between the Y and O reduction can be explained by considering that the oxygen percentage is also affected by the native oxide shell of the Si NWs. This EDX profile trend is very similar for all the other samples with the only difference of a deeper deposition for higher angles. Even if with EDX a precise Si NWs covered length cannot be obtained, it is possible to obtain an estimation of a 10% depth decrease for each 5° the tilt angle decreasing from 15° . In particular, the deposition depth goes down to $1.5 \mu\text{m}$, $1.25 \mu\text{m}$, and $1.10 \mu\text{m}$ for 5° , 10° , and 5° respectively. The fractal morphology of the samples obtained at different angle depositions were studied by using the FracLac plugin of ImageJ software. Different SEM images were acquired in plan-view at 5 kX, 50 kX and 300 kX magnifications for each sample. The acquired images were converted in binary by using the same contrast threshold level. This step is required by FracLac sliding box-counting algorithm that works on binary images. Moreover, the same set of box sizes, that is used by FracLac to probe the scale invariance by a box-counting algorithm, was applied to all the samples. All these steps were designed to guarantee consistency between the results. The fractal and the lacunarity analyses were performed on the 50 kX magnification images that permit to study a broad range of lengthscale from 20 nm up to $2 \mu\text{m}$. However, the first and the last part of the obtained trends were confirmed by further performing this analysis on the other magnification images per each deposition angle.

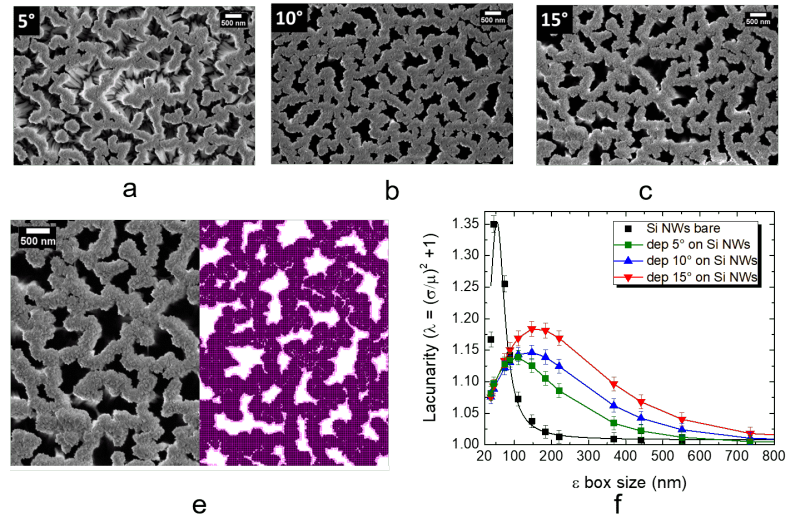


Figure 3.13: Plan view Sem images for 5°, 10°, and 15° $\text{Er:Y}_2\text{O}_3$ decorated Si NWs at the same magnification are reported in a), b), and c), respectively. In e) an example of superimposed boxes for the box-counting algorithm on the 15° decorated Si NWs sample is shown. f) Lacunarity as a function of the lengthscale (box size) for the bare Si NWs sample (black), 5° (green), 10° (blue), and 15° (red) decorated Si NWs.

The SEM plan-view images of the $\text{Er:Y}_2\text{O}_3$ decorated Si NWs obtained at 50 kX for 5°, 10°, and 15° are reported in Fig. 3.13a-c, respectively. It is clearly visible how the random fractal arrangement is preserved after the decoration process but with a different scale for each tilt angle. Indeed, the interstices among Si NWs appear to be more covered for small angles with a clear variation of the fill factor. The fill factor or the filling fraction (FF) is the ratio of the covered area per the total area of the analyzed image that we measure by pixel counting with ImageJ. A FF of $42\% \pm 2$ was measured for the bare Si NWs sample. The $\text{Er:Y}_2\text{O}_3$ decorated Si NWs show a FF of $76 \pm 1\%$, $74 \pm 1\%$, and $69 \pm 1\%$ for 5°, 10°, and 15° angle, respectively. These data show a decreasing of the in-plan coverage by increasing the angle, in perfect agreement with the deeper coverage attested by EDX and SEM in cross-section. This effect can be understood considering that for higher angles the fill factor decreases, thus decreasing the aperture angle of the shadowing cone. The FF analysis demonstrates how the morphology of the $\text{Er:Y}_2\text{O}_3$ deposition can be tuned in the NWs plan as a function of the oblique angle used in the

sputtering process. A fractal typical feature is the scale invariance of the FF that is independent to the magnification [197]. Indeed, both the bare Si NWs and the Er:Y₂O₃ decorated Si NWs show about the same fill factor at different magnifications (5 kX, 50 kX, and 300 kX). After the FF analysis, the fractal dimension (D_f) and the lacunarity (λ_f) were investigated for all the deposition angles. As introduced in this chapter, the fractal dimension is a measure of the mass distribution scaling of the object in the range of scale invariance of the system [198]. For a fractal, the D_f is a non-integer value and for a 2D fractal is strictly minor than 2. The fractal dimension doesn't describe univocally a fractal and as discussed by Mandelbrot [199] another parameter is required. This parameter is the lacunarity that represent the statistical fluctuation of the mass probed by the box-counting algorithm for each fixed dimension ϵ of the boxes. It provides complementary information to the fractal dimension, describing how the fractal texture is organized in terms of the fluctuation of the distribution of the alternation of empty and filled spaces, i.e. heterogeneities [198]. In particular, in this case the lacunarity is a measure of the variance of the filled pixels with respect to the square average number of them measured for each box scale. Indeed, λ_f is not a single value but depends on the observation scale. As-synthesized Si NWs shown a fractal dimension of about 1.88 ± 0.02 corroborating the claim of the realization of a 2D fractal array and in agreement with the previous result on this material [21, 175]. The same measure on Er:Y₂O₃ decorated Si NWs produce a D_f that vary slightly from 1.97 to 1.94 increasing the tilt angle from 5 to 15°. Lacunarity measures were subsequently carried out by the same FracLac algorithm for each sample as a function of the box scale sets used for the fractal dimension calculation.

Name	Filling Factor Si+ Er:Y₂O₃	Filling Factor Er:Y₂O₃	Fractal Dimension D_F	Lacunarity Maximum (nm)
NW bare	42% ± 2%		1.88 ± 0.02	53 ± 1
5°	76% ± 1%	34% ± 1%	1.97 ± 0.01	120 ± 3
10°	74% ± 1%	30% ± 1%	1.96 ± 0.02	160 ± 6
15°	69% ± 1%	25% ± 1%	1.94 ± 0.02	190 ± 10

Table 3.2: Structural and fractal parameters obtained for all the Er:Y₂O₃ decorated Si NWs.

The observation scale length value at which the lacunarity assumes its maximum value is resumed for all samples in table 3.2. This length scale that maximize the lacunarity corresponds to the maximum fluctuation of the refractive index, thus increasing the scattering strength of the material. Figure 3.13d shows how the box of a fixed length are superimposed onto the SEM image (in magenta) of the 15° sample during the fractal dimension and lacunarity calculation. The process was iterated for different grid size from tens of nm to about $2 \mu\text{m}$ and iterated for 5 different initial grid positions in all the SEM images. The number of boxes $N(\epsilon)$ required to cover all the structure was counted as a function of the box dimension ϵ . By fitting the power scaling law of N as a function of ϵ it is possible to find the fractal dimension. As discussed in the first part of the chapter, the slope of the regression $\ln N(\epsilon) - \ln \epsilon$ for $\epsilon \rightarrow 0$ is taken as fractal dimension. The lacunarity is defined as $\lambda_f = 1 + \sigma^2/\mu^2$ with σ and μ that represent the variance and the average filled pixels measured at a certain box dimension, respectively. In Fig. 3.13e λ_f is reported as a function of the box size ϵ (observation scale) per each sample. In particular, in black is reported the trend obtained for the Si NWs bare, while the trends obtained for the decorated samples are shown in red, blue, and green for the 15° , 10° , and 5° , respectively. The results were corroborated by using different sampling approaches and similar results were obtained by both non-overlapping and overlapping box counting analyses. The lacunarity peak intensity, its length scale position, and the full width at half maximum (FWHM) were measure for each sample by fitting the lacunarity with a lorentian function. The peak intensity is a measure of the pixel fluctuation amplitudem while the box size ϵ at which correspond indicates the length scale of the hetherogenities maximum fluctuations. The FWHM represents the estention of the observation scale where the heterogeneteities have their maximum fluctuation. Bare Si NWs present a sharp lacunarity peak of 1.35 centered at $53 \pm 1 \text{ nm}$, with a FWHM of 50 nm and remains significant in the range from 30 nm to 200 nm. It can be concluded that the hole size distribution in bare Si NWs shows huge fluctuations for dimensions below 200 nm. The variance of the mass is maximazied for small observation lengths and is not very spread. On the contrary, the lacunarities of the different angle $Er:Y_2O_3$ decorated Si NWs have a higher FWHM and the peak is shifted to higher observation scale as a function of the angle. By increasing the angle the maximum of the heterogeneteis results both increased and shifted for higher lengths. In particular, with respect to bare Si NWs the intensity of the lacunarity peak decreases of about the 51%, 43%, and 40%

shifting towards bigger length scale of 120, 160, and 190 nm for the 5°, 10° and 15° decorated NWs samples, respectively. All the lacunarity peak values are summarized in Tab. 3.2 with all the FFs and fractal dimensions for each sample. The lacunarity peak shift and broadening is in agreement with the FF data, providing a strong confirmation that holes smaller than about 100 nm are occluded by the deposited material suppressing the holes fluctuations in this range. Increasing the deposition angle, as demonstrated by the SEM and EDX analysis, the Er:Y₂O₃ decorates a deeper section along the Si NWs profile increasing increasing the FF and with a higher number of holes whose size fluctuate randomly. Due to the shadowing effect for higher angles, bigger holes remain partially uncovered and their size distribution is highly fluctuant over a broader region (up to 800 nm). This increase the lacunarity peak and its FWHM that correspond to a stronger light trapping and a larger wavelength range where the light result trapped. The deposition tilt angle strongly affects all the structural properties of the samples, determining how the material is distributed onto the fractal NWs structure. This is a clear demonstration that the morphological and structural fractal parameters of the decorated Er:Y₂O₃ Si NWs can be engineered by varying the deposition angle. In this way, the refractive index fluctuation and the scattering of the system can be controlled. In order to demonstrate this point, the optical response of the bare NWs, Er:Y₂O₃ decorated NWs and Er:Y₂O₃ film onto Si bulk substrates have been characterized by photoluminescence (PL) spectroscopy. The photoluminescence spectra of bare Si NWs sample and of the Er:Y₂O₃ decorated Si bulk and Si NWs were acquired by using an HR800 Lab spectrometer from Jobin-Yvon Horiba equipped with a cooled CCD and an InGaAs array detectors for visible and infrared spectroscopy, respectively. The samples were pumped at the excitation wavelength of 476, 488, and 514 nm lines obtained from an Ar⁺ laser focused through a 100X objective (NA 0.9) onto the sample. The set up work in backscattering configuration and the same objective is used to acquire the PL signal. The excitation power measured onto the sample plane was of about 30 μW for all the PL spectra. All the signals were acquired at room temperature. The scattering microscopies of the sample surfaces were acquired by focusing the 514 laser line at a power of 100 μW onto the sample by using a 100x objective. The scattered light was collected in a backscattering configuration through the same objective with a uEye microscopy camera.

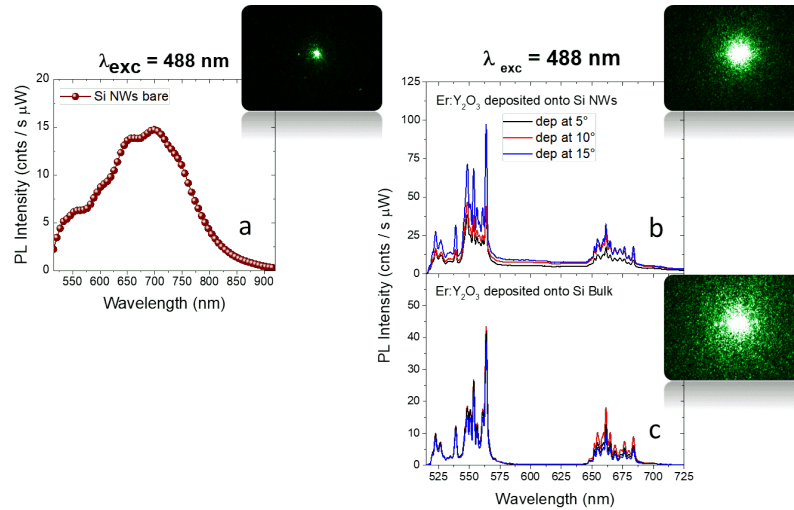


Figure 3.14: a) Si NWs bare PL emission at room temperature. $\text{Er:Y}_2\text{O}_3$ decorated Si NWs and Si bulk PL emission in the visible range excited through 488nm are shown in b) and c), respectively. In the upper right corner of any PL spectrum of each sample the scattering microscopy image, obtained by using a 532 nm excitation focused through a 100X, is reported.

In Fig. 3.14a the PL spectrum obtained for bare Si NWs excited at 488 is reported. It is clearly visible the typical NWs PL shape centered at about 700 nm due to the quantum confinement effect [25]. On the right upper part of the spectrum the light scattering obtained by bare Si NWs at 514 nm is reported. As can be observed, the light results very confined on the surface due to the strong light trapping of the 2D random fractal Si NWs. In Fig. 3.14b and c) the PL spectra obtained at 488 from $\text{Er:Y}_2\text{O}_3$ on Si NWs and Si bulk are reported, respectively. The PL signal shown in the spectra can be ascribed to the visible Er emission line. Indeed, 488 nm is resonant with the Er excitation channel and the peaks around 560 and 660 nm in the figure are clearly related to the $^4\text{I}_{15/2} \rightarrow ^4\text{F}_{9/2}$ Er^{3+} transition. The Si NWs PL emission is no longer visible by exciting the system at 488 nm (Er direct excitation) due to the higher efficiency of Er emission. By comparing the PL spectra obtained for decorated Si NWs to the spectra obtained for the decorated Si bulk is possible to observe a completely different trend as a function of the deposition angle. While in the Si bulk the Er PL emission is independent to the deposition angle, in the decorated Si NWs sample the

PL emission increases by increasing the angle. For the higher peak at 563 nm we measure a PL increment of 1.1 factor for the 10° sample and a factor of 2.4 higher for the 15° sample with respect to the sample deposited at 5° . This trend is due to the strong multiple scattering introduced by the fractal morphology that results in a pump efficiency enhancement and so in the increased Er PL emission [21]. On the right upper part of both Fig. 3.14b and c) the scattering microscopy obtained at 514 nm are reported for the 15° Si NWs and Si bulk sample, respectively. As it is clear to note the scattered light is maximized for the decorated Si bulk sample, while for the Er:Y₂O₃ decorated Si NWs is broader than the as-synthesized Si NWs. The scattering microscopies suggest that the light is better trapped into the Er:Y₂O₃ decorated NWs with respect to the decorated Si bulk sample. This better trapping of the light is responsible for the improved excitation pump efficiency. In order to attest the presence of a mediated excitation from Si NWs to Er ions, PL spectra for decorated Si NWs at 15° were acquired in an extended range from visible to IR under both direct (488 nm) and indirect (476 nm) excitation.

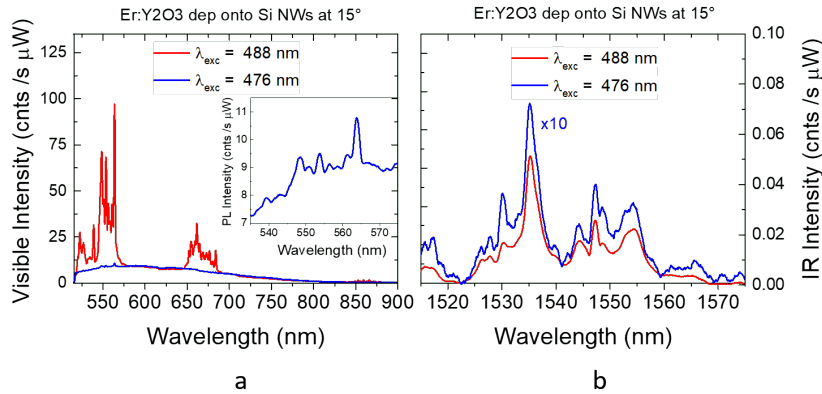


Figure 3.15: PL spectra comparison of Er:Y₂O₃ decorated Si NWs in direct excitation (488 nm, in red) and in indirect excitation (476 nm, in blue) are reported for visible and NIR range acquisition in a) and b), respectively.

Direct (red line) and indirect (blue line) excitation PL spectra are reported in Fig. 3.15a and b) for the Er significant range in visible and infrared, respectively. The visible and infrared Er emission signal corresponding to

$^4\text{S}_{3/2}$, $^4\text{F}_{9/2}$, and $^4\text{I}_{13/2}$ de-excitations appear to be very low. As suggested by the broadband peaked at 600 nm, the observed PL can be mainly attributed to defect emission. It is possible to conclude that no energy transfer mechanisms are present in this system under optical pump excitation. However, by considering the decorated Si bulk reference per each angle, similar PL enhancements are measured for all the emission wavelengths. This is a strong suggestion that the PL enhancement follows the structural morphology of the fractal structure. In particular, it is the lacunarity that drives the refractive index fluctuation and so, the PL enhancement. In order to fully demonstrate this point, the PL enhancement of the 560 nm Er band, obtained for the $\text{Er:Y}_2\text{O}_3$ decorated NWs scaled for the penetration depths of the excitation wavelength inside the material per each sample, was studied as a function of the excitation wavelength. The chosen excitation wavelengths were 364 nm, 476 nm, 488 nm, 514 nm, and the enhancement factors were defined as the Er PL intensity measured on decorated Si NWs with respect to the same intensity obtained for the same angle decorated Si bulk. This ratio was, finally, normalized for a scaling factor that takes into account the penetration depth of the different excitation length and the Er profile on Si NWs. Indeed, if all the emitting centers are optically active and fully illuminated by the laser probe, then the PL enhancement could be easily calculated from the ratio of the PL intensity measured from Er deposited onto Si NWs with respect to Si bulk. This is the case of the flat film deposited on Si bulk where we consider Er uniformly distributed into the Y_2O_3 matrix. In the decorated Si bulk case, moreover, the film deep is always lower than both the focal depth from which the signal is acquired and the inelastic length, representing the average length traveled by the light inside the material before its absorption. Unfortunately, this is not the case of the $\text{Er:Y}_2\text{O}_3$ decorated Si NWs. Indeed, as demonstrated by EDX the $\text{Er:Y}_2\text{O}_3$ deposit decreases from their tip to the bottom up to a maximum of 1.5 μm for the 15° sample. A scaling factor that takes into account the portion of Er ions effectively excited at the different wavelengths must be considered. The PL is acquired around 550 nm at which we are integrating the Er PL band and by taking into account the objective NA, we estimated a focal depth of about 1.2 μm . However, even if we are acquiring always the same wavelength region we are changing the excitation wavelength. Hence, a crucial parameter that must be considered is the inelastic length, accounting for the light that is absorbed from the Si NWs without being scattered and absorbed by the erbium. As discussed at the beginning of this chapter, the concentration of Si and SiO_2 in-plane for a

Si NWs slab can be obtained by the FF of the as-synthesized NWs. Indeed, as previously statistical demonstrated the realized Si NWs have an averaged radius of 7 nm with 5 nm of Si core and 2 of native SiO₂ as a surrounding shell. Considering the calculated FF for each deposition and subtracting the FF of bare Si NWs, the percentage of Y₂O₃ matrix (doped with 2 Er %) varies from 34% to 25% according to the deposition angle from 5° to 15°, consequently the remaining percentage will be composed of air (from about 15 to 25%). Since the Y₂O₃ matrix is highly transparent from 300 nm up to the whole visible region, its absorption within the decorated fractal system can be neglected. Meanwhile, the inelastic scattering and absorption of the 42% composition of Si must be considered. Indeed, at the excitation 364 nm in the UV region, the penetration depth is about 27 nm. This value is 2 order of magnitude less the penetration depth in the visible region. Indeed, the calculated penetration depth is 1050 nm, 1190 nm and 1665 nm for the wavelengths of respectively 476 nm, 488 nm, and 514 nm. The Er amount in the different deposition was the same as confirmed by RBS measurements. Hence, by considering that the depth increase by increasing the deposition angle, for a fixed total Er amount corresponds an Er concentration decrease. As reported by EDX, the Er:Y₂O₃ depth goes down to 1.5 μm, 1.25 μm, and 1.10 μm for 5°, 10°, and 5°, respectively. The effective fraction of Er ions involved was calculated by normalizing for the depth penetration of the excitation and for the decoration depth for each sample.

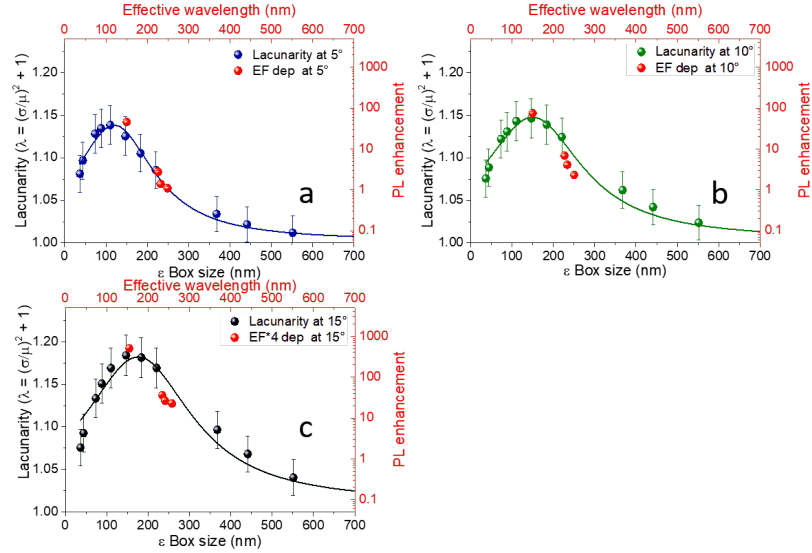


Figure 3.16: Normalized PL enhancement factors per probed volume calculated for the Er emission band at 560 nm (red dots) are compared to the lacunarity of the decorated Si NWs sample at 5° , 10° , 15° in a), b), and c), respectively.

The PL enhancement factors obtained as the 560 nm Er PL band measured on Si NWs with respect to the one obtained for Si bulk and normalized for the optically active Er fraction are reported as a function of the wavelength in Fig. 3.16. In particular, the enhancement factors obtained for the decoration at 5° , 10° , 15° are reported as red dots compared to the lacunarity curve obtained for the same samples in a, b, and c, respectively. The top axis report for each graph the effective wavelength obtained by the Bruggeman mixing rule, assuming that all samples have the same composition of 30% of Si and 15% of SiO_2 (measured from bare Si NWs) and different percentages of air and Y_2O_3 measured from the fill factor and confirmed by EDX analyses. As it is possible to observe a clear match between the PL enhancement factor trend and the lacunarity of the fractal system is present for all the investigated samples. Indeed, the lacunarity peak determines the maximum fluctuations for the refractive index, which correspond to the maximum scattering condition for the system. As expected a maximum of the PL enhancement corresponds to the maximum fluctuation of the refractive index of the fractal material. This is a strong demonstration that the optical

properties in terms of scattering and so, of emission, are driven by the fractal morphology of the system. In particular, the lacunarity emerges as a key parameter to modulate the erbium emission. Thanks to the possibility to control the fractal and lacunarity properties in a glancing angle deposition, this result opens new perspectives in the field of light management in novel photonic materials.

3.5 Conclusion

Fractal Si NWs have already been demonstrated to be a very appealing material for photovoltaics, as well as photonics, with the possibility to efficiently trap the light in a broadband region and as function of the fractal morphology. The light inside the fractal Si NWs medium results multiple scattered and eventually absorbed by the medium, making the samples look black. This strong multiple scattering inside the materials enhance all the scattering and absorption driven processes and a bright PL signal with a remarkable high Raman scattering is attested in these samples. Moreover, both the large scattering strength and the remarkable absorption, intrinsic in silicon materials, permitted to explore in depth the physics of Raman Coherent Backscattering (RCBS). RCBS appears as an all-optical process able to break reciprocity without the action of any external field and is uniquely linked to the scattering medium properties. The reciprocity breaking mechanism in RCBS was studied by 3D simulation of the hybrid path model that take into account Rayleigh and Raman events. Finally, this phenomenon was reported for the 2D random fractal Si NWs demonstrating both in simulation and experimentally how it depends on characteristic lengths of the random medium, such as the transport mean free path and the inelastic scattering length. This evidence paves the way for coherent control of waves in disordered materials just tuning their morphological and compositional characteristics, with important implications in future sensing technologies. The realization of novel artificial 2D fractal arrays based on Er:Y₂O₃ decorated Si NWs was shown. In particular, we successfully demonstrated the use of glancing angle sputtering to decorate fractal Si NWs with the possibility to tune the fractal morphology. By using this approach changing the deposition angle from 5° to 15° an increasing in the depth penetration up to 1.5 μm of the Er:Y₂O₃ was demonstrated. The Er concentration and the consistency between the different sputtering processes were confirmed through Rutherford backscat-

tering spectrometry. The fractal morphology was completely characterized in term of fractal dimension and lacunarity permitting to fully demonstrate the influence of the lacunarity of the system on the PL enhancement of the visible Er light emission. As expected, a maximum of the PL enhancement corresponds to the maximum fluctuation of the refractive index of the fractal material that is the maximum of the lacunarity. This is a demonstration that the optical properties in terms of scattering and so, of emission, are driven by the fractal morphology of the system. In particular, the lacunarity emerges as a key parameter to modulate the erbium emission. Thanks to the possibility to control the fractal and lacunarity properties in a glancing angle deposition, this result opens the route to new perspectives in the field of light management with a Si-compatible novel photonics materials.

Chapter 4

Different applications of silicon nanowires

Abstract

I^N this chapter different applications involving Si NWs are presented. On the first part, the realization a high performance catalysis platform based on the metal nanoparticles (NPs) decoration of Si NWs is shown. In particular, decorated Si NWs with Au and Cu NPs characterized by a chemically-shell free surface and a controllable diameter were realized by using a pulsed laser deposition approach. These substrate shown high catalysis performance for different applications such as C_{aryl} -N coupling reactions, carbonylation reaction, and reduction of nitroaromatic compounds. On the second part the optical trapping and manipulation of single Si NWs is shown. Only few years ago the Nobel price assigned to Ashkin was another time a strong demonstration of the potentialities of optical tweezers for applications that span from nanomaterials to bio-structure trapping and manipulation. However, the study of strong anisotropic structures is still scarcely explored. In this scenario, the dynamic of nanowires was deeply studied with a dual Gaussian beam trap configuration in different polarizations and finally, in a Laguerre-Gauss trap. A rich dynamic and several stable configurations were acquired with a perfect agreement with a Brown motion dynamics that consider hydro-dynamic coupling and interactions.

4.1 Silicon nanowires based catalysis platform

Surface and interface chemistry plays a crucial role in several applications involving innovative technology that rely on metals, semiconductors, and polymers. This branch of chemistry involves field as chemical bonding, adhesion, friction, electron and atom transport, solar energy conversion, and selective catalysis. In particular, catalysis emerges as the dominant application of the surface chemistry [200]. Nowadays, catalysis is of crucial interest in several fields especially, in industry. A recent study observed that in the USA catalysis processes are involved in more than one third of material gross national product. Indeed, several industrial product such as materials (high-strength polymers, stain-resistant fibers), expensive transportation fuels, high-temperature lubricants, chlorine-free refrigerants, and even cancer treatment drugs are just few of several thousands of goods that are possible thanks to catalysis applications. A catalyst is a material used to mediate the pathways by which chemical reactions occur, enabling highly selective formation of desired products at efficient rates. Catalyst is today applied in field as water waste purification and is considered a strategic resource for the reduction of air and water pollution. In particular, catalysis is considered a strategic tool to reduce products emissions that are considered harmful to human health and the environment [201].

Si NWs are emerging as a very interesting template to integrate other nanomaterials in silicon. The “More than Moore” philosophy is to integrate new functionalities and characteristics to a single processor instead of just increasing its calculus power. By following the same idea, the integration of other semiconductors on silicon is gaining the attention of the scientific and industrial community as an interesting route to enable new functionalities typical of other materials [144, 202]. In particular, the high surface area, the mechanical stability, and easy Si-industry compatible fabrication method make Si NWs as a promising host matrix to implement new material in silicon [203]. Among all the possible applications, a very interesting and challenging area is related to novel and performant substrates for catalysis. In order to address this point, our idea was to decorate Si NWs with metal nanoparticles (Me NPs) such as Au and Cu. The Si NWs dense forest structure offers a wide range of possibilities for further implementations. Among all the possible approaches for the decoration of Si NWs with Me NPs, the chemical routes are the most adopted ones. However, the use of chemical approaches does not permit a fine control of the NPs growth, size

and shape. By using galvanic reduction a further disadvantage is the presence of a chemical shell that surrounds the metal clusters, strongly limiting the applications of such systems. One of the most important points to address is the complete coverage of the all Si NWs matrix. Indeed, often the Si NWs are only partially decorated (commonly on the top part) strongly affecting the performance of the device [204–206]. In the last decade, several nanoscale metals have been anchored on Si NWs for catalytic purposes (Au [207, 208], Ag [209–211], Pd [212, 213], Pt [214–216], Cu [217, 218], etc.). Chemical reduction has been frequently employed as decoration method, with applications mainly in the degradation of dyes and pollutants [207, 209–214, 216, 217], but also in cross-coupling reactions [212, 218, 219]. In order to obtain a good metal nanoparticles coverage with the advantage of a chemical shell-free material, the pulsed laser ablation approach was successfully adopted by different groups [220–222]. By using this approach it is possible to realize a uniform and dense Si NWs decoration with a control on the size and interspacing between the Me NPs. The decorated NPs characteristics are a function of the experimental parameters such as gas nature, chamber pressure, laser fluence, and number of pulses. Previously, this approach was successfully used to decorate Si NWs with the realization of a SERS active substrate for enhanced Raman scattering sensing by Ag NPs [113, 221, 222]. Indeed, even if the realization of metal nanoscale covered Si NWs was adopted in different fields, before our study the realization of metal NPs decorated Si NWs through pulsed laser deposition for catalysis applications was lacking.

4.1.1 Decorated Si nanowires platform performances

Si NWs were fabricated through the use of the metal assisted chemical etching by silver salts. A (100)-oriented p-doped Si substrate was processed. Initially the samples were UV-ozone treated for 2 min and then immersed in a 5% hydrofluoric (HF) water solution. The surface oxygen-free Si was then immersed in the etching solution made of AgNO₃ 40%, H₂O 40%, and HF 20%. During the process silver clusters are formed and precipitate to the Si substrate acting as a catalyst for the silicon etching. Indeed, due to the electronegative difference at the Ag/Si interface an anodic reaction occurs, with the Ag that injects holes to the Si. The silicon underneath the metal results oxidized and, as a consequence of the HF in solution, is selectively etched. Ag clusters sink into the substrate and continue to etch the silicon with the formation of the Si NWs in the metal uncovered regions. After the

etching, the samples were immersed in a HNO_3 solution in order to remove the Ag dendrites formed during the etching. All the steps are at room temperature. After the realization of the $1.5 \mu\text{m}$ Si NWs, these sample were decorated through Pulsed Laser Deposition (PLD) with Au or Cu nanoparticles. The samples were inserted in a high vacuum chamber (10^{-4} Pa) and a KrF excimer laser beam (Lambda Physik CompEx 205, 25 ns pulse width, 248 nm wavelength, 10 Hz repetition rate, laser fluence set at $2.0 \text{ J}\times\text{cm}^{-2}$) was focused onto the surface of a pure gold or copper target using a quartz lens with the target mounted on a rotating holder to avoid excessive surface damaging. The Si NWs samples were placed 35 mm far from the PLD target.

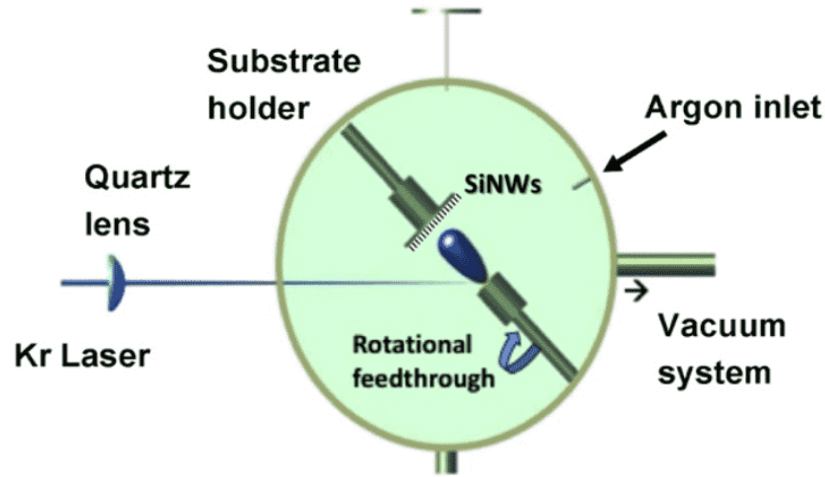


Figure 4.1: Scheme of the Pulsed Laser Deposition (PLD) approach for the Si NWs decoration. [?]

The PLD chamber is schematically illustrated in Fig. 4.1. The metal deposition process was performed in presence of 100 Pa of Ar for the case of Au, while a pressure of 70 Pa was used for the case of Cu. These two different pressures were optimized taking into account the atomic mass difference between the two metal (Cu 63.5 amu, Au 196.9 amu). Indeed, the NPs formation is led by the laser generated plasma interaction with the ambient gas inside the chamber [223]. As a consequence, an higher Ar pressure is needed to confine the Au plasma with respect to the Cu one. During the process, the plasma expands through the ambient gas forming a shock wave at the interface with the atmosphere ambient [224]. These conditions

drive the formation of metal clusters during the flight of the target material to the sample surface. In this way, metal nanoparticles are formed in-flight and land onto the Si NWs decorating them. A laser pulse number of 60K was used for both the two metals. Different samples were prepared though these conditions and the Au and Cu decorated Si NWs will be by now indicated as AuNPs@SiNWs and CuNPs@SiNWs, respectively. Si bulk was decorated together with the Si NWs and by using the same conditions to obtain a reference for the decoration and catalysis performances. The structural properties of the realized samples were investigated through a Scanning Electron Microscopy (SEM).

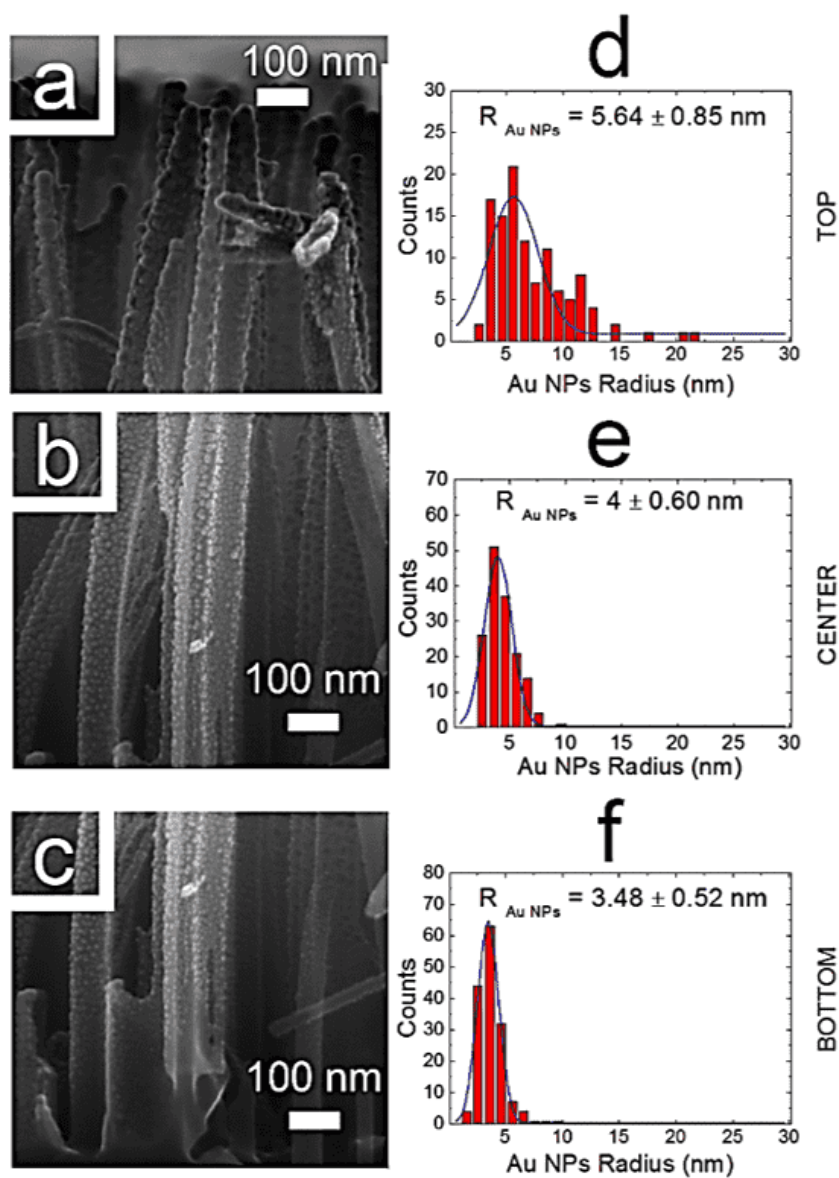


Figure 4.2: Cross section SEM images of top, center, and bottom region of the AuNPs@SiNWs in a), b), and c), respectively. Statistical analysis of the NPs radius dimension as a function of the Si NWs region from top to bottom in d), e), and f). [144]

In Fig. 4.2 the cross section SEM images of the AuNPs@SiNWs top,

center, and bottom region are reported in a), b), and c), respectively. As shown by the image and already demonstrated [113], the Si NWs arrays are not damaged during the PLD decoration process, and result fully decorated from the tips to the bottom region. The NPs dimension was analyzed through the statical analysis of the SEM images by using the analysis software ImageJ. In particular, as shown in Fig. 4.2d-f, the NPs on the Si NWs have an average radius of 5.6 ± 0.8 nm, 4 ± 0.6 nm, and 3.5 ± 0.5 nm for the top, center, and bottom region, respectively. The NPs radius was fitted by a Gaussian distribution. The metal nanoparticles result bigger on the top of the Si NWs and their dimension decrease going to the bottom part. This result is in perfect agreement with our previous study on the Si NWs decoration by PLD [113]. Indeed, the NPs are formed during the flight by the eroded target material before it reach the Si NWs substrate. At the beginning, the NPs arrive with the same average radius on the three different sections of the wires. The top region is more exposed compared to the bottom one, where a smaller fraction of NPs land. Thus, in the top region the formation of larger coalesced NPs happens determining the observed decreasing mean size of the metal NPs along the wire length from top to bottom, independently of the NW length and of the laser shots number.

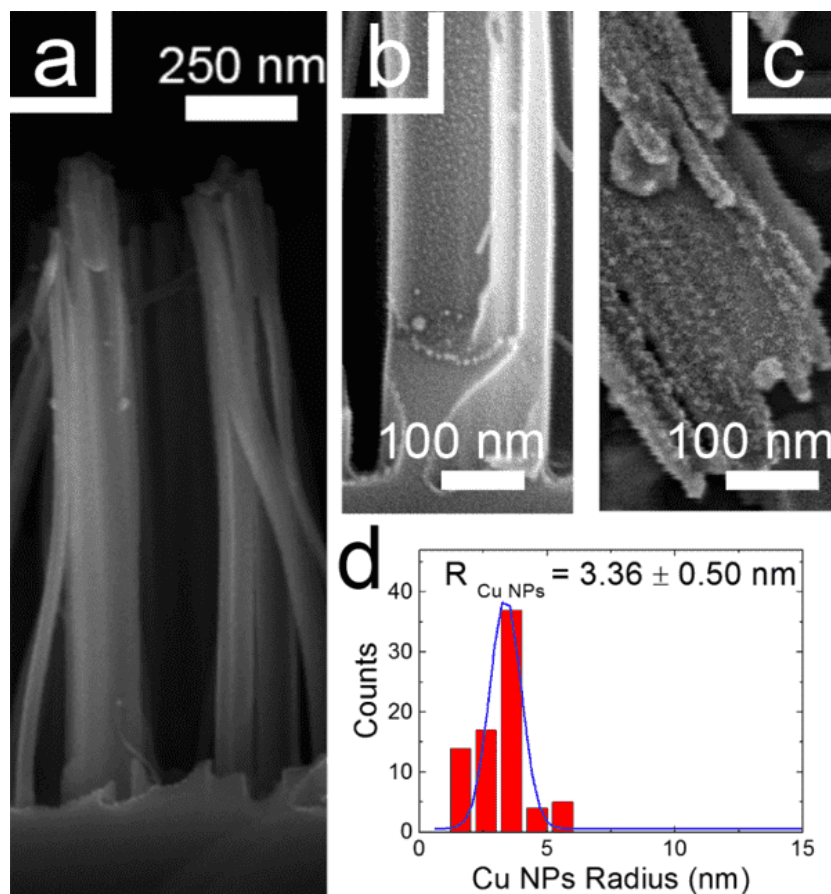


Figure 4.3: a) Cross section SEM image of CuNPs@SiNWs. Bottom and top region details of the decorated samples in b) and c), respectively. d) Statistical analysis of the NPs radius dimension in the top region. [144]

In Fig. 4.3a the cross section SEM image of the Si NWs decorated with Cu NPs is shown. The presence of the Cu nanoparticles is clearly attested from the bottom (Fig. 4.3b) to the top (Fig.4.3c) region of the Si NWs by the high magnification SEM images reported. The Cu NPs result visible in both the images but their average dimension is hardly to obtain for the bottom region where it reach the SEM resolution limit. In Fig. 4.3c the statistical analysis of the radius distribution obtained for the Si NWs top region is reported. In particular, a mean radius of about 3.4 ± 0.5 nm is attested, in good agreement with the results previously demonstrated for Ag NPs [113] and obtained for Au NPs (shown in Figure 4.2). The size difference

between Au and Cu NPs is due to the PLD conditions adopted that drive a different clustering dynamics. Moreover, the different wettability of the Si NWs surface respect the two different metals play an important role in the NPs final dimensions. The areal concentration of the decorating metals was obtained through a Rutherford Backscattering Spectrometry (RBS) analysis. In particular, for the CuNPs@SiNWs samples a concentration of 1.57×10^{17} Cu atoms/cm² (corresponding to 1.67×10^{-5} g/cm²) was obtained while for the AuNPs@SiNWs a concentration of 1.95×10^{17} Au atoms/cm² (6.41×10^{-5} g/cm²) was measured. After the morphology characterization the realized samples were tested in different catalytic activities.

C_{aryl}-N Coupling Reactions

In the recent years the use of gold nanoparticles-based catalysis device has attracted the scientific community. Au NPs were employed in several application such as cycloadditions, hydrogen generation, reduction of nitrophenols, and CO oxidation [225, 226]. Recent studies demonstrated that, despite the low catalytic performances of bulk copper, this material presents interesting performance at the nanoscale level [218]. Indeed, Pan et al. demonstrated remarkable performance in the catalysis of C-C and C-heteroatom bond formations and related reaction with copper(0) (metallic copper) nanoparticles [227]. In order to test the performances of the Me NPs decorated Si NWs as catalytic substrate, the C_{aryl}-N coupling of aryl halides with amines (Ullmann condensation) [228–230] was carried out. The Ullmann condensation is an interesting approach commonly adopted for the aromatic amines synthesis. Aromatic amines are considered of great interest thanks to their pharmaceutical and biological properties [231, 232]. However, until now the use of gold-based catalyst for these reaction didn't produce any significant result. Cu is much cheaper than other known active metal as Pd and Rh and several homogeneous Cu catalysts have been used for this reaction [233] but few heterogeneous counterparts have been reported [218, 234, 235]. By preliminary experiments the coupling conditions were optimized with respect to the model reaction between iodobenzene and butylamine. In particular, water was found as the most efficient solvent. This can probably be ascribed to two different aspects: i) the worse nucleophilic properties respect to the amine, that suppressed the competitive side-reaction of hydrolysis affording phenol; ii) the good solvent ability towards Cs₂CO₃. Among all the investigated bases, cesium carbonate resulted as the most performing base. The

effect of the temperature was similar to the other cases of the reaction in literature. A temperature below 110 °C results in low performances, while higher temperature have a decreasing of the selectivity as drawback.

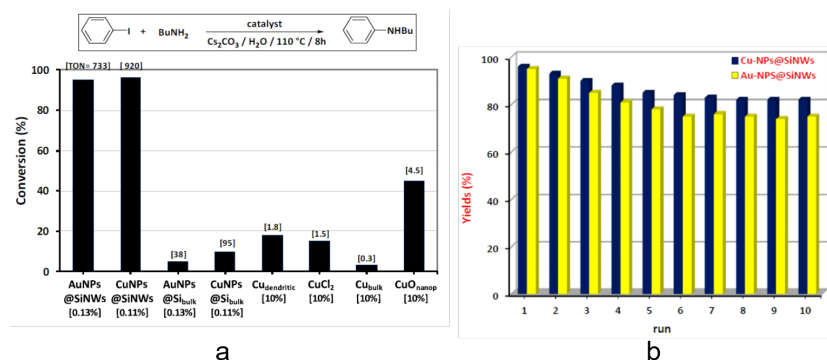


Figure 4.4: a) Comparison of the catalytic performances of decorated Si NWs with different Cu-based platform in the C–N coupling of iodobenzene with butylamine. b) Recycling experiment of Cu and Au NPs decorated Si NWs catalysis. [144]

In Fig. 4.4a the catalysis performances of Cu and Au NPs on Si NWs were compared with the reference samples of Cu and Au NPs on Si bulk and with similar platforms in literature. In this figure, the catalyst performances are both indicated as conversion percentage and turnover number (TON). The TON is a typical value used in literature that correspond to the moles number of converted iodobenzene per mole of surface metal (Cu or Au atoms) [140]. It is worth to note that not all the metal atom surface can be considered as a catalytic active site. Indeed, a big portion of the surface is bounded to the Si NWs and hence, unavailable for the catalysis. As commonly adopted in literature, the total number of surface metal atoms was used as number of the active catalytic sites [236] underestimating the catalytical performances of the platform. As shown in the Fig. 4.4a both the CuNPs@SiNWs and the AuNPs@SiNWs enabled the coupling at very low catalyst concentration (0.11 – 0.13 mol%) and with TON values of 920 and 733 for Cu and Au NPs, respectively. These remarkable performances are the best currently demonstrated with respect to the literature and from ten up to hundred times higher than the most commonly used Cu catalyst. On the contrary, the analogous Si bulk decorated with Cu and Au NPs produced modest results with TONs of ten

times lower. This is a strong demonstration of the crucial role of the Si NWs substrate to enhance the catalytic effect by dramatically increase the exposed surface of the metal nanoparticles as an effect of the Si NWs geometry with respect to the flat one of the Si bulk substrate. General applicability and limitation of this protocol were deeply investigated and both Cu and Au NPs decorated Si NWs shown similar performances. The highest performances were founds in the iodobenzene and primary aliphatic amine coupling with yield in the 75%-99% range. The coupling performances is related to both steric and electronic factors as demonstrated by lower yields corresponding to the case of hindered substrates such as 2-iodotoluene and dibutylamine or with the case of electron-rich substituents on the phenyl ring, like methoxy group. The Cu and Au NPs decorated Si NWs substrates have low performances with Aryl bromides and the aniline resulting in yield of 15-20% and seems to be uneffective on the alcoholic functionality. An interesting yield, higher than 90%, was obtained for the conversion of 4-mercaptobutan-1-ol into 4-(phenylthio)butan-1-ol. A crucial paramter for a catalysis substrate is the reciclability of the platform for further operations. In order to prove the stability of the Si NWs-based platform, a series of several recycling experiments were carried out as reported in Fig. 4.4b. After an initial activity decrease, occurred in the first four runs the catalyst performances seems to be stable. The initial performances deacrese can be ascribed to the metal nanoparticles depletion in the upper nanowires part due to the contact with the bulk reaction solution. The catalysis performance of both the metal NPs decorated Si NWs remains in the range of 75 and 80 % after 10 cycles strongly demonstrating the good anchoring of the NPs and the stability of the platform without loss of catalytic material. A strong advantage of this type of platform is the simplicity of its use. Indeed, after the catalysis experiments no further techniques, such as filtration or centrifugation, are required and the samples can be simply removed from the solution by a tweezers.

Carbonylation Reaction

As second test we choose carbonylation reaction due to the analogous pathway of the previous C-N hetero-coupling when the carbonylation occurs in presence of proper nucleophiles, such as alcohols or amines. This reaction occurs starting from the oxidative addition of metal to the haloarene, aromatic esters, and amides. All these molecules are considered extremely interesting for the realization of several agrochemical and pharmaceutical com-

pounds [237]. The chemistry of carbonylation reactions is dominated by palladium-based solutions [238, 239] with just few exceptions, as the use of nickel [240]. In this scenario, the use of other more cost-effective metal, as Cu, can have a disruptive impact for industrial applications. Furthermore, the use of Cu and Au catalyst based solutions has been considered inefficient for haloarenes carbonylations and no literature about a successful use of these metals is present [227]. After some preliminary testes, the AuNPs@SiNWs didn't produce any significant result, while CuNPs@SiNWs platform was capable of efficiently promoting these reactions. The Cu decorated Si NWs platform showed an array of iodoarenes as suitable substrates that can be easily converted into the corresponding benzamides (or benzoates) in the presence of amines (or alcohols) under CO pressure [144]. The reaction condition involving the amines were characterized by the use of water as solvent, 110 °C for 8 hours at a pressure of 20 atm. In this case water was chosen due to the ability of dissolving Cs_2CO_3 and suppressing the undesired side-reaction of solvolysis, that leads to phenol formation, due to its poor nucleophilicity. For the alcohols the temperature was of 130°C with a pressure of 30 atm and Et_3N as additive. This Cu decorated Si NWs platform shows high conversion rate, over 75%, for aliphatic amines, while low conversion rates were obtained with haloarenes and negligible results with bromobenzene [144]. The Cu NPs decorated Si NWs sample show excellent performances in the alkoxy carbonylation of iodobenzene [144]. In general, for the reactions that require Et_3N as an additive and a high selectivity, the performances were almost always above 90%, with the suppression of most of the side-reactions.

Reduction of Nitroaromatics

To further prove the potentialities of such Si NWs platform, the reduction of nitroaromatics was chosen as a further benchmark [241–245]. These type of compounds are of particularly interest to prevent water contamination. Indeed, as example, nitrophenols and their derivatives are present in waste water effluents coming from the production of pesticides. Another reason that push our research to these compounds is that nitrophenol compounds could be reduced to aminophenol dyes and pharmaceutical products. Commonly these compound are removed with adsorption techniques, but these approaches suffer of the generation of toxic slurries. It is worthy to note that the comparison of our platform with the others present in literature is not trivial since the NPs activity is strongly affected by their size, shape,

concentration, and by the reaction conditions. However, during our test the NPs decorated Si NWs platform shows performance comparable or higher to the literature, especially to the analogous composites prepared by galvanic decoration of silicon nanowires.

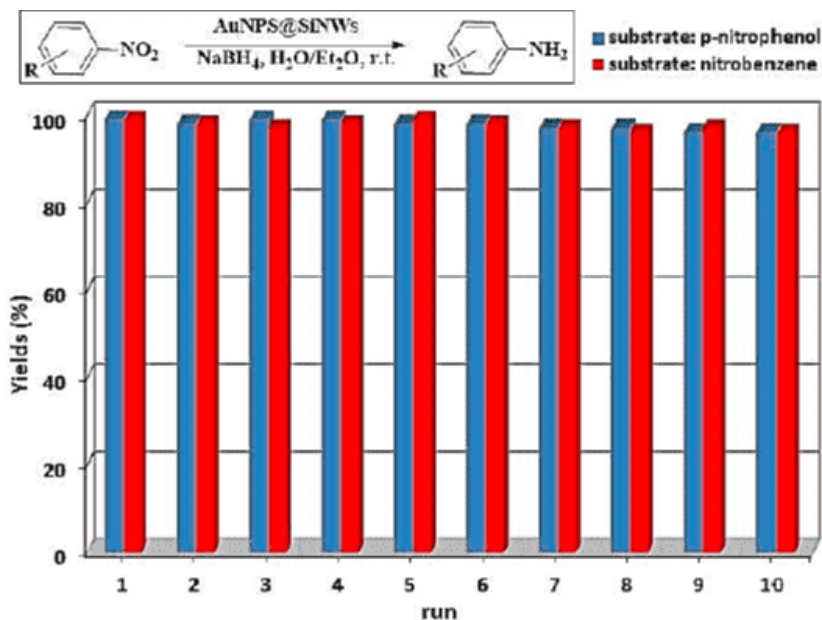


Figure 4.5: Recycling performances of AuNPs@SiNWs catalyst in the reduction of nitroarenes with NaBH₄. [144]

The recyclability of the platform was attested through 10 successive cycle under the same reaction conditions (as shown in Fig. 4.5). During this test the Si NWs platform doesn't show any loss of its activity both for gold and copper NPs nanocatalyst. Finally, an X-ray Photoelectron Spectroscopy (XPS) analysis was carried out before, and after, the use of the Si NWs platform in order to study the effect of the catalytic activity on the Me NPs decorated Si NWs. The analysis of the samples used for the catalyst activity clearly shows the presence of the metal nanocatalyst depletion, at least in the XPS sampling depth (10-20 nm). However, Au and Cu are still detectable and typical Au4f and Cu_{3/2} regions are reported in Fig. 4.6 a) and b), respectively.

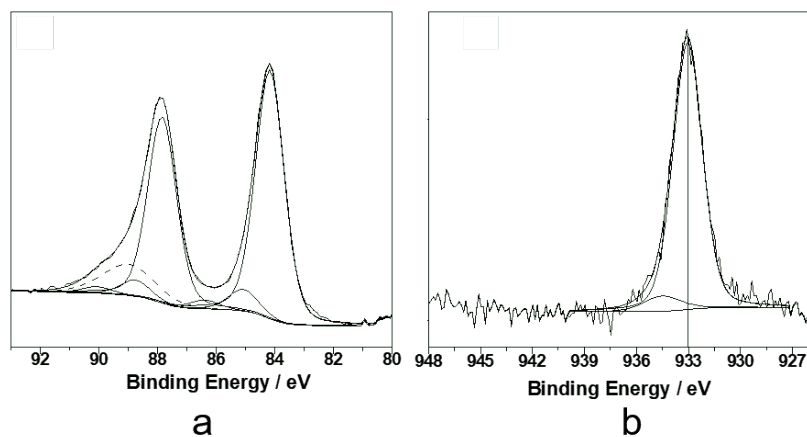


Figure 4.6: XPS spectra for Au decorated and Cu decorated Si NWs after catalysis experiment are reported in a) and b), respectively. a) Au4f XP region relevant to AuNPs@SiNWs (the dashed line corresponds to Mg2s signal, due to contamination); b) Cu2p_{3/2} XP region relevant to CuNPs@SiNWs (the vertical line indicates the position of the main component). [144]

For the case of the gold nanoparticles decorated Si NWs, the same components identified on pristine samples can be observed also on samples used in catalysis (Fig. 4.6a). In particular, a clear prevalence of gold silicides is outlined. Regarding the copper nanoparticles decorated Si NWs, as well as the same Cu components of the pristine sample, a new component falling at BE = 933.0 ± 0.2 eV is found (Fig. 4.6b). This signal can be ascribed to Cu-Si bond, again a case of metal silicides, demonstrating the intimate contact between the Cu NPs and the SiNW surface. This metal silicides component was probably undetected on the as-synthesized samples due to the air oxidation and the formation of surface oxide that cover the Cu-Si signal. The partial depletion that occur after the catalysis experiment make possible to detect the presence of these metal silicides after the use of the platform. The morphology of our system, the high exposed surface of the metal nanoparticles, and the systematic presence of these silicides on the sample surface are the reasons of this remarkable catalysis performances. In particular, the whole coverage of the $1.5 \mu\text{m}$ length NWs and the high density of wires allowed a continuous recycling of the catalyst for the reactions. Another crucial point is that the voids between the nanowires acts as “micro-reactors” confining the metal catalyst, which shows itself a great affinity towards the Si NWs. In this

hypothesis, if catalytic metals undergo a series of reaction and re-deposition cycles within the micro-channels, this could amplify the catalytic properties of MeNPs explaining the high performances demonstrated.

4.2 Optical trapping of silicon nanowires

After the laser discovery, innovative applications involving the radiation pressure interaction with microscale object were investigated. In these years, the Bell's laboratories were an incredible and strategic pole of the world top reaserch [246]. In these labs, Ashkin and Chu were working with various optical systems that could trap microscale objects, as well as atoms and molecules. In 1986, Ashkin, Chu, and other colleagues developed for the first time the concept of an optical tweezers with the demonstration of a single-beam optical trap [247]. In the optical trap the laser beam is extremely focused permitting to produces a gradient force that balances the radiation pressure confining the beam to the object focus. In 1997 the research of Chu was awarded with the Nobel Prize in Physics for his work on trapping and cooling of atoms by using laser optical traps [248]. During the same years, Ashkin focused his efforts on the study of biological systems in a totally new way, demonstrating that optical tweezers could trap and manipulate living cells, viruses [249, 250], and subcellular component in living cells [251], as well estimating the force that drives organelle transport along microtubules in amoebas [252]. This research soon became the engine for novel device applications. Indeed, the biologist Karin Schütze that worked with Ashkin on molecular motor forces in living cells measured through optical tweezers [252], co-funded a new company that create innovative devices for applications as cancer detection. These devices are based on new technology that couple optical tweezers and classical spectroscopy methods.

The radiation pressure, which idea was discussed even by Kepler in the 1662, was theorized by Maxwell, and demonstrated at the beginning of the last century. This physics phenomenon is extremely clear from a quantum mechanics point of view. Indeed, due to the duality particle-wave light carries a momentum $p = h/\lambda$ (with $h =$ Plank constant) that is function of the wavelength. Indeed, when an atom emits or absorbs a photon, its momentum changes according to Newton's laws. The existence of the radiation pressure means that an object will experience a force whenever a propagating light beam is refracted or reflected by its surface. For macroscopic objects this

force is so small that has a negligible effect with respect to all the other forces that act on the object. However, for microscopic objects these forces can have a significant effect and a focused laser beam can be used to trap a microscopic particle. The particle experience a 3D potential well and it is attracted near the focus of the light beam. When on the particle acts other forces that moves it from its equilibrium position, in first approximation the physics of the system can be described through the Hooke's law:

$$F_x = -k_x(x - x_0) \quad (4.1)$$

Where x represent the position of the particle and x_0 the equilibrium position with respect to the optical trap. k_x is the force stiffness, the equivalent of the spring constant respect the x -axis of the trap. Indeed, the 3 dimensional potential well due to the optical tweezers effect can be approximated by three independent harmonic oscillators, one for each axis-direction. Considering the light beam propagating through the z -direction, in the ideal case with all the optics aligned, the x and y spring constants are roughly the same, while the z spring constant is typically smaller by a factor of $\approx 5-10$. This point make feasible the study of biological object as cell, viruses, etc. Another class of object of particularly interest that could be affected and controlled by the radiation pressure are the nanostructures. Optical trapping of nanostructures [247, 253, 254] has acquired growing interest by the scientific community. Optical control of nanoparticles by optical trapping is commonly complicated by the presence of thermal fluctuation contributes that can easily overwhelm trapping force at the nanoscale [254]. Nanowires [255, 256], graphene [257], carbon nanotubes [258], polymer nanofibers [259] obtained during these years the interest of the academic community and have been stably trapped thanks to their highly anisotropic geometry. The applications involving these structures go from their manipulation to build nanoassemblies [260, 261], to the study and measure of femtoN forces of crucial interest for photonics force microscopy applications [255–257] In the presented application, Si NWs were manipulated in controlled optical traps based on counter-propagating beams, permitting to compensate detrimental light scattering forces. Optical trapped Si NWs dynamics are influenced by both optical and hydrodynamic interactions. In this work, an in-depth investigation of the rich dynamic of trapped nanowires is presented analyzing several polarization configurations that present different stable structures. All the results are in good agreement with Brownian dynamics considering an ap-

propriate optical and hydrodynamic coupling. This confirms that this rich scenario is crucially dependent on the non-spherical shape of the nanowires. Such an increased level of optical control of multiparticle structure and dynamics open perspectives for nanofluidics and multi-component light-driven nanomachines.

4.2.1 4.2.1. Silicon nanowires dynamics in dual beam traps

Another strategy employed to obtain a better trapping effect and to suppress the detrimental effect of the scattering forces is to use two counter-propagating beams [262]. Dual beam traps involve low-Numerical Apertures (low-NA) lenses and permit a reduced incident power with a wider focal region with respect to standard optical traps [263–265]. When the beams are linearly polarized in the same direction, a standing wave trap [266] is formed involving several equilibrium positions produced by the interference fringes along the beam axis [267]. The optical trapping and manipulation of spherical particles were extensively studied by the scientific community both experimentally [268–272] and theoretically [254, 268]. On the contrary, optical trapping of non-spherical objects is still partially explored both theoretically [273–276] and experimentally [265, 277–279]. The study of more complex asymmetric objects is of great interest to the evolution of new methods for optically controlled fabrication of microstructures and lattices [280], as well as particle delivery [281]. We decided to focus our efforts on the study of the rich dynamics of Si NWs under counter-propagating Gaussian and Laguerre–Gaussian beams with three different types of polarizations: parallel linear polarization (PLP), crossed linear polarization (XLP), and opposite circular polarization (CP). The obtained results were successfully in agreement with our theoretical simulations based on a Brownian dynamics characterized by optical and hydrodynamic interactions. For this application an IR 1064 nm laser (IPG, YLM-10-1064-LP-SP) was used. The counter-propagating beam trap is realized by using a holographic mask imprinted onto a single spatial light modulator (SLM) and transferred by relay optics. By the SLM we can control the waists of the two beam in the range 1.8–3.8 μm , and the power onto the sample in the range 25–80 MW. This correspond to a maximum power density of about 0.1–1.6 MW/cm² for the case of the smallest waist size of 1.8 μm . In order to increase the axial trapping sta-

bility, the two beam are slightly displaced of about $5 \mu\text{m}$ along the beam propagation axis.

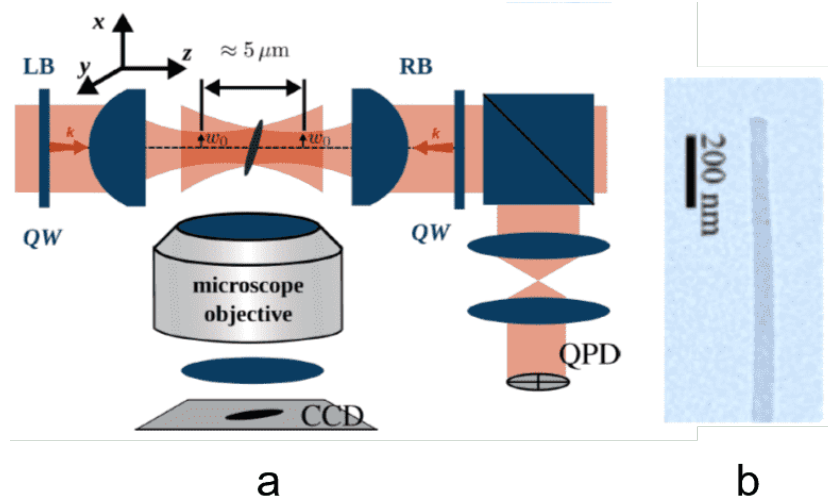


Figure 4.7: a) Dual Beam set up scheme. This is composed of two counter-propagating laser beams (left-hand beam, LB, and right-hand beam, RB) focused by two aspheric lenses ($\text{NA} = 0.5$, w_0 beam waist). QWs are the quarter wave plates used to set the beam polarizations. A microscope is used to observe the optically trapped Si NWs. b) TEM image of a typical Si NWs showing a good size uniformity along the Si NWs vertical axis. [78]

In Fig. 4.7a the experimental setup of the dual beam trap is schematized. The different type of polarization studied were obtained by quarter and half waveplates. Considering the z-axis parallel to the beam propagation the linearly polarized waves are polarized in the x-direction (vertical polarization) or y (horizontal polarization) direction. For the circular polarization case, the electric field vector rotates in the x-y plane and the counter-propagating beams have opposite handedness so that both the two electric field vectors rotate in the same sense. Silicon nanowires were synthesized by metal-assisted chemical etching through silver salts (see method described in 4.1.1), mechanically scratched from the substrate, and then stably dispersed by sonication in a aqueous solution of sodium dodecyl sulfate (SDS). The realized Si NWs have a length of $6 \mu\text{m}$ and a mean diameter of $78 \pm 16 \text{ nm}$. In Fig. 4.7b the TEM image of a typical Si NWs is reported. SDS is used to improve the temporal

stability of the dispersion toward aggregation and to minimize the sticking to the glass surface without the aid of surfactants. The solution is put inside glass squared capillary (Vitrocell) with an inner size of $50\ \mu\text{m}$. The capillary is inserted into the optical field of focused counter-propagating laser beams. A CCD camera (Basler Ac640–750) is used to acquire the signal of the Si NWs trapping and dynamics from a direction (y) perpendicular to the propagation z -axis. A complementary analysis is performed acquiring by an additionally quadrant photodiode (Thorlabs PDQ80A) the back focal plane interferometry and tracking signals from the trapping region [282]. Even if silicon is a low adsorber in the near IR at our power density, some small temperature effects might be expected [283,284] and the absorption of water might produce a thermal fluid flow. However, this phenomenon is suppressed by the use of the thin capillary [285] and the counter-propagating configuration that imply a waist wider than typical single-beam optical tweezers. These experimental choices ensure temperature effects smaller than a couple of degrees [284], as well as isotropic heating with consequent limited influence of thermophoretic flow along the Si NWs axial direction. In the absence of gradient forces, nanowires tend to align with the electric polarization [286]. In a classical single beam trap, if Si NWs are long enough or the focus is tight enough that Si NWs protrude beyond diffraction limited beam size, they tend to align with the beam axis [287–289]. In the case of a wavelength of $1064\ \text{nm}$ the Si NWs length critical to present this effect is about $0.4\ \mu\text{m}$. In the case of the dual beam trap the beam waist is relatively big ($1.8\text{--}3.8\ \mu\text{m}$) and, due to the interplay between the polarization and the gradient intensity aligning torques, the NWs can adopt several different configurations.

Parallel linear polarization

Let's start with the case of parallel linear polarization (PLP) with the electric field parallel to x -axis.

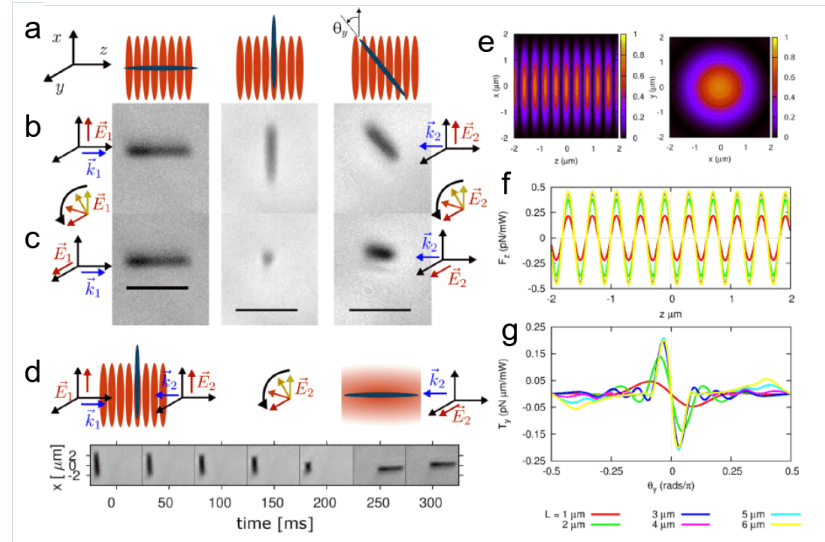


Figure 4.8: a) Si NWs optical trapping are sketched in parallel (PLP) configuration and as observed in b): parallel (left), perpendicular (middle), or tilted (right) with respect to the beams propagation axis. c) Alignment orientation change of a trapped Si NWs as a consequence of the rotation of the polarization of both beams. Scale bars correspond to $5 \mu\text{m}$. d) when the configuration is switched from PLP to XLP, the orientation of the Si NWs with respect to the beam propagation axis is switched from perpendicular to parallel. e) Calculated field intensity for PLP configuration showing the standing wave interference pattern along the propagation direction and the transverse Gaussian intensity profile on the left and on the right, respectively. f) Axial optical force F_z for Si NWs trapped and oriented along the polarization axis x , showing that trapping points correspond to the standing wave intensity maxima. g) Optical torque component T_y as a function of the angle that the nanowire makes with the polarization direction (x axis) θ_y . [78]

In this case a standing wave is formed with a series of high-intensity fringes distributed along the beam z -axis (see Figure 4.8) and parallel to the x - y plane. This configuration is characterized by a competition between the polarization torque, transverse high-intensity gradients, and elongated high-intensity structure of the counter-propagating beams. In Figure 4.8 the stable configuration observed for the NWs are schematized in a) and shown in b) and c). On the left is reported the configuration parallel to beam propagation axis, on the center the perpendicular one, and on the right the

tilted case. In particular, in c) the polarization of both beams is rotated from vertical to horizontal. As a consequence, the alignment of a trapped Si NWs is unchanged for parallel orientation (left), while it is rotated for the case of perpendicular (center) or tilted orientation (right) with respect to the beam axis. This effect due to the polarization optical torque controlling these orientation. The calculated field intensity for PLP configuration is reported in Fig. 4.8e showing the standing wave interference pattern along the propagation direction and the transverse Gaussian intensity profile on the left and on the right, respectively. In Fig. 4.8d the axial optical force F_z is reported for Si NWs trapped and oriented along the polarization axis x , showing that trapping points correspond to the standing wave intensity maxima. For several micrometers long Si NWs we observed the parallel configuration as the most stable orientation. This behaviour is theoretically supported as showed in Figure 4.8g by the optical torque component, with respect to the polarization direction, as a function of the angle between the NWs axis and the polarization axis x . As nanowires are rotated with respect to perpendicular axes to the beam axis (i.e., axes in the x - y plane), they intercept varying numbers of bright intensity fringes, generating series of tilted equilibrium configurations. The equilibrium configuration obtained with the Si NWs axis parallel to the polarization is the strongest one. However, this equilibrium position has a low angular range ($\pm 12^\circ$) and for rotation over this angle the equilibrium is lost. The perpendicular configuration is characterized by a weaker restoring torque force. However, the wider angular range of about 50° make this configuration one of the most observed. The oblique equilibrium position depends on the NWs length. Short NWs are commonly aligned following the polarization axis. However, configuration with an angle close to 45° between NWs and polarization in the x - z plane are found to be stable as observed on the right of Fig. 4.8b. The strong influence of the polarization torque was confirmed by rotating the beams polarization axis from x to y and observing the consequent controlled tilt of the trapped Si NWs (as shown in Figure 4.8c). Due to the high aspect ratio and asymmetrical geometry, NWs are mostly affected by translation with respect to its orthogonal direction, while are quite insensitive to parallel displacements [289, 290]. Indeed, the stiffness coefficient k_x in the polarization axis (x -axis) decreases exponentially by increasing the wire length. On the contrary, the k_y is about 3 orders of magnitude greater, as example for a $6 \mu\text{m}$ NWs $k_x/k_y \approx 1.3 \times 10^{-3}$. In particular, by increasing the wire length k_y approaches a constant value. Furthermore, the angular stiffness for tilt around

the y axis (i.e., out of the standing-wave high-intensity fringe) is about 2 orders of magnitude stronger than that for rotations around the z -axis (i.e., in the plane of the high-intensity fringe). When more than one Si NWs is trapped with PLP polarized beams, they tend to orient parallel or perpendicularly to each other. In this case, the arrangement of several particles is partially caused by the standing wave contribute. However, optical binding mediated by mutual scattering between Si NWs is also occurring [268].

Crossed Linear polarization

Adiabatically rotating the polarization of one beam the Si NWs trapped in the transverse plane and oriented along the polarization axis rotate until the polarizations of the beams are perpendicular. This condition correspond to the crossed linear polarization (XLP) case and the Si NWs switch to a longitudinal orientation along the z -axis (see Figure 4.8d). This stability orientation change is caused by the disappearance of the intensity fringes, which no longer confine the nanowires in the transverse plane. For long NWs the intensity gradient torques dominate causing their alignment along the beam axis, while short nanowires prefer to align orthogonally to the beam axis. For more than one Si NWs trapped in the crossed polarized XLP case, the distance d between Si NWs can be controlled with the beam waist, as happen for spherical objects [270, 280]. As already reported in literature [287, 291, 292], we find the presence of a non-conservative cycling when an equilibrium configuration has sufficiently low symmetry to permit nonsymmetric coupling between different freedom degrees. For example, in the left case of Figure 4.8a-b the stable state of a trapped Si NWs in PLP configuration is reached when it is aligned with the polarization axis. This equilibrium configuration is reached due to the impossibility of an asymmetric coupling between degrees of freedom. In literature when the symmetry is reduced, as for the presence of a taper [291], a bend [293], or if the NWs center is displaced from the beam axis, non-conservative effects are obtained. Similarly trapped Si NWs show non-conservative cycling whenever they find themselves in an equilibrium configuration with sufficiently low symmetry [273].

Circular polarization

The circular polarized counter-propagating trap was realized by putting a quarter waveplate in the path of each beam and setting their fast axes to $\pm 45^\circ$ with respect to the incident beam polarization. We set the experimental condition to obtain an opposite circular polarization σ^+/σ^- between the two beams. In this way, the two counter-propagating beam superposition generate a standing wave characterized by the rotation of the electric field around the beam propagation direction [265, 273]. We observe different equilibrium states with Si NWs stably oriented along or perpendicular to the beam propagation axis. The dynamic of the perpendicular orientation is particularly interesting. Indeed, in this case the spin angular momentum [273, 286, 294] is efficiently transferred from the light to the trapped NWs. As shown in Figure 4.9a this cause the rotation of the Si NWs with a frequency dependent on the Si NWs length. In particular, by decreasing the Si NWs length the rotational frequency increase. To confirm that the rotation is caused by the circular polarization, we verified that the rotation stops when the beam polarization is switched from circular to linear (horizontal or vertical). For transverse orientation we observed an efficiently rotation when the Si NWs center, or one of its edges, is a fixed point. The rotational dynamics acquired through the microscopy was studied by the correlation function analysis of the QPD tracking signals [258, 290, 291, 293, 295] analyzing the Si NWs rotational dynamic in the transverse plane (x-y). In particular, we studied the differential cross-correlation functions ($DCCF_{xy}$) [291, 295]. In our case the rotation of the Si NWs is reflected in the $DCCF_{xy}$ as a sinusoidal function with frequency related to the trapped particle rotational frequency [291, 295]. In particular, we fitted the z-axis cross-correlation function with the following expression [291, 295]:

$$DCCF_{xy} = A \sin(2\Omega\tau) \quad (4.2)$$

where A is a constant related to a calibration factor and Ω is the NWs rotational angular frequency. The factor 2 in Ω is related to the Si NWs symmetry [293]. In Figure 4.9b the typical $DCCF_{xy}$ of a rotating $3 \mu\text{m}$ long nanowire is reported. The corresponding tracking signal (V_x) is shown in the figure inset. By fitting three different case with the $DCCF_{xy}$ shown in eq. 4.2, an average rotational angular frequency $\omega = 42 \pm 1 \text{ rad/s}$ was measured. We obtained a similar result of 6.4 Hz independently from a

power spectral density (PSD) analysis (Fig. 4.9c) of the Si NWs rotational dynamics obtained from video microscopy.

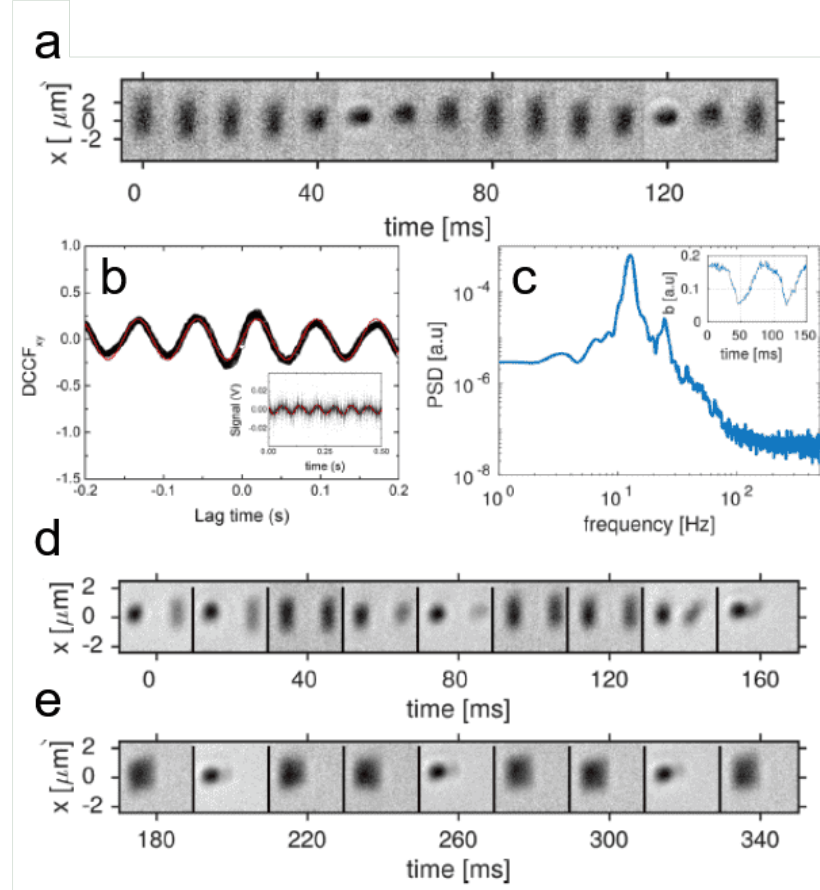


Figure 4.9: a) Image sequence of a nanowire with a length $L \approx 3 \mu\text{m}$ rotating with respect to the beam propagation axis in the circular polarization case. b) Transverse differential cross-correlation function DCCF_{xy} obtained from the transverse QPD tracking signals (inset). The fit is obtained with the sinusoidal function of eq 4.2. c) Power spectrum analysis of the aspect ratio modulation (inset) of the Si NWs images obtained from video microscopy. d), e) are the image sequences of a pair of Si NWs initially displaced far from each other that rotate independently. When they approach each other, their rotation synchronize and lock to a parallel orientation due to hydrodynamic interactions. [78]

The rotational dynamics of the Si NWs is determined by the viscous rotational drag torque related to the Si NWs rotational mobility $\Gamma_{\text{rot}} \approx 104$ ($\text{pN} \times \mu\text{m} \times \text{s})^{-1}$ and the spinning optical torque $T_z = \Omega/\Gamma_{\text{rot}}$. From the viscous rotational drag torque and the rotational angular frequency measures we obtained an optical spinning torque of $0.4 \text{ pN } \mu\text{m}$. The observed rotational dynamics of the Si NWs is slower compared to the typical values of plasmonic nanoparticles [296, 297]. This is because the transfer of spin angular momentum is caused by the anisotropic scattering related to the non-spherical shape [294] since Si NWs are not absorbing light. From the autocorrelation function ACFs analysis we analyzed the center of mass fluctuations. This method has already been proved for non-spherical nanostructures in standard optical traps [258, 290]. The exponential decay rates of ACFs (ω_x , ω_y , and ω_z) are related to translational fluctuations that through the knowledge of the Si NWs anisotropic hydrodynamic mobilities permit to obtain the optical force stiffnesses. Considering the z -axis we find the stiffness $k_z = \omega_z/\Gamma_{\perp}$ that correspond to the trap tighter confinement. Γ_{\perp} ($\approx 114 \mu\text{m pN}^{-1} \text{ s}^{-1}$ for our Si NWs) is the transverse translational mobility [258]. By using of $\omega_z = 331 \pm 83 \text{ rad/s}$ obtained from our measures an z -axis spring constant $k_z \approx 2.9 \text{ pN}/\mu\text{m}$ is obtained. In order to obtain the radial stiffness of the trap we can use the radial frequency $\omega_{\rho} = (\omega_x + \omega_y)/2$ by averaging the relaxation rate of the corresponding transverse ACFs and the radial mobility $\Gamma_{\rho} = (\Gamma_{\parallel} + \Gamma_{\perp})/2$ ($= \pm 142 \mu\text{m pN}^{-1} \text{ s}^{-1}$ for our Si NWs) by averaging the transverse and parallel mobilities. By using these values we obtained a radial stiffness $k_{\rho} \approx 0.8 \times \text{pN}/\mu\text{m}$, 3.6 times smaller than the axial one, (k_z), in agreement with the standing wave intensity pattern. As for the linear polarization cases, we observed optical binding also in the σ^+/σ^- configuration. In Figure 4.9d-e the optical binding that occurs by a pair of spinning Si NWs is shown through an image sequence. At the beginning the two Si NWs rotate independently since they are enough far from each other. As they get closer, their rotation become synchronized and the two Si NWs oriented parallel to each other. This behavior is in agreement with what is expected for a pairs of Si NWs in counter-propagating σ^+/σ^- plane waves [273] and is caused by optical binding between them and by their hydrodynamic synchronization at short-range [78]. It is noteworthy that for larger polystyrene microdiscs the synchronization has been observed at larger distances and with the two object perpendicular to each other, even for discs in contact [265, 276]. This is a demonstration of how the size and shape of the trapped particles has a crucial role in the trap binding and dynamic. During the experiments we

observed the dynamic of more than two NWs, and in agreement with theory [273], the Si NWs are unsynchronized no matter the rotational frequency or the distance between them. In these case, we also observed mixed configuration of both parallel and perpendicularly oriented Si NWs with respect to the beam propagation axis. As shown by the experiments, this optical binding effect can be used to hold two Si NWs synchronized and parallel to each other despite the diffusive influence of thermal fluctuations. The strength of this interaction depend on the distance between the two NWs. In particular, increasing the distance between the wires the optical interaction decreases. However, for 6 μm long Si NWs this interaction remain strong enough to bind them even for separation of 10 μm and at a modest beam power of ≈ 10 mW [78].

Laguerre–Gaussian Beams

Finally we study the optical trapping and dynamics of Si NWs by using two counter-propagating Laguerre–Gaussian beams with topological charge $l = \pm 1$ in both linear and circular polarizations. In Figure 4.10a a Si NWs bundle (thicker than an individual one) oriented parallel to the beam axis is shown. In this case for any polarization the stable position is off-centered with respect to the beam propagation axis due to the transfer of orbital angular momentum caused by the two counter-propagating Laguerre–Gaussian beams.

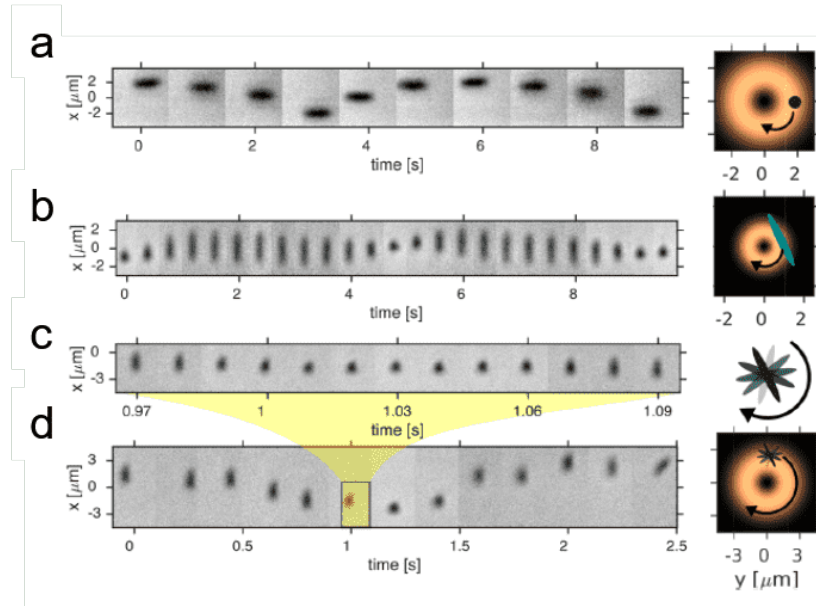


Figure 4.10: Counter-propagating circularly polarized Laguerre–Gaussian beam case with topological charge $l = \pm 1$. a) images of a nanowires aligned parallel to the beam propagation axis with a clear orbital motion around the optical vortex. b) images of a NWs aligned perpendicularly to the beam propagation axis with a reorientation of the Si NWs resulting from the transfer of both spin and orbital angular momentum of light. c) and d) are the simultaneous spinning and orbiting of a shorter nanowire. On the right part of the figure, the cross-sections of the beam are shown with sketches of the trapped nanowires. [78]

In the circular polarization case for short Si NWs the orientation result flipped and the Si NWs lies perpendicularly to the beam propagation (Fig. 4.10b). This is caused by the combined influence of spin and OAM [298]. In this case, spin and orbital rotations of the trapped Si NWs have about the same frequency of ≈ 0.1 Hz. This effect is clearly demonstrated in Fig. 4.10c with a Si NWs shorter than beam transverse size. In this case, the spinning rotation frequency measured is about 4.5 Hz while the intrinsic spinning has a rotational frequency of about 0.5 Hz. This difference between the two frequency produce a clear separation in the image sequence extracted from the movie acquired with the camera. It is possible to conclude that orbital angular momentum determine the precession of the wires around the beam

axis while gradient forces cause the gradient force effect is to obtain the NWs trapping off-centered with respect to the center of mass. Moreover, short Si NWs can strongly interact with the spin angular momentum, which causes them to rotate about their own centers, and with the orbital momentum of the beam, which determines their centers rotation around the beam axis.

4.3 Conclusion

Si NWs are already considered a strategic resource for different applications. Indeed, we investigated the use of metal nanoparticles (NPs) decorated Si NWs platforms as a high performance substrate for catalysis application. In particular, we decorated Si NWs with Cu or Au NPs by using a pulsed laser deposition approach. The platforms demonstrated high performances over the catalysis of different compounds such as C_{aryl}-N coupling reactions, carbonylation reaction, and reduction of nitroaromatic compounds. The performances reported by these substrates were unprecedented in the literature, especially for Cu NPs, and result extremely competitive and better than the common results. The advantage of a 3D Si-based platform with high surface to volume ratio and an industrially compatible approach with the high performances shown make these substrates extremely appealing for multifunctional catalysis applications.

On the second part of the chapter the optical trapping of Si NWs were studied in a dual counterpropagating beam trap configuration. The rich dynamics of single or multiple Si NWs were systematic investigated. In particular, we demonstrated that several microns long Si NWs prefer a stable orientation along the propagation axis for all the polarization state while shorter Si NWs prefer the direction along the transverse polarization axis. The distance between multiple Si NWs can be controlled with the width of the beam waists. Circular polarization condition induce a rotation of the Si NWs due to the transfer of spin angular momentum from the beam to the trapped Si NWs oriented perpendicular to the beam propagation axis. Si NWs trapping were also studied in counter-propagating Laguerre–Gaussian beams with opposite topological charge. In this case Si NWs tend to orbit around the beam axis and for circularly polarized beams they also spin around their symmetry axis, demonstrating how shape can couple spin and orbital angular momentum of light. The infrared negligible absorption of these Si NWs can be extremely appealing for their optical manipulation in biological environments, where

large heating effects might be detrimental. Optical trapping of Si NWs have also great potentiality for photodynamics therapy applications.

Bibliography

- [1] I. Feynman, Richard P. *There's plenty of room at the bottom* (1960).
[Http://resolver.caltech.edu/CaltechES:23.5.1960Bottom](http://resolver.caltech.edu/CaltechES:23.5.1960Bottom).
- [2] M. Von Ardenne. *Zeitschrift fur Physik* **109**, 553 (1938).
- [3] G. Binning et al. *Surface Science* **126**, 236 (1983).
- [4] G. Binning, et al. *Phys. Rev. Lett.* **56**, 930 (1986). URL <https://link.aps.org/doi/10.1103/PhysRevLett.56.930>.
- [5] I. A. R. Center. <https://www.nano.gov/nanotech-101/what/working-nanoscale> (1989).
- [6] USA. *National nanotechnology initiative, strategic plan*.
<https://www.nano.gov/NNIBudgetSupplementsandStrategicPlans>
(2014).
- [7] N. C. Reichardt et al. *Chem. Soc. Rev.* **42**, 4358 (2013).
- [8] S. Aldrich. *Gold nanoparticles: Properties and applications* (2019).
[Https://www.sigmaaldrich.com/technical-documents/articles/materials-science/nanomaterials/gold-nanoparticles.html](https://www.sigmaaldrich.com/technical-documents/articles/materials-science/nanomaterials/gold-nanoparticles.html).
- [9] T. Chen et al. *Semiconductor Nanocrystals and Metal Nanoparticles*
(CRC Press, Taylor and Francis Group, 2017).
- [10] M. M. Waldrop et al. *Nature* **530** (2016).

- [11] O. W. i. D. Max Roses. <https://ourworldindata.org/technological-progress> (2019).
- [12] K. Bourzac. *Cobalt could untangle chips' wiring problems* (2018). <https://spectrum.ieee.org/semiconductors/materials/cobalt-could-untangle-chips-wiring-problems>.
- [13] B. P. Bae. *Big data, for better or worse: 90% of world's data generated over last two years* (2013). <https://spectrum.ieee.org/semiconductors/materials/cobalt-could-untangle-chips-wiring-problems>.
- [14] B. Delley et al. *Phys. Rev. B* **47** (1993).
- [15] Intel. <https://www.intel.com/content/www/us/en/products/network-io/high-performance-fabrics/silicon-photonics.html> (2019).
- [16] Y. Cui, et al. *Nano Letters* **3**, 149 (2003). URL <https://doi.org/10.1021/nl10258751>.
- [17] J. Goldberger et al. *Nano Letters* **6** (2006).
- [18] W. Feng, et al. *Japanese Journal of Applied Physics* **51**, 04DC06 (2012). URL <https://doi.org/10.1143%2Fjjap.51.04dc06>.
- [19] E. Garnett et al. *Nano Letters* **10** (2010).
- [20] M. D. Kelzenberg, et al. *Nature Materials* **9**, 239 (2010). URL <https://doi.org/10.1038/nmat2635>.
- [21] B. Fazio, et al. *Light: Science & Applications* **5**, e16062 (2016). URL <https://doi.org/10.1038/lsa.2016.62>.
- [22] F. Priolo et al. *Nature Nanotechnology* **9** (2014).
- [23] A. Irrera, et al. *ACS Photonics* **5**, 471 (2017). URL <https://doi.org/10.1021/acsp Photonics.7b00983>.
- [24] A. A. Leonardi, et al. *ACS Sensors* **3**, 1690 (2018). URL <https://doi.org/10.1021/acssensors.8b00422>.
- [25] A. Irrera, et al. *Nanotechnology* **23**, 075204 (2012). URL <https://doi.org/10.1088/0957-4484/23/7/075204>.

- [26] C. D. Thomas, et al. *Nature* **427**, 145 (2004). URL <https://doi.org/10.1038/nature02121>.
- [27] W. energy outlook. *Total primary energy demand* (2019). <https://www.iea.org/weo/>.
- [28] N. Marigo. *Progress in Photovoltaics: Research and Applications* **15** (2007).
- [29] I. Fraunhofer Institute for Solar Energy Systems. *Photovoltaics report* (2016). <https://www.ise.fraunhofer.de>.
- [30] P. M. Fauchet. *Journal of Luminescence* **70**, 294 (1996). URL [https://doi.org/10.1016/0022-2313\(96\)82860-2](https://doi.org/10.1016/0022-2313(96)82860-2).
- [31] G. M. Credo, et al. *Applied Physics Letters* **74**, 1978 (1999).
- [32] C. Chiappini, et al. *Advanced Functional Materials* **20**, 2231 (2010). URL <https://onlinelibrary.wiley.com/doi/abs/10.1002/adfm.201000360>.
- [33] F. Erogbogbo, et al. *ACS nano* **4**, 5131 (2010).
- [34] G. Franzò et al. *Applied Physics A* **74** (2002).
- [35] L. Pavesi, et al. *Nature* **408**, 440 (2000). URL <https://doi.org/10.1038/35044012>.
- [36] A. Irrera, et al. *Nanotechnology* **20**, 135601 (2009). URL <https://doi.org/10.1088/0957-4484/20/13/135601>.
- [37] S. Walavalkar et al. *Nano Letters* **10** (2010).
- [38] S. Kalem et al. *Applied Physics A* **112** (2013).
- [39] M. J. L. Faro, et al. *Journal of Materials Science: Materials in Electronics* (2019). URL <https://doi.org/10.1007/s10854-019-00672-y>.
- [40] F. Patolsky et al. *Materials Today* **8**, 20 (2005). URL [https://doi.org/10.1016/s1369-7021\(05\)00791-1](https://doi.org/10.1016/s1369-7021(05)00791-1).
- [41] F. Patolsky et al. *Nanomedicine* **1** (2006).

- [42] V. Schmidt et al. *Advanced Materials* **21** (2009).
- [43] V. G. Dubrovskii, et al. *Physical Review B* **78** (2008). URL <https://doi.org/10.1103/physrevb.78.235301>.
- [44] S. Kodambaka, et al. *Phys. Rev. Lett.* **96**, 096105 (2006). URL <https://link.aps.org/doi/10.1103/PhysRevLett.96.096105>.
- [45] V. A. Nebolsin, et al. *Inorganic Materials* **41**, 1256 (2005). URL <https://doi.org/10.1007/s10789-005-0296-5>.
- [46] Y. Cui, et al. *Nano Letters* **3**, 149 (2003). URL <https://doi.org/10.1021/nl025875l>.
- [47] R. S. Wagner et al. *Applied Physics Letters* **4**, 89 (1964). URL <https://doi.org/10.1063/1.1753975>.
- [48] B. M. Kayes, et al. *Applied Physics Letters* **91**, 103110 (2007). URL <https://doi.org/10.1063/1.2779236>.
- [49] A. I. Hochbaum, et al. *Nano Letters* **5**, 457 (2005). URL <https://doi.org/10.1021/nl047990x>.
- [50] Y. Wu, et al. *Nano Letters* **4**, 433 (2004). URL <https://doi.org/10.1021/nl035162i>.
- [51] M. I. den Hertog et al. *Nano Letters* **8** (2008).
- [52] E. Koren et al. *Nano Letters* **10** (2010).
- [53] O. Gunawan et al. *Solar Energy Materials and Solar Cells* **93**, 1388 (2009). URL <https://doi.org/10.1016/j.solmat.2009.02.024>.
- [54] J. Nah, et al. *Applied Physics Letters* **94**, 063117 (2009). URL <https://doi.org/10.1063/1.3079410>.
- [55] E. F. Pecora, et al. *Applied Physics A* **102**, 13 (2010). URL <https://doi.org/10.1007/s00339-010-6040-2>.
- [56] E. Givargizov et al. *Journal of Crystal Growth* **9**, 326 (1971). URL [https://doi.org/10.1016/0022-0248\(71\)90250-8](https://doi.org/10.1016/0022-0248(71)90250-8).
- [57] V. A. Nebol'sin et al. *Inorganic Materials* **39** (2003).

- [58] B. Wu, et al. *Journal of Applied Physics* **108**, 051101 (2010). URL <https://doi.org/10.1063/1.3474652>.
- [59] H. Jansen, et al. *Journal of Micromechanics and Microengineering* **6**, 14 (1996). URL <https://doi.org/10.1088%2F0960-1317%2F6%2F1%2F002>.
- [60] C.-M. Hsu et al. *Applied Physics Letters* **93** (2008).
- [61] M. T. Ghoneim et al. *Small* **13**, 1601801 (2017). URL <https://doi.org/10.1002/sml1.201601801>.
- [62] J. Yeom, et al. *Journal of Vacuum Science & Technology B: Microelectronics and Nanometer Structures* **23**, 2319 (2005). URL <https://doi.org/10.1116/1.2101678>.
- [63] B. L. Fontaine. *Lasers and moore's law*. <http://spie.org/news/spie-professional-magazine/2010-october/lasers-and-moores-law?SSO=1> (2010).
- [64] T. Ito et al. *Nature* **406**, 1027 (2000). URL <https://doi.org/10.1038/35023233>.
- [65] L. Harriott. *Proceedings of the IEEE* **89**, 366 (2001). URL <https://doi.org/10.1109/5.915379>.
- [66] H. H. Solak, et al. *Journal of Vacuum Science & Technology B: Microelectronics and Nanometer Structures* **25**, 91 (2007). URL <https://doi.org/10.1116/1.2401612>.
- [67] M. Totzeck, et al. *Nature Photonics* **1**, 629 (2007). URL <https://doi.org/10.1038/nphoton.2007.218>.
- [68] H. W. P. Koops et al. *Journal of Vacuum Science & Technology B* **6** (1988).
- [69] A. Heuberger et al. *Proceedings SPIE* **0393** (1983).
- [70] S. Y. Chou, et al. *Science* **272**, 85 (1996). URL <https://doi.org/10.1126/science.272.5258.85>.

- [71] B. D. Gates, et al. *Chemical Reviews* **105**, 1171 (2005). URL <https://doi.org/10.1021/cr030076o>.
- [72] C. Vieu, et al. *Applied Surface Science* **164**, 111 (2000). URL [https://doi.org/10.1016/s0169-4332\(00\)00352-4](https://doi.org/10.1016/s0169-4332(00)00352-4).
- [73] M. LaPedus. *Toshiba claims to 'validate' nano-imprint litho*. https://www.eetimes.com/document.asp?doc_id=1167276 (2007).
- [74] J. K. W. Yang et al. *Journal of Vacuum Science & Technology B* **27** (2009).
- [75] M. S. M. Saifullah, et al. *Nanotechnology* **13**, 659 (2002). URL <https://doi.org/10.1088/0957-4484/13/5/323>.
- [76] H. G. Craighead. *Science* **290**, 1532 (2000). URL <https://doi.org/10.1126/science.290.5496.1532>.
- [77] X. Li et al. *Applied Physics Letters* **77**, 2572 (2000). URL <https://doi.org/10.1063/1.1319191>.
- [78] M. G. Donato, et al. *Nano Letters* **19**, 342 (2018). URL <https://doi.org/10.1021/acs.nanolett.8b03978>.
- [79] H. Li, et al. *Journal of Micromechanics and Microengineering* **27**, 124002 (2017). URL <https://doi.org/10.1088/1361-6439/aa96c4>.
- [80] H. Han, et al. *Nano Today* **9**, 271 (2014). URL <https://doi.org/10.1016/j.nantod.2014.04.013>.
- [81] Y. Harada, et al. *Journal of the American Chemical Society* **123** (2001).
- [82] I. H. Campbell et al. *Solid State Communications* **58** (1986).
- [83] M. Hjiri, et al. *Nanomaterials* **3**, 357 (2013). URL <https://doi.org/10.3390/nano3030357>.
- [84] Y. Engel, et al. *Angewandte Chemie International Edition* **49**, 6830 (2010). URL <https://doi.org/10.1002/anie.201000847>.
- [85] X. Chen, et al. *Cell Research* **18**, 997 (2008). URL <https://doi.org/10.1038/cr.2008.282>.

- [86] D. A. Morrow et al. *Circulation* **108**, 250 (2003). URL <https://doi.org/10.1161/01.cir.0000078080.37974.d2>.
- [87] N. Jhala, et al. *American Journal of Clinical Pathology* **126**, 572 (2006). URL <https://doi.org/10.1309/cev30be088cbdqd9>.
- [88] R. D. Fremont, et al. *The Journal of Trauma: Injury, Infection, and Critical Care* **68**, 1121 (2010). URL <https://doi.org/10.1097/ta.0b013e3181c40728>.
- [89] P. Schuetz, et al. *Swiss Medical Weekly* (2015). URL <https://doi.org/10.4414/smw.2015.14079>.
- [90] J. T. Whicher, et al. *CRC Critical Reviews in Clinical Laboratory Sciences* **18**, 213 (1982). URL <https://doi.org/10.3109/10408368209085072>.
- [91] E. Denham, et al. *Annals of Clinical Biochemistry* **44**, 529 (2007). URL <https://doi.org/10.1258/000456307782268237>.
- [92] P. D. Eckersall, et al. *Veterinary Research Communications* **15**, 17 (1991). URL <https://doi.org/10.1007/bf00497786>.
- [93] R. E. Chambers, et al. *Annals of Clinical Biochemistry: An international journal of biochemistry and laboratory medicine* **24**, 520 (1987). URL <https://doi.org/10.1177/000456328702400518>.
- [94] A. J. Bakker. *Clinical Chemistry* **34**, 82 (1988).
- [95] R. M. Lequin. *Clinical Chemistry* **51**, 2415 (2005). URL <https://doi.org/10.1373/clinchem.2005.051532>.
- [96] S. D. Gan et al. *Journal of Investigative Dermatology* **133**, 1 (2013). URL <https://doi.org/10.1038/jid.2013.287>.
- [97] S. Zhang, et al. *The Analyst* **139**, 439 (2014). URL <https://doi.org/10.1039/c3an01835k>.
- [98] C. Punyadeera, et al. *Journal of Immunological Methods* **373**, 19 (2011). URL <https://doi.org/10.1016/j.jim.2011.07.013>.
- [99] G. Zheng et al. *Nature Biotechnology* **23** (2005).

- [100] X. Zhao, et al. *Journal of the American Chemical Society* **125**, 11474 (2003). URL <https://doi.org/10.1021/ja0358854>.
- [101] M. R. Sierks, et al. *Integrative Biology* **3**, 1188 (2011). URL <https://doi.org/10.1039/c1ib00018g>.
- [102] J. H. An, et al. *Biosensors and Bioelectronics* **67**, 739 (2015). URL <https://doi.org/10.1016/j.bios.2014.10.049>.
- [103] C. A. Heid, et al. *Genome Research* **6**, 986 (1996). URL <https://doi.org/10.1101/gr.6.10.986>.
- [104] I. Mackay. *Clinical Microbiology and Infection* **10**, 190 (2004). URL <https://doi.org/10.1111/j.1198-743x.2004.00722.x>.
- [105] D. R. Almassian, et al. *Chemical Society Reviews* **42**, 8769 (2013). URL <https://doi.org/10.1039/c3cs60144g>.
- [106] J. Nurmi, et al. *Analytical Chemistry* **74**, 3525 (2002). URL <https://doi.org/10.1021/ac020093y>.
- [107] A. Forootan, et al. *Biomolecular Detection and Quantification* **12**, 1 (2017). URL <https://doi.org/10.1016/j.bdq.2017.04.001>.
- [108] M. A. Hoy. In *Insect Molecular Genetics*, pp. 307–372 (Elsevier, 2013). URL <https://doi.org/10.1016/b978-0-12-415874-0.00008-1>.
- [109] D. Mabey, et al. *Nature Reviews Microbiology* **2**, 231 (2004). URL <https://doi.org/10.1038/nrmicro841>.
- [110] H. Yoon et al. *Advanced Functional Materials* **19**, 1567 (2009). URL <https://doi.org/10.1002/adfm.200801141>.
- [111] K. Xu, et al. *Sensors* **9**, 5534 (2009). URL <https://doi.org/10.3390/s90705534>.
- [112] B. Fazio, et al. *Scientific Reports* **6** (2016). URL <https://doi.org/10.1038/srep26952>.
- [113] C. D'Andrea, et al. *Nanotechnology* **27**, 375603 (2016). URL <https://doi.org/10.1088/0957-4484/27/37/375603>.

- [114] K. Sapsford, et al. *Sensors* **6**, 925 (2006). URL <https://doi.org/10.3390/s6080925>.
- [115] A. P. Alivisatos. *Science* **271**, 933 (1996). URL <https://doi.org/10.1126/science.271.5251.933>.
- [116] K. Dohnalová, et al. *Light: Science & Applications* **2**, e47 (2013). URL <https://doi.org/10.1038/lsa.2013.3>.
- [117] J. M. Costa-Fernández, et al. *TrAC Trends in Analytical Chemistry* **25**, 207 (2006). URL <https://doi.org/10.1016/j.trac.2005.07.008>.
- [118] R. Freeman, et al. *Advanced Materials* **24**, 6416 (2012). URL <https://doi.org/10.1002/adma.201202793>.
- [119] H. Wei, et al. *Environmental Science: Nano* **2**, 120 (2015). URL <https://doi.org/10.1039/c4en00211c>.
- [120] Z. A. Peng et al. *Journal of the American Chemical Society* **123**, 183 (2001). URL <https://doi.org/10.1021/ja003633m>.
- [121] M. Zayats, et al. *Journal of the American Chemical Society* **125**, 16006 (2003). URL <https://doi.org/10.1021/ja0379215>.
- [122] G. Compagnini, et al. *Physical Chemistry Chemical Physics* **1**, 2351 (1999). URL <https://doi.org/10.1039/a901034c>.
- [123] S. M. Kwon, et al. *Journal of Nanoscience and Nanotechnology* **11**, 1511 (2011). URL <https://doi.org/10.1166/jnn.2011.3417>.
- [124] Y. L. Bunimovich, et al. *Journal of the American Chemical Society* **128**, 16323 (2006). URL <https://doi.org/10.1021/ja065923u>.
- [125] K.-I. Chen, et al. *Nano Today* **6**, 131 (2011). URL <https://doi.org/10.1016/j.nantod.2011.02.001>.
- [126] B. Maeng, et al. *RSC Advances* **6**, 7384 (2016). URL <https://doi.org/10.1039/c5ra21665f>.
- [127] K. Urmann, et al. *Analytical Chemistry* **87**, 1999 (2015). URL <https://doi.org/10.1021/ac504487g>.

- [128] C. M. Gonzalez et al. *Journal of Materials Chemistry C* **4**, 4836 (2016). URL <https://doi.org/10.1039/c6tc01159d>.
- [129] M. C. McAlpine, et al. *Nature Materials* **6**, 379 (2007). URL <https://doi.org/10.1038/nmat1891>.
- [130] M. CHENG, et al. *Current Opinion in Chemical Biology* **10**, 11 (2006). URL <https://doi.org/10.1016/j.cbpa.2006.01.006>.
- [131] R. Beckman et al. *Science* **310**, 465 (2005). URL <https://doi.org/10.1126/science.1114757>.
- [132] S. M. Lo, et al. *Optics Express* **25**, 7046 (2017). URL <https://doi.org/10.1364/oe.25.007046>.
- [133] M. F. Pineda, et al. *IEEE Sensors Journal* **9**, 470 (2009). URL <https://doi.org/10.1109/jsen.2009.2014427>.
- [134] S. Ögüt, et al. *Physical Review Letters* **79**, 1770 (1997). URL <https://doi.org/10.1103/physrevlett.79.1770>.
- [135] T. Takagahara et al. *Physical Review B* **46**, 15578 (1992). URL <https://doi.org/10.1103/physrevb.46.15578>.
- [136] R. J. Walters, et al. *Nature Materials* **4**, 143 (2005). URL <https://doi.org/10.1038/nmat1307>.
- [137] X. Wu, et al. *Nanomedicine: Nanotechnology, Biology and Medicine* **10**, 297 (2014). URL <https://doi.org/10.1016/j.nano.2013.08.008>.
- [138] O. Bisi, et al. *Surface Science Reports* **38**, 1 (2000). URL [https://doi.org/10.1016/s0167-5729\(99\)00012-6](https://doi.org/10.1016/s0167-5729(99)00012-6).
- [139] M. V. Wolkin, et al. *Physical Review Letters* **82**, 197 (1999). URL <https://doi.org/10.1103/physrevlett.82.197>.
- [140] B. Fazio et al. *Nature Photonics* **12** (2017).
- [141] C. Chiappini, et al. *Advanced Functional Materials* **20**, 2231 (2010). URL <https://doi.org/10.1002/adfm.201000360>.

- [142] S. Chan, et al. *physica status solidi (a)* **182**, 541 (2000). URL <https://onlinelibrary.wiley.com/doi/abs/10.1002/1521-396X%28200011%29182%3A1%3C541%3A%3AAID-PSSA541%3E3.0.CO%3B2-%23>.
- [143] X. Wu, et al. *Nanomedicine: Nanotechnology, Biology and Medicine* **10**, 297 (2014). URL <https://doi.org/10.1016/j.nano.2013.08.008>.
- [144] M. Casiello, et al. *Nanomaterials* **8**, 78 (2018). URL <https://doi.org/10.3390/nano8020078>.
- [145] A. Irrera, et al. *Semiconductor Science and Technology* **32**, 043004 (2017). URL <https://doi.org/10.1088/1361-6641/aa60b8>.
- [146] T. Collaboration. *New England Journal of Medicine* **367**, 1310 (2012). URL <https://doi.org/10.1056/nejmoa1107477>.
- [147] J. Salazar, et al. *Cardiology Research and Practice* **2014**, 1 (2014). URL <https://doi.org/10.1155/2014/605810>.
- [148] C. Mueller, et al. *Circulation* **105**, 1412 (2002). URL <https://doi.org/10.1161/01.cir.0000012625.02748.62>.
- [149] P. M. Ridker. *Circulation* **103**, 1813 (2001). URL <https://doi.org/10.1161/01.cir.103.13.1813>.
- [150] E. J. Benjamin, et al. *Circulation* **135** (2017). URL <https://doi.org/10.1161/cir.0000000000000485>.
- [151] S. Bandhavkar. *Clinical Microbiology: Open Access* **05** (2016). URL <https://doi.org/10.4172/2327-5073.1000234>.
- [152] N. Gitlin. *Clinical Chemistry* **43**, 1500 (1997). URL <http://clinchem.aaccjnls.org/content/43/8/1500>.
- [153] S. Petralia, et al. *The Analyst* **142**, 2090 (2017). URL <https://doi.org/10.1039/c7an00202e>.
- [154] S. Anwar et al. *Laser Physics Letters* **12**, 076001 (2015). URL <https://doi.org/10.1088/1612-2011/12/7/076001>.

- [155] N. Yamazoe et al. In *Semiconductor Gas Sensors*, pp. 3–34 (Elsevier, 2013). URL <https://doi.org/10.1533/9780857098665.1.3>.
- [156] G. Neri. *Chemosensors* **3**, 1 (2015). URL <https://doi.org/10.3390/chemosensors3010001>.
- [157] F. Rettig et al. In *Semiconductor Gas Sensors*, pp. 261–296 (Elsevier, 2013). URL <https://doi.org/10.1533/9780857098665.2.261>.
- [158] A. Mirzaei, et al. *Ceramics International* **42**, 15119 (2016). URL <https://doi.org/10.1016/j.ceramint.2016.06.145>.
- [159] A. Dey. *Materials Science and Engineering: B* **229**, 206 (2018). URL <https://doi.org/10.1016/j.mseb.2017.12.036>.
- [160] Y. Navale, et al. *Ceramics International* **45**, 1513 (2019). URL <https://doi.org/10.1016/j.ceramint.2018.10.022>.
- [161] J. F. Gouyet. *Physics and fractal structures* (Springer, 1996).
- [162] A. Lesne et al. *Scale Invariance: From Phase Transitions to Turbulence* (Springer, 2012).
- [163] B. B. Mandelbrot. *Fractals: form, chance, and dimension* (Freeman, 1977).
- [164] B. Mandelbrot. *Science* **156** (1967).
- [165] J. W. Kirchner, et al. *Nature* **403**, 524 (2000). URL <https://doi.org/10.1038/35000537>.
- [166] E. Aslan, et al. *ACS Photonics* **3**, 2102 (2016). URL <https://doi.org/10.1021/acsp Photonics.6b00540>.
- [167] B. B. Mandelbrot. *Annals of Finance* **1**, 193 (2005). URL <https://doi.org/10.1007/s10436-004-0008-1>.
- [168] J. A. Wasserman et al. In *Studies in Symbolic Interaction*, pp. 29–62 (Emerald Group Publishing Limited, 2011). URL [https://doi.org/10.1108/s0163-2396\(2011\)0000037004](https://doi.org/10.1108/s0163-2396(2011)0000037004).
- [169] V. Krachmalnicoff et al. *Physical Review Letters* **105** (2010).

- [170] S. R. Broadbent et al. *Mathematical Proceedings of the Cambridge Philosophical Society* **53** (1957).
- [171] J. M. Hammersley. *The Annals of Mathematical Statistics* **28** (1957).
- [172] S. Smirnov et al. *Comptes Rendus de l'Académie des Sciences - Series I - Mathematics* **333** (2001).
- [173] G. B. Smith et al. *Physical Review B* **78** (2008).
- [174] J. Laverdant et al. *Physical Review B* **77** (2008).
- [175] M. J. L. Faro, et al. *Journal of Materials Science: Materials in Electronics* (2019). URL <https://doi.org/10.1007/s10854-019-00672-y>.
- [176] R. F. Voss et al. *The Mathematics and Physics of Disordered Media: Percolation, Random Walk, Modeling and Simulation Lecture Notes in Mathematics*. Berlin Heidelberg: Springer **1035** (1983).
- [177] T. G. Andersson. *Gold Bulletin* **15** (1982).
- [178] D. A. G. Bruggemann et al. *Annals of Physics* **24** (1935).
- [179] D. E. Aspnes et al. *Physics Review B* **27** (1983).
- [180] Y. F. Huang et al. *Nature Nanotechnology* **2** (2007).
- [181] E. Akkermans et al. *Mesoscopic Physics of Electrons and Photons* (Cambridge University Press, 2007). URL <https://doi.org/10.1017/cbo9780511618833>.
- [182] D. S. Wiersma. *Nature Photonics* **6**, 506 (2012). URL <https://doi.org/10.1038/nphoton.2012.187>.
- [183] K. Müller, et al. *Physical Review Letters* **114** (2015). URL <https://doi.org/10.1103/physrevlett.114.205301>.
- [184] F. A. Erbacher, et al. *Europhysics Letters (EPL)* **21**, 551 (1993). URL <https://doi.org/10.1209/2F0295-5075/2F21/2F5/2F008>.
- [185] S. E. Skipetrov. *Nature Photonics* **11**, 144 (2017). URL <https://doi.org/10.1038/nphoton.2017.18>.

- [186] D. S. Wiersma. *Light in strongly scattering and amplifying random media* (PhD Thesis, 1995).
- [187] A. Irrera, et al. *Journal of Applied Physics* **107**, 054302 (2010). URL <https://doi.org/10.1063/1.3319581>.
- [188] K. Suh, et al. *Optics Express* **18**, 7724 (2010). URL <https://doi.org/10.1364/oe.18.007724>.
- [189] X. Wang, et al. *Optical Materials Express* **8**, 2970 (2018). URL <https://doi.org/10.1364/ome.8.002970>.
- [190] X. Zhang, et al. *Advanced Materials* **29**, 1604431 (2017). URL <https://doi.org/10.1002/adma.201604431>.
- [191] M. Miritello, et al. *Advanced Materials* **19**, 1582 (2007). URL <https://doi.org/10.1002/adma.200601692>.
- [192] T. T. Van, et al. *Journal of Applied Physics* **100**, 023115 (2006). URL <https://doi.org/10.1063/1.2214299>.
- [193] X. Wang, et al. *Journal of Materials Chemistry* **21**, 4251 (2011). URL <https://doi.org/10.1039/c0jm03761c>.
- [194] A. Scarangella, et al. *Scientific Reports* **7** (2017). URL <https://doi.org/10.1038/s41598-017-17567-9>.
- [195] Y. Mao, et al. *Journal of Applied Physics* **105**, 094329 (2009). URL <https://doi.org/10.1063/1.3117520>.
- [196] R. L. Savio, et al. *Journal of Applied Physics* **106**, 043512 (2009). URL <https://doi.org/10.1063/1.3195077>.
- [197] L. S. Liebovitch et al. *Complexity* **5**, 34 (2000). URL [https://doi.org/10.1002/1099-0526\(200003/04\)5:4<34::aid-cplx5>3.0.co;2-3](https://doi.org/10.1002/1099-0526(200003/04)5:4<34::aid-cplx5>3.0.co;2-3).
- [198] R. E. Plotnick, et al. *Physical Review E* **53**, 5461 (1996). URL <https://doi.org/10.1103/physreve.53.5461>.
- [199] B. B. Mandelbrot. In *Fractals in Biology and Medicine*, pp. 8–21 (Birkhäuser Basel, 1994). URL https://doi.org/10.1007/978-3-0348-8501-0_2.

- [200] G. A. Somorjai et al. *Introduction to Surface Chemistry and Catalysis, 2nd Edition* (Wiley, 2010).
- [201] A. T. Bell. *Science* **299**, 1688 (2003). URL <https://doi.org/10.1126/science.1083671>.
- [202] M. L. Faro, et al. *Nanomaterials* **8**, 569 (2018). URL <https://doi.org/10.3390/nano8080569>.
- [203] R. Elnathan, et al. *Nano Today* **9**, 172 (2014). URL <https://doi.org/10.1016/j.nantod.2014.04.001>.
- [204] E. Galopin, et al. *ACS Applied Materials & Interfaces* **1**, 1396 (2009). URL <https://doi.org/10.1021/am900087s>.
- [205] M.-W. Shao, et al. *Applied Physics Letters* **93**, 233118 (2008). URL <https://doi.org/10.1063/1.2969292>.
- [206] M.-L. Zhang, et al. *The Journal of Physical Chemistry C* **114**, 1969 (2010). URL <https://doi.org/10.1021/jp902775t>.
- [207] S. Naama, et al. *Materials Research Bulletin* **76**, 317 (2016). URL <https://doi.org/10.1016/j.materresbull.2015.12.046>.
- [208] M. Shao, et al. *Applied Physics Letters* **93**, 243110 (2008). URL <https://doi.org/10.1063/1.3043459>.
- [209] S. Amdouni, et al. *Semiconductor Science and Technology* **31**, 014011 (2015). URL <https://doi.org/10.1088/0268-1242/31/1/014011>.
- [210] Y. Shao, et al. *Frontiers of Optoelectronics in China* **4**, 171 (2011). URL <https://doi.org/10.1007/s12200-011-0159-4>.
- [211] J. Hua, et al. *Journal of Physics and Chemistry of Solids* **70**, 192 (2009). URL <https://doi.org/10.1016/j.jpcs.2008.10.004>.
- [212] Y. M. A. Yamada, et al. *Angewandte Chemie International Edition* **53**, 127 (2013). URL <https://doi.org/10.1002/anie.201308541>.
- [213] F. Wang, et al. *Materials Research Bulletin* **44**, 126 (2009). URL <https://doi.org/10.1016/j.materresbull.2008.03.024>.

- [214] N. Brahiti, et al. *Materials Research Bulletin* **62**, 30 (2015). URL <https://doi.org/10.1016/j.materresbull.2014.11.007>.
- [215] Y. Qu, et al. *Journal of Materials Chemistry* **20**, 3590 (2010). URL <https://doi.org/10.1039/c0jm00493f>.
- [216] H. Hu, et al. *The Journal of Physical Chemistry C* **111**, 3467 (2007). URL <https://doi.org/10.1021/jp066440f>.
- [217] X. Yang, et al. *Journal of Materials Chemistry A* **2**, 9040 (2014). URL <https://doi.org/10.1039/c4ta00119b>.
- [218] K. Pan, et al. *Dalton Transactions* **41**, 2564 (2012). URL <https://doi.org/10.1039/c2dt12182d>.
- [219] F. Liao, et al. *Journal of Materials Science: Materials in Electronics* **26**, 4722 (2015). URL <https://doi.org/10.1007/s10854-015-2949-8>.
- [220] C. D'Andrea et al. *Nanotechnology* **20** (2009).
- [221] L. Mikac, et al. *Croatica Chemica Acta* **88**, 437 (2015). URL <https://doi.org/10.5562/cca2769>.
- [222] V. M. Nardo, et al. *Atti della Accademia Perloritana dei Pericolanti. Classe di Scienze Fisiche, Matematiche e Naturali* **95**, A5-1-A5-12 (2017). URL <http://doi.org/10.1478/AAPP.951A5>.
- [223] A. Bailini et al. *Europhysics Letters (EPL)* **79**, 35002 (2007). URL <https://doi.org/10.1209/0295-5075/79/35002>.
- [224] M. C. Spadaro, et al. *EPL (Europhysics Letters)* **109**, 25002 (2015). URL <https://doi.org/10.1209/0295-5075/109/25002>.
- [225] P. Prielcel, et al. *Chinese Journal of Catalysis* **37**, 1619 (2016). URL [https://doi.org/10.1016/s1872-2067\(16\)62475-0](https://doi.org/10.1016/s1872-2067(16)62475-0).
- [226] M. Lukosi, et al. *Frontiers of Chemical Science and Engineering* **10**, 39 (2016). URL <https://doi.org/10.1007/s11705-015-1551-1>.
- [227] B. C. Ranu, et al. *ChemSusChem* **5**, 22 (2011). URL <https://doi.org/10.1002/cssc.201100348>.

- [228] F. Ullmann. *Berichte der deutschen chemischen Gesellschaft* **36**, 1017 (1903). URL <https://doi.org/10.1002/cber.190303601211>.
- [229] J. Hassan, et al. *Chemical Reviews* **102**, 1359 (2002). URL <https://doi.org/10.1021/cr000664r>.
- [230] S. V. Ley et al. *Angewandte Chemie International Edition* **42**, 5400 (2003). URL <https://doi.org/10.1002/anie.200300594>.
- [231] C. Annese, et al. *Journal of Peptide Science* **19**, 751 (2013). URL <https://doi.org/10.1002/psc.2571>.
- [232] C. Annese, et al. *Tetrahedron Letters* **54**, 515 (2013). URL <https://doi.org/10.1016/j.tetlet.2012.11.074>.
- [233] G. Evano, et al. *Chemical Reviews* **108**, 3054 (2008). URL <https://doi.org/10.1021/cr8002505>.
- [234] L. Rout, et al. *Organic Letters* **9**, 3397 (2007). URL <https://doi.org/10.1021/o10713887>.
- [235] S. Jammi, et al. *The Journal of Organic Chemistry* **74**, 1971 (2009). URL <https://doi.org/10.1021/jo8024253>.
- [236] P. Zhang, et al. *J. Mater. Chem. A* **1**, 1632 (2013). URL <https://doi.org/10.1039/c2ta00350c>.
- [237] A. Brennführer, et al. *Angewandte Chemie International Edition* **48**, 4114 (2009). URL <https://doi.org/10.1002/anie.200900013>.
- [238] A.-R. Hajipour, et al. *RSC Advances* **6**, 78468 (2016). URL <https://doi.org/10.1039/c6ra18679c>.
- [239] A. S. Prasad et al. *Journal of Molecular Catalysis A: Chemical* **370**, 205 (2013). URL <https://doi.org/10.1016/j.molcata.2013.01.002>.
- [240] N. Iranpoor, et al. *New Journal of Chemistry* **39**, 6445 (2015). URL <https://doi.org/10.1039/c5nj00655d>.
- [241] Y. S. Seo, et al. *Nanoscale Research Letters* **12** (2017). URL <https://doi.org/10.1186/s11671-016-1776-z>.

- [242] R. Ciganda, et al. *Chem. Commun.* **50**, 10126 (2014). URL <https://doi.org/10.1039/c4cc04454a>.
- [243] Z. Zhang, et al. *Chemical Communications* **47**, 3906 (2011). URL <https://doi.org/10.1039/c0cc05693f>.
- [244] M.-L. Wang, et al. *Journal of Materials Chemistry A* **1**, 5923 (2013). URL <https://doi.org/10.1039/c3ta10293a>.
- [245] R. Tang, et al. *Chemistry Letters* **37**, 834 (2008). URL <https://doi.org/10.1246/cl.2008.834>.
- [246] M. Schirber. <https://physics.aps.org/articles/v11/100>.
- [247] A. Ashkin, et al. *Optics Letters* **11**, 288 (1986). URL <https://doi.org/10.1364/ol.11.000288>.
- [248] M. C. Asplund, et al. *Analytical and Bioanalytical Chemistry* **411**, 5001 (2019). URL <https://doi.org/10.1007/s00216-019-01913-z>.
- [249] A. Ashkin et al. *Science* **235**, 1517 (1987). URL <https://doi.org/10.1126/science.3547653>.
- [250] A. Ashkin, et al. *Nature* **330**, 769 (1987). URL <https://doi.org/10.1038/330769a0>.
- [251] A. Ashkin et al. *Proceedings of the National Academy of Sciences* **86**, 7914 (1989). URL <https://doi.org/10.1073/pnas.86.20.7914>.
- [252] A. Ashkin, et al. *Nature* **348**, 346 (1990). URL <https://doi.org/10.1038/348346a0>.
- [253] D. G. Grier. *Nature* **424**, 810 (2003). URL <https://doi.org/10.1038/nature01935>.
- [254] K. Dholakia, et al. *Chem. Soc. Rev.* **37**, 42 (2008). URL <https://doi.org/10.1039/b512471a>.
- [255] Y. Nakayama, et al. *Nature* **447**, 1098 (2007). URL <https://doi.org/10.1038/nature05921>.
- [256] F. Dutto, et al. *Nano Letters* **11**, 2517 (2011). URL <https://doi.org/10.1021/nl201085b>.

- [257] O. M. Maragó, et al. *ACS Nano* **4**, 7515 (2010). URL <https://doi.org/10.1021/nn1018126>.
- [258] O. Marago, et al. *Nano Letters* **8**, 3211 (2008).
- [259] A. A. R. Neves, et al. *Optics Express* **18**, 822 (2010). URL <https://doi.org/10.1364/oe.18.000822>.
- [260] P. J. Pauzauskie, et al. *Nature Materials* **5**, 97 (2006). URL <https://doi.org/10.1038/nmat1563>.
- [261] R. Agarwal, et al. *Optics Express* **13**, 8906 (2005). URL <https://doi.org/10.1364/opex.13.008906>.
- [262] A. Ashkin. *Physical Review Letters* **24**, 156 (1970). URL <https://doi.org/10.1103/physrevlett.24.156>.
- [263] A. Jonás
et al. *ELECTROPHORESIS* **29**, 4813 (2008). URL <https://doi.org/10.1002/elps.200800484>.
- [264] R. W. Bowman et al. *Reports on Progress in Physics* **76**, 026401 (2013). URL <https://doi.org/10.1088/0034-4885/76/2/026401>.
- [265] O. Brzobohatý, et al. *Scientific Reports* **5** (2015). URL <https://doi.org/10.1038/srep08106>.
- [266] P. Zemánek, et al. *Journal of the Optical Society of America A* **19**, 1025 (2002). URL <https://doi.org/10.1364/josaa.19.001025>.
- [267] T. Čížmár, et al. *Applied Physics B* **84**, 197 (2006). URL <https://doi.org/10.1007/s00340-006-2221-2>.
- [268] O. Brzobohatý, et al. *Optics Express* **18**, 25389 (2010). URL <https://doi.org/10.1364/oe.18.025389>.
- [269] S. A. Tatarkova, et al. *Physical Review Letters* **89** (2002). URL <https://doi.org/10.1103/physrevlett.89.283901>.
- [270] V. Karásek, et al. *Physical Review Letters* **101** (2008). URL <https://doi.org/10.1103/physrevlett.101.143601>.

- [271] D. M. Gherardi, et al. *Applied Physics Letters* **93**, 041110 (2008). URL <https://doi.org/10.1063/1.2955518>.
- [272] W. Singer, et al. *Journal of the Optical Society of America B* **20**, 1568 (2003). URL <https://doi.org/10.1364/josab.20.001568>.
- [273] S. H. Simpson, et al. *Nano Letters* **17**, 3485 (2017). URL <https://doi.org/10.1021/acs.nanolett.7b00494>.
- [274] D. S. Bradshaw et al. *Physical Review A* **72** (2005). URL <https://doi.org/10.1103/physreva.72.033816>.
- [275] D. L. Andrews et al. *Optics Letters* **30**, 783 (2005). URL <https://doi.org/10.1364/ol.30.000783>.
- [276] S. H. Simpson, et al. *Physical Review A* **93** (2016). URL <https://doi.org/10.1103/physreva.93.023842>.
- [277] O. M. Maragò, et al. *Nature Nanotechnology* **8**, 807 (2013). URL <https://doi.org/10.1038/nnano.2013.208>.
- [278] Y. Arita, et al. *Optics Letters* **40**, 4751 (2015). URL <https://doi.org/10.1364/ol.40.004751>.
- [279] O. Brzobohatý, et al. *Optics Express* **24**, 26382 (2016). URL <https://doi.org/10.1364/oe.24.026382>.
- [280] O. Brzobohatý, et al. *Applied Physics Letters* **99**, 101105 (2011). URL <https://doi.org/10.1063/1.3634007>.
- [281] O. Brzobohatý, et al. *Nature Photonics* **7**, 123 (2013). URL <https://doi.org/10.1038/nphoton.2012.332>.
- [282] G. Pesce, et al. *Journal of the Optical Society of America B* **32**, B84 (2015). URL <https://doi.org/10.1364/josab.32.000b84>.
- [283] P. B. Roder, et al. *Langmuir* **28**, 16177 (2012). URL <https://doi.org/10.1021/la303250e>.
- [284] P. B. Roder, et al. *The Journal of Physical Chemistry C* **118**, 1407 (2014). URL <https://doi.org/10.1021/jp4078745>.

- [285] T. Čižmár, et al. *Laser Physics Letters* **8**, 50 (2010). URL <https://doi.org/10.1002/lapl.201010100>.
- [286] S. H. Simpson, et al. *Physical Review A* **76** (2007). URL <https://doi.org/10.1103/physreva.76.043408>.
- [287] A. Irrera, et al. *Nano Letters* **16**, 4181 (2016). URL <https://doi.org/10.1021/acs.nanolett.6b01059>.
- [288] F. Borghese, et al. *Physical Review Letters* **100** (2008). URL <https://doi.org/10.1103/physrevlett.100.163903>.
- [289] S. H. Simpson et al. *Nanotechnology* **23**, 205502 (2012). URL <https://doi.org/10.1088/0957-4484/23/20/205502>.
- [290] A. Irrera, et al. *Nano Letters* **11**, 4879 (2011). URL <https://doi.org/10.1021/nl202733j>.
- [291] W. J. Toe, et al. *Physical Review E* **93** (2016). URL <https://doi.org/10.1103/physreve.93.022137>.
- [292] S. H. Simpson et al. *Physical Review E* **82** (2010). URL <https://doi.org/10.1103/physreve.82.031141>.
- [293] P. H. Jones, et al. *ACS Nano* **3**, 3077 (2009). URL <https://doi.org/10.1021/nn900818n>.
- [294] F. Borghese, et al. *Optics Express* **14**, 9508 (2006). URL <https://doi.org/10.1364/oe.14.009508>.
- [295] G. Volpe et al. *Physical Review Letters* **97** (2006). URL <https://doi.org/10.1103/physrevlett.97.210603>.
- [296] A. Lehmuskero, et al. *Nano Letters* **13**, 3129 (2013). URL <https://doi.org/10.1021/nl4010817>.
- [297] L. Shao, et al. *ACS Nano* **9**, 12542 (2015). URL <https://doi.org/10.1021/acsnano.5b06311>.
- [298] V. Garcés-Chávez, et al. *Physical Review Letters* **91** (2003). URL <https://doi.org/10.1103/physrevlett.91.093602>.

Curriculum Vitae

Antonio Alessio Leonardi was born in Bari (BA), Italy, on October 4th, 1992.

Education

Ph.D. in Physics

Ph.D. student in Physics (XXXII cycle) at the Department of Physics and Astronomy "Ettore Majorana" of the University of Catania under the supervision of the Prof. Francesco Priolo and of the dr. Alessia Irrera of the CNR-IPCF of Messina for a scientific research activity on new sensoristic perspectives of silicon photonics.

Master degree in Physics 110/110 cum laude

Master degree in Physics at the Department of Physics and Astronomy "Ettore Majorana" of the University of Catania. Under the supervision of the Prof. Francesco Priolo and dr. Alessia Irrera of the CNR-IPCF of Messina the candidate carried out a thesis on the realization of the first sensor based on to the luminescence at room temperature of silicon nanowires for the specific and ultrasensitive detection of C-reactive protein (CRP).

Bachelor degree in Physics 110/110 cum laude

Bachelor degree in Physics at the Department of Physics and Astronomy "Ettore Majorana" of the University of Catania. Under the supervision of prof. Giovanni Piccitto the candidate realized a thesis on the plasmonic localized heating of gold nanoparticles performed by a simulation analysis

through COMSOL Multiphysics with applications in localized hypertermical treatments.

Publication and conference contribute list

Conference contributes:

Invited

1. Silicon Nanowires Array: From Photonics to Sensing, I symposium, E-MRS 2018, Strasburg

Oral

1. A new generation of label-free optical sensors based on silicon nanowires, FisMat 2017, Trieste
2. Ultrasensitive Label-free Optical Biosensors based on Silicon Nanowires, G symposium, E-MRS 2018, Strasburg
3. Silicon nanowires array: from photonics to sensing applications, NM03 symposium, MRS 2018, Boston
4. Label-free luminescent biosensors based on Si NWs, FisMat 2019, Catania

Posters

- CNS 2018, Catania
- 3 posters, G symposium, E-MRS 2018, Strasburg

- International School of Physics "Enrico Fermi", Course 204 "Nanophotonics" 2018
- CHESS school, Firenze 2019.

Attended

1. Materials, 2016, Catania

Awards:

1. Graduate Student Awards at European Material Research Society (EMRS) 2018, Strasburg, for a talk on: Ultrasensitive Label-free Optical Biosensors based on Silicon Nanowires.
2. Pietro Brovotto Award of the Italian Physics Society for the master degree thesis and the curriculum , 2019

International Schools, external courses, and visiting periods:

- Course: " Messaggeri della conoscenza", Nanoparticles physics and quantum optics subjects, Catania 2013-2014
- Stage of 6 months in the R&D group of the STmicroelectronics, Catania, 2016
- Course: Scientific writing, Scuola Superiore di Catania, 2017.
- Course: "Order and disorder in Nanophotonics", Scuola Superiore di Catania, 2018.
- International School of Physics "Enrico Fermi", Course 204 "Nanophotonics", Varenna 2018.
- Visiting for 2 weeks at the Chemistry department of the University College of London under the supervision of the prof. Giovanni Volpe.

- Visiting for 2 weeks at the Physics department of the Politecnico of Milan under the supervision of the prof. Giulio Cerullo.
- Visiting Student for 6 months at the Electrical and Computer Science departments and the Photonics Center of the Boston University, PI prof. Luca Dal Negro.
- CHESS school, Firenze 2019.

Publications in journal with Impact factor:

1. M. G. Donato, O. Brzobohaty, S. H. Simpson, A. Irrera, **A. A. Leonardi**, M. J. Lo Faro, V. Svak, O. M. Marago, P. Zemánek, Optical Trapping, Optical Binding, and Rotational Dynamics of Silicon Nanowires in Counter-Propagating Beams, **Nano Letters**, 2019, 19 (1), 342–352
2. A. Irrera, **A. A. Leonardi**, C. Di Franco, M. J. Lo Faro, G. Palazzo, C. D’Andrea, K. Manoli, G. Franzò, P. Musumeci, B. Fazio, L. Torsi, F. Priolo, New Generation of Ultrasensitive Label-Free Optical Si Nanowire-Based Biosensors, **ACS Photonics**, 2018, 5 (2), pp 471–479
3. **A. A. Leonardi**, M. J. Lo Faro, S. Petralia, B. Fazio, P. Musumeci, S. Conoci, A. Irrera, F. Priolo, Ultrasensitive Label-and PCR-Free Genome Detection Based on Cooperative Hybridization of Silicon Nanowires Optical Biosensors, **ACS Sensors** 2018, 3, 9, 1690-1697
4. **A. A. Leonardi**, M. J. Lo Faro, C. Di Franco, G. Palazzo, C. D’Andrea, D. Morganti, K. Manoli, P. Musumeci, B. Fazio, M. Lanza, L. Torsi, F. Priolo, A. Irrera. Silicon nanowire luminescent sensor for cardiovascular risk in saliva, **Journal of Material Science: Materials in Electronics**, 2018, <https://doi.org/10.1007/s10854-018-0417-y>
5. A. Irrera, M. J. Lo Faro, C. D’Andrea, **A. A. Leonardi**, P. Artoni, B. Fazio, R. A. Picca, N. Cioffi, S. Trusso, G. Franzo, P. Musumeci, F. Priolo, F. Iacona, Light-emitting silicon nanowires obtained by metal-assisted chemical etching, **Semiconductor Science and Technology**, 2017, 32, 1-20

6. M. Casiello, R. A. Picca, C. Fusco, L. D'Accolti, **A. A. Leonardi**, M. J. Lo Faro, A. Irrera, S. Trusso, P. Cotugno, M. Sportelli, N. Cioffi, A. Nacci, Catalytic activity of silicon nanowires decorated with gold and copper nanoparticles deposited by pulsed laser ablation, **Nanomaterials**, 2018, 8(2), 78
7. M. J. Lo Faro, **A. A. Leonardi**, C. D'Andrea, D. Morganti, P. Musumeci, C. Vasi, F. Priolo, B. Fazio, A. Irrera, Low Cost Fabrication of Si NWs/CuI Heterostructures, **Nanomaterials**, 2018, 8(8), 569
8. M. J. Lo Faro, **A. A. Leonardi**, C. D'Andrea, D. Morganti, P. Musumeci, C. Vasi, F. Priolo, B. Fazio, A. Irrera, Low cost synthesis of silicon nanowires for photonic applications, **Journal of Material Science: Materials in Electronics** 2019, <https://doi.org/10.1007/s10854-019-00672-y>
9. W. Giurlani, V. Dell'Aquila, M. Vizza, N. Calisi, A. Lavacchi, A. Irrera, M. J. Lo Faro, **A. A. Leonardi**, D. Morganti, M. Innocenti, Electrodeposition of Nanoparticles and Continuous Film of CdSe on n-Si (100), **Nanomaterials**, 2019, 9(10), 1504
10. M. J. Lo Faro, C. D'Andrea, **A. A. Leonardi**, D. Morganti, A. Irrera, B. Fazio, Fractal silver dendrites as 3D SERS biosensing platform for highly sensitive detection of biomolecules in hydration conditions, **Nanomaterials**, 2019, 9(11), 1630

Outcoming publications

11. **A. A. Leonardi** et al., All-optical reciprocity breaking mechanism in Raman Coherent Backscattering from a disordered slab of Silicon nanowires. submitted 2019
12. Lo Faro M. J., **A. A. Leonardi** et al., Enhanced erbium emission in Er:Y₂O₃ decorated fractal arrays of silicon nanowires. submitted 2019

Publications without Impact factor:

1. Relazione tra luminosità e diametro delle galassie: un'esperienza didattica. *Giornale di astronomia* 2011, 37 (2), 43

Cover of journal with impact factor:

1. Semiconductor Science and Technology, Volume 32, Issue 4 (April 2017)
2. Nanomaterials, Volume 8, Issue 2 (February 2018)

Chapters of books:

1. B. Fazio, G. Ruello, A. A. Leonardi, D. Morganti, M. J. Lo Faro, A. Irrera, 22 - Raman spectroscopy: methods and techniques for applications in cultural heritage, Springer Handbook of Cultural Heritage Analysis, just accepted 2019

Acknowledgements

Here we go on the most complicated part of the physics, the emergent phenomena that take the name of consciousness, and finally, of our feelings. No sorry I'm just joking about that... or maybe not. However, I'm very pleased that you my reader reach this part, so the first thanks is for you, whoever you are. By the way, I want really to thanks all the people that were close to me during this project: my friends, my colleagues, and my family. In particular thanks to all the Capybara group, Piccia, Fonti, and Anaconda. Thanks to my father, my mother, and my brother. A special thanks goes to the entire reasearch group to which I belong. I'm very lucky to work with such good scientists and people that make really hard to find appropriate words. Thanks to Alessia, José, Dario, Barbara, Paolo, and to prof. Priolo for their trust, time and kindness. All of them have driven what can be considered a success in these years and I will continue to growth also thank to them. José is not just a colleague but a friend and was the first to help me and to create a special friendly and helpful environment at work. Dario, even if you are just arrived this year we are friend from so long time that I always used your time, your help and you presence, at work and in the private life. Barbara thank you for help anytime I need it, for your advices and for everything that I learned from you. Paolo you helped me to growth not only as scientist but as person in the network activity. Prof. Priolo your hard work, smartness, dialectic and elegant knowledge is of inspiration for my hard work and personal growth. Alessia deserves more than what can be wrote, thanks for your time even during the weekend, for your trust, and in particular, for your lead that have made me a better scientist and a better person. I want really to thanks Pietro Gucciardi, Onofrio Maragò, Antonella

Iatì, and Mariagrazia Donato for all the useful scientific and friendly discussion that helped me a lot. Thanks also to Cirino Vasi and Giovanna Toscano for the welcome shown and all the help during these years at the CNR-IPCF. Another special thank goes to prof. Giuseppe Angilella for all the kind help during my years at the University. Among all the things, thank you so much for your help in all my darkest time with latex. My acknowledgements also go to all the technician that silently make our work feasible: thanks to G. Lupò, D. Arigò, G. Gismondo, R. Caruso, G. Spinella, S. Tatì, G. Panté, and C. Percolla. In general, without cite every person that I met in these years, I would like really to thanks all the research center and institute with which we collaborated or where I spent some of my visiting periods. In particular, thanks to CNR-IPCF of Messina, CNR-IMM of Catania, STmicroelectronics of Catania, Chemistry department of the Bari University, Chemistry department of Messina University, Chemistry department of the UCL, Physics department of the Politecnico of Milan, and finally the Photonics Center and the department of Electrical and Computer Engineering of the Boston University. I want to thanks Sabrina Conoci and Salvatore Petralia for my time spent in STmicroelectronics. In particular thanks to the prof. Giorgio Volpe of the UCL, to prof. Dario Polli and prof. Giulio Cerullo of the Politecnico of Milan for the time, the advice, and for what I learned during my period in London and Milan. I owe a special appreciation to the prof. Luca Dal Negro for what I learned and for the extremely active and interesting period spent in his group for 6 months at the ECE and Photonics Center of the BU.